PhD Thesis

Self-organized magnetization patterns in cold atoms

Supervisor:
Prof. Thorsten Ackemann
Additional supervisors:
Prof. Gian-Luca Oppo
Dr. Aidan Arnold

Author:
Ivor Krešić

A thesis submitted to the University of Strathclyde
in partial fulfilment of the requirements
for the degree of
Doctor of Philosophy

Department of Physics

February 22, 2017

Declaration of Authorship

I declare that, except where specifically indicated, this thesis titled, 'Self-organized magnetization patterns in cold atoms' and the work presented in it are my own and I am the sole author of all parts.

UNIVERSITY OF STRATHCLYDE

Abstract

Department of Physics

Doctor of Philosophy

Self-organized magnetization patterns in cold atoms

by Ivor Krešić

This Thesis reports on a realization of self-organized magnetization patterns in a cloud of cold atoms driven far from equilibrium by a pump laser beam. The experiments are performed in the single mirror feedback configuration, where transverse ordering occurs due to amplification of fluctuations in the atomic medium at critical lengthscales via the optical non-linearity and the Talbot effect. For a linearly polarized pump beam a generation of modulated light with orthogonal polarization is seen to occur, signaling the presence of a polarization instability. Imaging of the refractive index modulations at the end of the cloud reveals complementary regions of the two orthogonal circularly polarized components of the imaged light, which is related to the ordering of atomic spins. A detailed investigation of dependence of pattern properties on the direction and strength of the applied B-fields is presented. In addition to this, a theoretical model describing the dynamics and coupling of atomic magnetic moments and the laser light in the relevant parameter regime is developed and shown to provide good agreement with results of the experiment.

Non-equilibrium self-organization of atomic degrees of freedom in cold gases can in some cases be mapped onto phase transitions in condensed matter systems. In this respect, the single mirror feedback configuration is particularly interesting as it provides a simple arrangement where ordering breaks the continuous translational and rotational symmetries of the initial system.

Acknowledgements

Judging from anecdotal evidence, doing a PhD project in experimental atomic physics often feels the way I imagine digging through dirt looking for gold would. The equipment rarely works exactly the way one wants it to (until it does) and the results are most of the time too noisy, vague and inconclusive. On top of that there is the weight of all the experimental and theoretical work done since the dawn of modern science, telling you that what you are setting out to do is at best incremental and at worst useless, uninteresting or wrong. This is why a student relies on good mentorship, and I have been fortunate to have Thorsten Ackemann as my Thesis supervisor. I thank Thorsten for the guidance provided during the last three years and the hours spent teaching me the hidden art of transverse pattern formation in non-linear optics.

In addition to Thorsten, I've had the privilege of working with a number of talented researchers. I thank William Guerin and Pedro Gomes for teaching me most of what I know about running a cold atoms experiment. I also thank Pedro Gomes for his work on the early stages of the MOT experiment, and Paul Griffin and Aidan Arnold for their experimental advice throughout the duration of this Thesis. Robin Kaiser I thank for granting me the opportunity to study superradiance in cold atoms. Guillaume Labeyrie I thank for numerous discussions on the pattern formation experiments and their results. I would also like to thank Stefan Kuhr for the financial assistance during the last few months of this project. The simulation results presented in this Thesis would not have been possible without the work of the members of the Strathclyde Computational Non-linear Quantum Optics group. I thank Gordon Robb for developing the code for solving the dynamical equations in the single-mirror feedback configuration, Willie Firth for developing the “thick medium” theory, and Gian-Luca Oppo for general theoretical advice.

I also want to thank the numerous students and postocs of the Strathclyde Experimental Quantum Optics and Photonics group for providing a stimulating work environment and making the last three years in Glasgow enjoyable. Most of all I thank my family and friends, who have been supportive of me through the years.

Contents

Declaration of Authorship **i**

Abstract **ii**

Acknowledgements **iii**

List of Figures **vii**

Abbreviations **ix**

1 Optical pattern formation in the transverse plane **1**
- 1.1 Introduction 1
  - 1.1.1 Transverse patterns in non-linear optics 2
  - 1.1.2 Self-organization in cold atomic gases: simulating condensed matter physics 4
- 1.2 Single mirror feedback configuration 5
  - 1.2.1 Pattern formation mechanism 5
  - 1.2.2 Talbot effect 8
  - 1.2.3 Optical pumping nonlinearity 9
- 1.3 Describing systems driven out of thermodynamic equilibrium 12
  - 1.3.1 Dynamical systems theory 12
  - 1.3.2 Attractors 13
  - 1.3.3 Bifurcations 14
  - 1.3.4 Linear stability analysis 16
  - 1.3.5 Pattern symmetry selection 19

2 Modeling the atom-light interaction **22**
- 2.1 Theoretical framework 23
  - 2.1.1 Semiclassical atom-light interaction 23
  - 2.1.2 Multipole decomposition of the density matrix 26
  - 2.1.3 Deriving the equations 30
- 2.2 Medium equations 34
  - 2.2.1 Longitudinal $B-$field 34
  - 2.2.2 Transverse $B-$fields 36

2.2.3 Optical response 38
2.3 Numerical results 39
2.3.1 Longitudinal B-field 39
2.3.2 Transverse B-fields 43
2.3.3 Optical properties 44

3 Experimental setup 47
3.1 Preparation and characterization of the optical medium 47
3.1.1 Laser cooling and trapping of neutral atoms 47
3.1.2 Principle of magneto-optical trapping 49
3.1.3 Laser system 50
3.1.4 Setup for laser cooling and trapping 54
3.1.5 Optical thickness optimization and measurements 56
3.1.6 Temperature measurements 59
3.2 Pattern measurements 61
3.2.1 Experimental sequence 61
3.2.2 Near and far field imaging 63
3.2.3 Monitoring pump intensity 68
3.2.4 B-field control and measurements 69

4 Experimental results 74
4.1 Region of instability 75
4.2 Breaking of inversion symmetry 76
4.3 Instability onset 80
4.4 Scanning the B-fields 84
4.5 Relation to previous work 88

5 Simulating the magnetization patterns 91
5.1 Linear stability analysis 92
5.1.1 Self-organization via mirror feedback 92
5.1.2 Polarization instability 95
5.2 One dimensional model 99
5.2.1 Steady state patterns 100
5.2.2 Longitudinal B-field scan 103
5.2.3 Transverse B-field scans 104
5.3 Two dimensional model 106
5.3.1 Pattern symmetries 106
5.3.2 Spin magnetization 108
5.4 Summary 109

6 Thick medium effects 110
6.1 Theoretical model 111
6.1.1 Beam propagation through the medium 111
6.1.2 Transverse perturbations in the quasi-Kerr limit 112
6.1.3 Calculating the thresholds 114

6.2 Experimental results . . . 115
6.3 Discussion . . . 118

7 Conclusion and outlook **120**

A Derivation of the dynamical equations **122**
A.1 Longitudinal B-field . . . 122
A.2 Transverse $B-$fields . . . 124
A.3 Optical response . . . 126

List of original publications **128**

Bibliography **129**

List of Figures

1.1 Principle of single-mirror feedback mechanism . . . 6
1.2 Principle of optical pumping into stretched states for the $F = 1 \rightarrow F' = 2$ transition. . . . 10
1.3 Description of the spin ordering in the single-mirror feedback configuration . . . 11
1.4 Illustration of *supercritical* and *subcritical* bifurcations . . . 15
1.5 Types of instabilities . . . 17
1.6 Pattern symmetry selection . . . 21

2.1 Hyperfine level structure of model system . . . 25
2.2 Symmetries of magnetic multipole states . . . 30
2.3 Driving terms of atomic variables . . . 32
2.4 Comparison of approximate and full steady state solutions for linear light . . . 40
2.5 Comparison of approximate and full steady state solutions for elliptical light . . . 41
2.6 Transverse B-field scans for linear light . . . 42
2.7 Parralel B-field scan for linear light, varying longitudinal and orthogonal fields . . . 43
2.8 Orthogonal B-field scan for linear light, varying longitudinal and orthogonal fields . . . 44
2.9 Susceptiblities of the medium . . . 45
2.10 Susceptiblities of the medium, B_x-scan . . . 46

3.1 Principle of magneto-optical trapping . . . 49
3.2 Atomic levels and laser locking . . . 51
3.3 Schematics of the MOT and pattern formation setup . . . 54
3.4 Principle of compressed MOT . . . 57
3.5 Properties of compressed MOT (cMOT) . . . 59
3.6 Time of flight temperature measurement of the cMOT cloud . . . 60
3.7 MOT compression images . . . 61
3.8 Experimental sequence for measuring pattern formation . . . 62
3.9 Schematics and example of near field imaging . . . 65
3.10 Schematics and example of far field imaging . . . 66
3.11 Monitoring shot-to-shot intensity fluctuations . . . 68
3.12 B-field switching process . . . 70

3.13 Simulations of the non-linear Faraday effect 71
3.14 Experimental measurements of non-linear Faraday rotation 73

4.1 Region of instability 76
4.2 Pattern symmetries, near field images 77
4.3 Pattern symmetries, far field images 79
4.4 Other pattern symmetries for the $B = 0$ case 80
4.5 Dependence of diffracted power on pump duration 81
4.6 Total diffracted power vs. input beam intensity 82
4.7 Normalized diffracted power vs. input beam intensity 83
4.8 Diffracted light vs. longitudinal B-field 84
4.9 Asymmetry of the diffracted power in the B_z-scan 85
4.10 Total diffracted power vs. B_z-scan 86
4.11 Diffracted power vs. transverse B-fields 87
4.12 Diffracted power vs. transverse B-fields 88

5.1 Steady state patterns in 1D, zero B-field 101
5.2 Steady state patterns in 1D at applied longitudinal B-field 102
5.3 Intensity modulations for applied longitudinal B-field 103
5.4 Modulation depth vs. longitudinal B-field 104
5.5 Modulation depth vs. parallel and orthogonal B-fields 105
5.6 Square patterns at zero B-field values 106
5.7 Hexagon patterns at finite B_z values 107
5.8 1D cuts along w magnetization peaks, square patterns 108
5.9 1D cuts along w magnetization peaks, hexagonal patterns 109

6.1 Threshold curve for a Kerr medium 115
6.2 Scan of mirror distance 117
6.3 Talbot rings for varying mirror distance 118

Abbreviations

AOM	Acousto-optical modulator
BEC	Bose-Einstein condensation
CCD	Charge-coupled device
CP	Counter-propagating (beam configuration)
CPT	Coherent population trapping
EIT	Electromagnetically induced transparency
EOM	Electro-optical modulator
GPIO	General purpose input/output
h.o.t	Higher order terms
HWP	Half-wave plate
LHS	Left hand side
MOT	Magneto-optical trap
OD	Optical density
PBS	Polarizing beam splitter
PD	Photodiode
QWP	Quarter-wave plate
RHS	Right hand side
RWA	Rotating wave approximation
SFM	Single feedback mirror (configuration)
TA	Tapered amplifier

Chapter 1

Optical pattern formation in the transverse plane

In this introductory Chapter the theoretical background required to understand the main results of the rest of the Thesis is given. An introductory outline of the study of light-induced self-organization of atomic degrees of freedom is given first. This introduction is followed by a heuristic discussion on the particular system studied in this Thesis, the single feedback mirror (SFM) setup. Some remarks are made on the nature of the non-linearity employed in the pattern formation process. In the last Section of this Chapter an introduction of some of relevant the concepts of dynamical systems theory is made, and shown how it relates to the results of this Thesis.

1.1 Introduction

In this Section an overview of the results on self-organization in optical systems is presented. The first part is devoted to the work on transverse patterns in non-linear systems, discussing the pioneering studies performed in the 1990s and the modern implementations of these ideas. The second part describes the more recent work done in cold atoms, commonly referred to as *cold atom simulations*. Some important results are outlined, along with potential connections to the field of *quantum technologies*.

1.1.1 Transverse patterns in non-linear optics

The term transverse optical instability describes the instabilities occurring in the orthogonal plane of optical systems laser driven along a single axis. The study of transverse instabilities in optical media driven by counter-propagating (CP) beams started in the late 1980s with e.g. work concerning oscillatory instabilities in atomic vapors by Grynberg et. al. [1] and Gauthier et. al. [2] and static instabilities in a Kerr medium by Firth et. al. [3]. In 1990 a scheme called the single feedback mirror configuration (SFM) was devised by Firth [4] which was a simplification with respect to the CP arrangement and allowed for better experimental control of pattern lengthscales than in the CP case. This scheme was subsequently employed for experimental observations of pattern formation in liquid crystals [5, 6, 7, 8], thin organic films [9], photorefractives [10, 11] and alkali vapors [12, 13, 14].

In the SFM scheme, as will be explained in more detail in Section 1.2, the patterns form due to the feedback provided by the mirror reflection and the optical non-linearity of the medium. Even in a single type of medium, several kinds of optical non-linearities can exist. The non-linearities utilized in the early pattern formation experiments in atomic vapors were based on optical pumping into dark Zeeman sublevels, which do not couple to the light [13]. More recent experiments, this time using thermal cold atomic clouds as the medium, utilized different kinds of non-linearities. The experiments of Gauthier et. al. [15, 16, 17] in the CP configuration used optical non-linearities based on pumping into the stretched (maximum spin projection number $|m|$) Zeeman states, simultaneously cooling and polarizing the atoms. These experiments reported on a formation of lattices (gratings) along longitudinal and transverse directions causing modulations of the atomic densities to occur. Another set of experiments was done in the group of G. Labeyrie at INLN, where the optomechanical [18] and the saturable two-level non-linearities

[19] were used to observe patterns in cold atoms in the SFM configuration. A polarizing beam splitter (PBS) was inserted inside the feedback loop to make sure that the light polarization is preserved in the pattern formation process and the patterns can be understood in the scalar framework. The optomechanical non-linearity [20, 21] is based on bunching of the atoms in regions of minimum intensity (for a detuning $\Delta > 0$) by the optical dipole force [22]. In steady state this results in modulations of atomic density in the transverse plane.

In this Thesis, the SFM configuration is used to create self-organized patterns in the magnetic sublevels of the optical transition used. The difference in the setup with respect to the experiments of Ref. [18, 19] is in removing the PBS from the feedback loop, allowing the polarization degree of freedom of the light to participate in the pattern formation process. The resulting polarization instability is similar to the one observed in the group of W. Lange [23], however there are some differences in the physics of these two systems. The experiments of e.g. Ref. [13] use hot vapors with Doppler broadening due to atomic motion on the level of ~ 1 GHz, which is avoided in the experiments reported here by using a magneto-optical trap to reduce the Doppler width below the transition linewidth. The Doppler broadening is related to the Doppler effect, due to which the frequency of the light seen by the moving atom either increases (for atoms moving toward the direction of the light beam) or decreases (for atoms moving away from the direction of the light beam). The other difference is in the level structures of the Na atoms used in [13] and the Rb atoms used in this Thesis. The $J = 1/2 \rightarrow J' = 1/2$ transition of the Na line allows only for dipole (spin) physics, whereas the $F = 2 \rightarrow F' = 3$ can in principle allow even the quadrupole terms to play a role (for a discussion of the meaning of the magnetic multipole nomenclature in this context see Chapter 2). The quantum numbers J and F denote the total angular momentum of the valence electron and the sum of the nuclear spin and total electron angular momentum, respectively. The transition $F = 2 \rightarrow F' = 3$ is modeled in this Thesis by the minimal model capturing all the relevant physics, which is the $F = 1 \rightarrow F' = 2$ transition, and the main physical effects leading to self-organization are shown to be dipolar in origin.

1.1.2 Self-organization in cold atomic gases: simulating condensed matter physics

The idea of using cold atomic gases to study condensed matter phenomena in a more controlled setting has an almost 20 year history [24, 25, 26]. The study of self-organization, where the ordering occurs in the atomic degrees of freedom not confined to fixed regions of space by an external potential, is one branch of this kind of research [27]. One notable example of an experiment studying self-organization in a Bose-Einstein condensate (BEC) placed in a transversely pumped single mode Fabry-Perot cavity is reported in Ref. [28], where a Dicke phase transition of the atomic motional degrees of freedom is observed. A Dicke phase transition occurs in systems described by the Dicke Hamiltonian [29], where the cavity photons coherently excite the collective atomic modes, in this particular experiment given by discrete eigenstates of the momentum operator [28], when both the cavity mode and the collective atomic modes reach a macroscopic occupation. The initial experiment was based on the atomic ordering into odd or even wells of the generated cavity potential thus breaking only a discrete symmetry, however a recent modification of the experiment reports on a formation of a supersolid-like phase by breaking of a continuous symmetry [30]. A supersolid phase occurs spontaneously when matter possesses both the quantum phase and crystalline order, breaking the continuous translational spatial symmetry in the process [31]. A wealth of thermodynamical phases is also predicted to occur for a BEC trapped in a multimode cavity [32, 33, 34, 35]. Other innovative ideas concern using photonic crystal waveguides to trap the atoms by evanescent fields, and engineer the waveguide dispersion relation to control the light-mediated atom-atom interactions [36, 37]. Self-organized phases were predicted to occur in BECs in the single feedback mirror configuration [38, 39] and in free space [40], with realizations in ring cavities [41]. Current experiments in thermal cold atoms used single mode cavities to achieve cavity cooling and self organization [42, 43] and also the counter-propagating [15] and single feedback mirror [44, 18] beam configurations. A wealth of theoretical proposals has been put forward in recent years to study the dissipative dynamics of thermal ensembles in Fabry-Perot cavities pumped transversely [45, 46].

In addition to the potential use in studying analog condensed matter systems, some intriguing technological prospects exist for the patterns of the kind studied in this Thesis. The theory of Grynberg and Lugiato [47] showed how squeezing of either the difference between the intensities or the phases of two opposite side-bands can occur for transverse patterns in the single-mirror feedback configuration. Squeezing of light [48] and the atomic spin [49] has been shown to be useful for precision measurements near the quantum limit. Another effect with potential use in e.g. photonic quantum circuits is the high fifth order non-linearity observed by Greenberg and Gauthier in a cloud of cold atoms pumped in the CP configuration [50]. A proposal for realizing dissipative solitons in a thermal ensemble in a ring cavity, potentially useful for quantum memory applications, has been considered by Tesio et. al. [51].

1.2 Single mirror feedback configuration

1.2.1 Pattern formation mechanism

A particularly fruitful system for transverse pattern formation was first considered in 1990 by William J. Firth [4]. In this work a nonlinear medium is optically excited by a laser beam which is then reflected from a planar feedback mirror. The refractive index fluctuations inside the medium cause a phase grating to form in the beam at the end of the cloud, and interference patterns to emerge due to Talbot diffraction [52] during the propagation from the mirror and back. The mirror provides positive feedback which increases the refractive index modulations via the optical non-linearity of the medium only to fluctuations with critical wavevectors of modulus $|\mathbf{q}_c|$ determined by the Talbot effect and mirror distance. Self-organized patterns can thus arise spontaneously from the homogeneous initial state, breaking both translational and rotational symmetries of the initial system in the plane transverse to the pump beam.

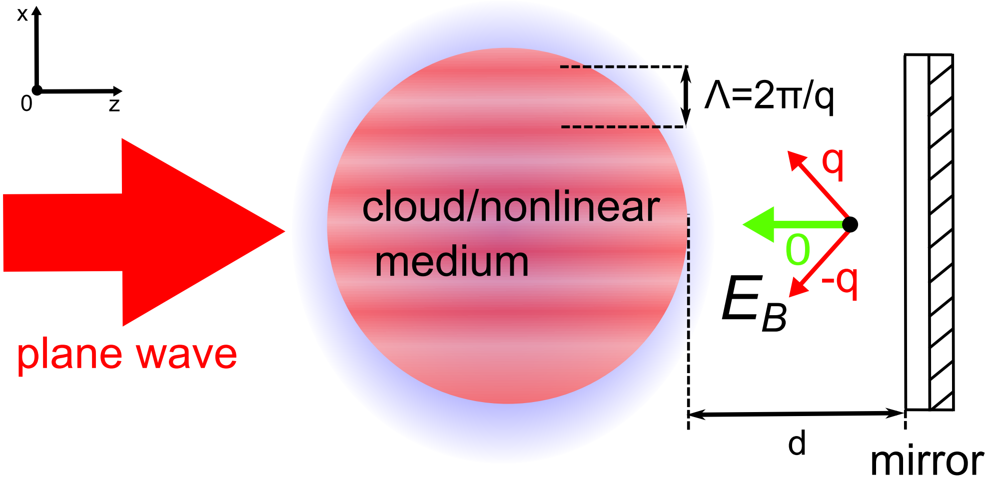

FIGURE 1.1: Principle of single-mirror feedback mechanism. The plane wave input beam impinges on the cold atomic cloud used as the optically non-linear medium. The initial refractive index fluctuations in the optically nonlinear cloud of cold atoms are converted into amplitude modulations only for modulations with lengthscales of $\Lambda_c = \sqrt{4\lambda d}$ in the self-focusing medium. The backward propagating beam E_B with a modulated amplitude is a result of interference of the sidebands with the zero order beam.

Using atoms as the nonlinear medium, first considered experimentally in Ref. [13] adds another interesting layer to the problem. In case when the optical nonlinearity is based on light interacting with magnetic sublevels of the atoms, diffractive coupling of spatially separated regions inside the atomic cloud mimics magnetic interactions. This type of interaction can be said to be *mirror mediated*, and provides an alternative to the *cavity mediated* interactions used in many setups with cold and ultracold atoms [43, 28, 53, 32]. The study of bifurcations occurring in such systems may provide insight into magnetic phase transitions in condensed matter.

The basic principle of pattern formation in the SFM configuration is illustrated in Fig. 1.1, in a one-dimensional system. The plane wave laser beam with flat phase and amplitude enters a medium with a fluctuating refractive index. It is assumed the fluctuations occur at all wavenumbers q, due to e.g. the random nature of atomic motion in an atomic cloud. At high detuning $\Delta \gg \Gamma_1$ (where Γ_1 is the natural linewidth of the optical transition), the absorption coefficient, decaying as Δ^{-2}, can be neglected with respect to the refractive index, decaying as Δ^{-1} [22]. The influence of the medium on the plane wave field is then to change its phase as $\varphi = \chi_q kL$, where χ_q is the medium susceptibility, k is the longitudinal wavenumber of the light and L is the length of the medium. The medium susceptiblity is related to the refractive index n_q given by

$$n_q = n_0 + \Delta n(I) \cos(qx), \tag{1.1}$$

via the relation $n_q = 1 + \chi_q/2$, where n_0 is the linear refractive index, while $\Delta n(I)$ is the amplitude of refractive index modulation. The influence of the medium of longitudinal length L on the beam is given by the equation [54]

$$\frac{\partial E(x,z)}{\partial z} = ik\chi_q E(x,z). \tag{1.2}$$

It should be noted that, for reasons of convenience, the paraxial and propagation equations [54] for the electric field used in this Chapter follow the convention $E \sim \exp(i(kx - \omega t))$ for the electric field, which is not the same as the convention in Eq. (2.5) followed throughout the rest of the Thesis. The initial amplitude of the refractive index modulation is small, so the electric field immediately after the cloud can be Taylor expanded up to the first order in $\Delta n(I)$ to get

$$E(x, z = L) \approx E_0(1 + i\Delta n'(I) \cos(qx)), \tag{1.3}$$

where $\Delta n'(I) = 2kL\Delta n$.

1.2.2 Talbot effect

After the cloud, the beam undergoes free space propagation, governed by

$$\frac{\partial E(x,z)}{\partial z} = \frac{i}{2k}\frac{\partial^2}{\partial x^2}E(x,z), \tag{1.4}$$

which is sometimes referred to as near-field diffraction [23]. This propagation results in conversion of phase modulation into amplitude modulation over a quarter of a distance known as the Talbot distance [52]. The transversely modulated term in the above expression (1.3) propagates to the mirror and back and diffracts according to Eq. (1.4), causing interference between the zeroth order and the sidebands generated by the sinusoidal modulation of refractive index. During a propagation for a distance $2d$ to the mirror and back this interference results in a phase shift of $\Theta = q^2 d/k$ in the transversely modulated part of the field [4]. The backwards propagating electric field E_B is now given by

$$E_B(x, z = L) = \sqrt{R}E_0(1 + ie^{-i\frac{q^2 d}{k}}\Delta n'(I)\cos(qx)). \tag{1.5}$$

For diffractive phase shifts of $\Theta = \frac{\pi}{2} + 2m\pi$ (where m is an integer), the initial phase grating is converted into an amplitude grating, for $\Theta = \pi + 2m\pi$ it is converted into a phase grating shifted by half a period, for $\Theta = \frac{3\pi}{2} + 2m\pi$ an amplitude grating shifted by half a period and for $\Theta = 2\pi + 2m\pi$ it is converted back into the initial phase grating.

The effect of the medium nonlinearity and mirror feedback can now be seen clearly. Growth of patterns out of a randomly distributed range of lengthscales relies on amplification of phase gratings with intensity dependent amplitudes $\Delta n(I)$ by conversion into amplitude gratings. In the linear approximation (1.3) a single wavenumber, often called the critical wavenumber $q_c = \frac{2\pi}{\Lambda_c}$ (where Λ_c is the critical lengthscale), has a much stronger growth amplitude than the other perturbations. In a self-focusing medium ($\Delta n(I)$ increases with I), the phase grating is amplified if an intensity modulation with the same phase and period is reflected onto it, meaning the critical wavenumber of the growing fluctuation is $q_c^{SF} = \sqrt{\frac{k\pi}{2d}}$, which has a lengthscale $\Lambda_c = \sqrt{4\lambda d}$, for light of wavelength λ and the mirror distance d. A self-defocusing medium ($\Delta n(I)$ decreases with I) experiences a growth of phase modulation if an intensity modulation with a π shifted period is reflected onto it, and the critical wavenumber is $q_c^{SD} = \sqrt{\frac{3k\pi}{2d}}$, with the lengthscale given by $\Lambda_c = \sqrt{\frac{4}{3}\lambda d}$. For intensities I higher than the threshold intensity I_{th}, the nonlinear modulation amplitude $\Delta n(I)$ becomes sufficiently high to counter the thermal fluctuations and a steady state pattern emerges.

1.2.3 Optical pumping nonlinearity

The optical nonlinearity relevant for patterns studied in this Thesis is based on pumping the atoms into states with maximum magnetic projection quantum number $|m|$, often called stretched states. As described in Chapter 2, the minimal model required to describe the Zeeman sublevels of the experimentally probed atomic transition is the $F = 1 \rightarrow F' = 2$ system. In this system, the main driver of instability is orientation, equal to the difference between populations in the two stretched states.

The mechanism of nonlinearity is depicted in Fig. 1.2. In case when optical pumping rate is smaller than the depumping rate, in cold atom experiments set to $\gamma \sim 10$ kHz mainly by stray transverse B-fields, the populations are spread evenly between all ground states. The optical response of the medium is then given by a weighted average between all optical coherences with weights proportional to Clebsch-Gordan coefficients [22]. When the pump rate P_+ is greater than the depump rate γ, the population of the stretched state increases. If the laser beam is red detuned from the excited state energy levels, the refractive index n of an optical transition is $n > 1$ [22]. The refractive index of an atom pumped into a stretched state coupling to the light, also called a bright stretched state, will in the case of the $F = 1 \rightarrow F' = 2$ transition be increased by a factor of $9/5$ (see Eq. (2.26)).

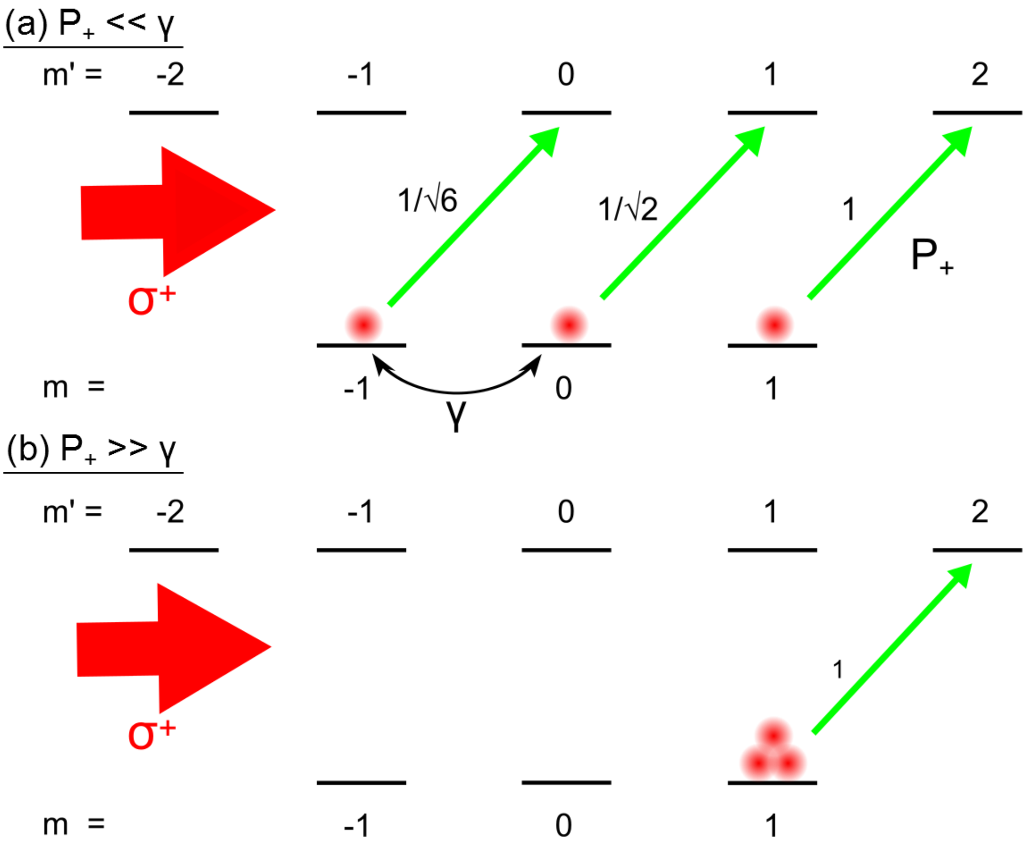

FIGURE 1.2: Kastler diagrams describing optical pumping into the $m = 1$ stretched state. For pump rate $P_+ \gg \gamma$, where γ is the depumping rate, a transfer of population into the $m = 1$ stretched state occurs at timescales of a few scattering rate frequencies. Atoms in stretched states interact more strongly with the light due to higher Clebsch-Gordan coefficients.

Using linear light, a sum of $\sigma^\pm$ components with equal weights, as input, produces a polarization instability. This happens because the two light components have opposite signs of refractive index for a given population distribution. The feedback then causes the two light components to spatially separate as is illustrated in Fig. 1.3. The initial atomic spin fluctuation modulates the phase of the two light components upon traversing the cloud, via the refractive index modulations $\Delta n_\pm$ of $\sigma^\pm$ light. The phase modulations of the circular light components are now shifted by π, i.e. peaks of the spin variable w (defined as the difference between populations in the two stretched states (2.11)) correspond to peaks of the phase modulation of the σ^+ light component $\Delta\varphi_+$ and troughs of $\Delta\varphi_-$. The phase to amplitude conversion via the Talbot effect then converts the phase $\Delta\varphi_\pm$ modulations into amplitude modulations $\Delta P_\pm$, reinforcing the initial modulation in atomic spin, thus closing the feedback loop. The excess positive (negative) light in the transverse plane is then effectively localized in regions of positive (negative) spin, allowing for in-situ imaging of atomic magnetization by simple near-field imaging of the transverse profile of the circular light polarization components inside the cloud. Different techniques such as time-of-flight [55] and Bragg diffraction [56] could also be used to probe the magnetic ordering inside a cloud of ultra-cold atoms.

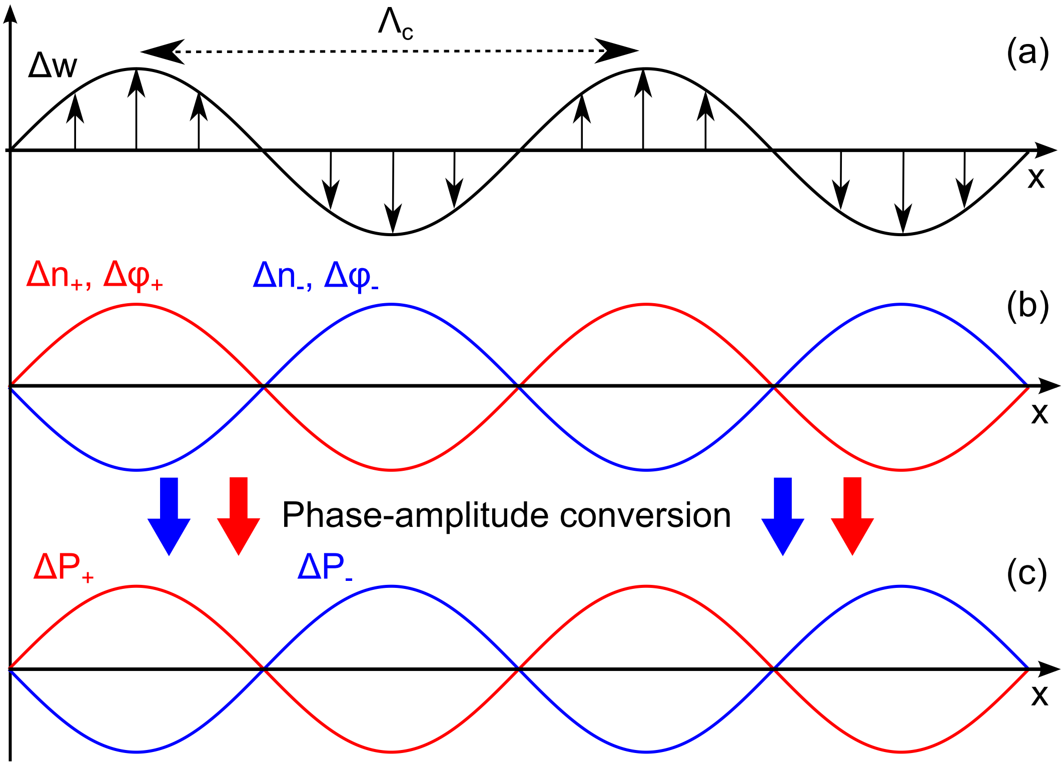

FIGURE 1.3: Ordering of the atomic spins in the single-mirror feedback configuration. (a) a modulation Δw with a critical wavelength Λ_c of the spin variable $w = \rho_{1,1} - \rho_{-1,-1}$ (where $\rho_{1,1}$ and $\rho_{-1,-1}$ are the populations of the two stretched states, as defined in Sec. 2.1.2) converts to a (b) refractive index $\Delta n_\pm$ modulation which causes a phase modulation $\Delta\varphi_\pm$ of the two circular beam components $\sigma^\pm$ traversing the cloud. Diffraction to the mirror and back causes the phase modulation to convert to an (c) amplitude modulation $\Delta P_\pm$.

1.3 Describing systems driven out of thermodynamic equilibrium

1.3.1 Dynamical systems theory

Systems driven far from equilibrium exhibit transitions from homogeneous into non-trivially ordered states, which typically break the symmetry of the initial system. The process of self-organization of these ordered states is commonly referred to as pattern formation. A common way to describe pattern formation is by using the concepts of the branch of mathematics known as dynamical systems theory. The main question of this approach is: what happens to a point in phase space as time progresses? This in practice amounts to writing and solving a set of non-linear partial differential equations describing the "microscopic" dynamics of the system. The microscopic equations do not need to model the system down to the atomic level, as is exemplified in studies of fluid dynamics, where Navier-Stokes equations are used as the dynamical equations. The basics of dynamical systems approach are outlined in great detail in numerous introductory textbooks, such as the ones by Strogatz [57], Guckenheimer and Holmes [58], and review articles, such as the one by Cross and Hohenberg [59].

As non-linear differential equations are in most cases impossible to solve analytically, techniques of dynamical systems theory can provide some understanding of the system properties, e.g. stability of the homogeneous solutions to perturbation [59, 60]. Another great advantage of the approach is the universality of techniques and approximations used to solve the dynamical equations. This however often comes at a cost of obfuscating the physical mechanisms at play, and insight can be gained by augmenting the dynamical analysis with a description based on non-equilibrium statistical physics, or even simple phenomenological approaches. In addition to that, dynamical systems modeling relies greatly on use of computer simulations, which means the behavior of larger systems with stronger interactions is in general more computationally expensive to model.

Dynamical systems can be divided into two classes: *conservative* (Hamiltonian), where the available phase space volume is conserved during temporal evolution and *dissipative*, where the available phase space contracts to zero during temporal evolution. The work presented in this Thesis deals with an example of a *driven dissipative* system, where a *steady state* is reached when the input (driving) energy exactly compensates for the energy dissipated by the decay processes inside the system.

1.3.2 Attractors

Although closed form solutions of coupled non-linear differential equations are rare, the qualitative understanding of the nature of the steady state solutions and system dynamics is in many cases readily achievable. Starting from given initial conditions, a dynamical system evolves towards an *attractor*, constituting a portion of the phase space. A regular *attractor* has a simple geometrical shape, typically a *fixed point*, *limit cycle* or a *torus*, whereas a chaotic attractor possesses unusual geometric properties [38].

A stable fixed point attractor is an equilibrium point in phase space stable to small disturbances [57], which is why it is sometimes referred to as the steady state solution. In addition to stable fixed point attractors, a system can possess an unstable fixed point attractor, which is a point in phase space away from which the system tends to move. An example of a system evolving towards a stable fixed point attractor is an overdamped oscillator, which at long timescales evolves towards a stationary state of lowest energy. Limit cycles constitute closed orbits in phase space, and are characteristic solutions of periodically oscillating systems, with the paradigmatic example being the non-damped harmonic oscillator.

Systems driven out of thermodynamic equilibrium, such as the one studied in this Thesis, commonly tend towards stable fixed point attractors. One example of such solutions are the aforementioned patterned states, appearing commonly in driven systems with dissipation. The first study of pattern formation was performed by

Turing in 1952 [61], in a paper modeling reaction-diffusion processes relevant for biological stucture formation. Pattern formation has since been studied under various names such as dissipative structures formation [62], synergetics [63] and self-organization [64]. The range of systems where pattern formation was observed is exceptionally broad, including, among others, hydrodynamical, chemical, optical and biological systems [59]. This point conveniently illustrates the fact of universal applicability of dynamical systems theory. The universality of pattern formation processes allows for using optical systems as testbeds for studying the general properties of driven systems dynamics in a well controlled setting [60].

1.3.3 Bifurcations

Behavior of a dynamical system often depends critically on its parameters. An important element in studying driven systems is the concept of a bifurcation, which can be defined as a qualitative change occuring due to a change in one or more system parameters. The said change most commonly constitutes a creation, destruction or a change in the stability of the fixed points of the system.

There are three kinds of most commonly occurring bifurcations: *saddle node*, *tricritical* and *pitchfork*. A *saddle node* bifurcation is characterized by a creation or a destruction of a fixed point above a critical parameter value. In a *tricritical* bifurcation, a given fixed point changes stability at the critical parameter value. An example of a *tricritical* bifurcation occurs in the simple model of a solid state laser, where a non-zero photon (i.e. lasing) solution is found after the pump parameter exceeds the critical value [57]. The bifurcation most relevant for the system in this Thesis is the *pitchfork* bifurcation. A *pitchfork* bifurcation commonly occurs in systems possessing symmetries, and is characterized by a creation of multiple fixed points upon exceeding the critical parameter value.

There are two qualitatively different kinds of *pitchfork* bifurcations: *supercritical* and *subcritical*. In a *supercritical* bifurcation, at a critical point two stable and one unstable fixed points arise from a single stable point. *Supercritical* phase transitions are known to occur in statistical models of magnetization [57], and in some cases analogies can be found with the second order phase transitions familiar in thermodynamics [59]. Typically, *subcritical* bifurcations are characterized by an existence of one stable and two unstable solutions below threshold, and a single unstable solution above it.

The two types of bifurcations relevant for the pattern forming system studied in this Thesis are depicted in Fig. 1.4. The first figure shows a *supercritical* bifurcation, with its two symmetric stable branches with a finite order parameter, which can be loosely defined as a measure of order in the system and is the state variable of interest in the present description, and an unstable branch arising continuously from the zero amplitude stable branch as the critical parameter ϵ (for definition see next Section) crosses its zero value. Below threshold the system is in the state with zero order parameter, whereas above threshold, the system selects a solution with a finite order parameter. The order increases continuously with increasing the control parameter, as is the case for the zero longitudinal B-field results of Chapter 4. The order parameter in this case is the diffracted light power, while the control parameter is the pump beam intensity.

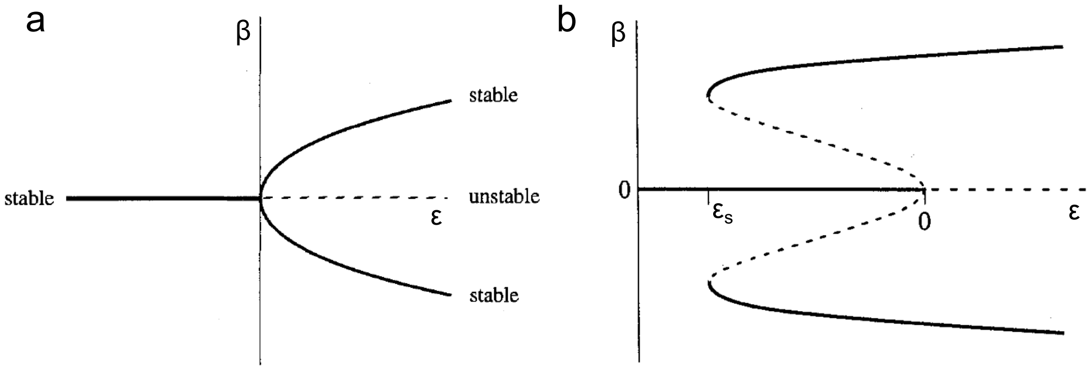

FIGURE 1.4: Dependence of the order parameter β on the control parameter ϵ for the (a) supercritical and (b) subcritical bifurcation. Solid lines indicate stable fixed points and dashed lines indicate unstable fixed points. The Figure is modified from Ref. [57].

The second figure shows a variant of *subcritical* bifurcation with a *saddle point* bifurcation. The *saddle point* bifurcation occurs at the point $\epsilon = \epsilon_s$, where two new stable fixed points with finite order parameters appear from a single stable fixed point. The *subcritical* bifurcation occurs at $\epsilon = 0$, where the zero order parameter stable fixed point disappears, and the system selects a stable fixed point with finite order parameter. The behavior of this type of systems is highly dependent on the direction of the change of the control parameter. For increasing ϵ, the system stays in the zero order parameter state until $\epsilon = 0$, and then abruptly jumps into a finite order parameter state. For decreasing ϵ, the system stays in the finite order parameter state until $\epsilon = \epsilon_s$, and then jumps into the zero order parameter state. This type of phenomenon is called hysteresis, and produces discontinuous jumps of the order parameter upon scanning the control parameter in a single direction, as seen in the finite longitudinal B-field case of Chapter 4. In general, *subcritical* transitions can be mapped to first order phase transitions of thermodynamical systems.

1.3.4 Linear stability analysis

Linear stability analysis is a useful technique for analysing the stability of dynamical systems. The approach is based on analysing the stability of a homogeneous (steady state) solution of the dynamical system of equations to small perturbations, for a given value of the parameters. As was noted above, the occurrence of an instability (bifurcation) is parametrized by a control parameter λ, setting the strength of external driving, exceeding a critical value λ_c. For this purpose one can introduce a dimensionless quantity ϵ

$$\epsilon = \frac{\lambda - \lambda_c}{\lambda_c} \tag{1.6}$$

and a transition is predicted to occur for $\epsilon \geq 0$.

In a generic case, the evolution of the system variables $E(\mathbf{r}, t)$ (vector) is described by the equation

$$\frac{\partial E}{\partial t} = G[E, \partial_{\mathbf{r}}, \partial_{\mathbf{r}}^2, \epsilon], \tag{1.7}$$

where the functional G depends on the system variables E, its derivatives and a parameter ϵ. In general G is a functional of orders higher than the first in E, i.e. the dynamical system is non-linear.

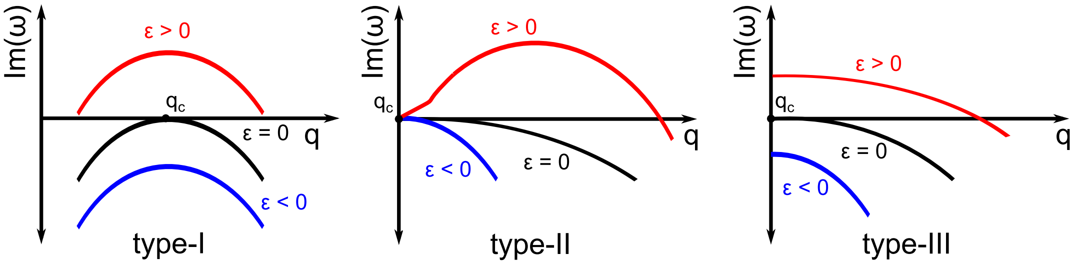

FIGURE 1.5: Growth rates $\mathrm{Im}(\omega)$ vs. pattern wavevector q for three types of instabilities, see text. The ϵ variable is defined as in Eq. (1.6). The Figure is modified from Ref. [59].

Linear stability analysis consists of perturbing the homogeneous solutions $E_j = E_0^j$ with small perturbations $e(\mathbf{r}, t)$, putting the perturbed system variables to $E(\mathbf{r}, t) = E_0 + e(\mathbf{r}, t)$ into the evolution equations and keeping only linear terms in the perturbation. The perturbation modes have a generic form

$$e_j(\mathbf{r}, t) = e_j^0 e^{i\mathbf{q}\cdot\mathbf{r} - i\omega t}, \tag{1.8}$$

where $\mathbf{q}$ is the transverse perturbation wavevector, $\mathrm{Re}(\omega)$ determines the perturbation frequency and $\mathrm{Im}(\omega)$ its growth rate [59]. The subject of this Thesis are stationary patterns, for which $\mathrm{Re}(\omega) = 0$. Upon the said linearization, the dynamical equations have the form

$$\frac{\partial E}{\partial t} = A \cdot E, \quad A_{i,j} = \left.\frac{\delta G_i}{\delta e_j}\right|_{E=E_j^0}, \tag{1.9}$$

with a set of eigenvalues $\omega_i(\mathbf{q})$. From this set one can select a particular branch $\omega(\mathbf{q})$, e.g. the one with the highest growth rate, and study the threshold properties for pattern formation. Typically, the threshold properties are studied with respect to varying the control parameter ϵ, as defined in (1.6).

As depicted in Fig. 1.5 for a 1D case where $\mathbf{q} \equiv q$, varying the control parameter ϵ changes the shape of the imaginary part of $\omega(\mathbf{q})$. The critical parameter λ_c in (1.6) is the lowest λ value for which the curve $\mathrm{Im}(\omega)$ crosses the zero of the y axis. The critical wavevenumber q_c is defined as the wavenumber for which this happens. As the perturbations depend on time as $e_j \sim \exp(-i\omega t)$, $\mathrm{Im}(\omega(q))$ determines the stability condition of the patterns at a given wavenumber q, by determining whether the the perturbations will exponentially decrease ($\mathrm{Im}(\omega(q)) < 0$), increase ($\mathrm{Im}(\omega(q)) > 0$) or be marginally stable ($\mathrm{Im}(\omega(q)) = 0$), i.e. neither grow nor decay in time. Below a critical point ($\epsilon < 0$), the perturbations decay to zero. At $\epsilon = 0$, the perturbations are marginally stable. For $\epsilon > 0$ there is a region of q values where $\mathrm{Im}(\omega) > 0$, and perturbations grow exponentially with time.

Depending on the value of the critical wavevector q_c, three different types of instability can occur. If the dispersion curve for $\epsilon = 0$ crosses the the zero of the y-axis at a finite value q_c, the instability is said to be type-I. The threshold solutions of type-I are patterns with symmetries determined by the amplitude equations (see Sec. 4.2). The patterns studied in this Thesis are indeed instabilities of the type-I. This is indicated in the fact that the wavenumber the with highest gain has a finite value, meaning that the patterns, i.e. modes with finite wavenumber, are the preferred solutions of the dynamical system of equations for $\epsilon \geq 0$. For type-II instabilities the lowest wavenumber for which the curve crosses the zero of the y-axis is $q_c = 0$. The maximum gain for $\epsilon = 0$ is thus for the non-patterned solution. However, for increasing the control parameter to values $\epsilon > 0$ there is a bounded region where patterned solutions have the highest gain, and therefore are preferred solutions. For type-III instabilities, the maximum growth rate for all ϵ values and the crossing of the zero of the y-axis both occur at $q_c = 0$. In type-III instabilities the patterns thus do not form as the maximum gain always favours the growth of a non-patterned state.

1.3.5 Pattern symmetry selection

In addition to enabling the prediction of threshold conditions for pattern formation, dynamical systems theory allows for prediction of symmetries of the patterned states. In two-dimensional non-linear systems, wave mixing determines the growth of a superposition of Fourier modes $\sim e^{i\mathbf{q}_i\cdot\mathbf{r}}$, also called roll states or rolls, with a critical wavevector radius $\mathbf{q} = q_c$. At intensities slightly above threshold, only the lowest order (in amplitude) wave mixing terms are relevant, and the total field variable E can be written as a superposition of three roll states with different amplitudes A_i and wavevectors $\mathbf{q}_i$

$$E = E_0 \left(\sum_{i=1}^{3} A_i(\mathbf{r}, t) e^{i\mathbf{q}_i\cdot\mathbf{r}} + c.c. \right), \tag{1.10}$$

where the wavevectors lie on a circle of radius q_c, i.e. $|\mathbf{q}_i| = q_c$. The wave-mixing equations close to threshold have been derived for the SFM configuration in a rigorous manner (for a Kerr medium) by D'Alessandro and Firth in Ref. [65]. Concentrating on the driving of a particular roll state with the label $i = 1$, the equation is [65], [66]

$$\partial_t A_1 = \mu A_1 + \eta_{123} A_2^* A_3^* - \sum_{l=1}^{3} (\gamma_{1l}(\theta_{1l}) |A_l|^2) A_1 + ... \tag{1.11}$$

A simple heuristic reasoning leads to the same equations. This is because the three terms on the RHS are the only possible way to have wave-mixing of three rolls and satisfy the phase matching condition for the two sides of the equation, for all three wavevectors having a length of q_c. As illustrated in Fig. 1.6, for the second term on the RHS of Eq. (1.11), describing three wave mixing, these conditions lead to the equation $\mathbf{q}_1 = -\mathbf{q}_2 - \mathbf{q}_3$. This equality fixes the angles of the roll wavevectors at 120°, causing a pattern with hexagonal symmetry to grow out of the background noise at threshold. Turning the attention to the first and third term, one sees that the phase matching condition is always satisfied, and a pattern with rolls at any angle, with the probability determined by the function $\gamma_{ij}(\theta_{ij})$, can grow at threshold.

The question of which symmetry patterns does the system choose at threshold is thus determined by the existence of inversion symmetry in the non-linear system. It is shown, e.g. in Sec. 5.3 of Ref. [66], that in practice the inversion symmetry is determined by the condition that the equations of montion are invariant to the transformation of the perturbation of the field variable δE: $\delta E \rightarrow -\delta E$. This then implies that the term η_{123} in Eq. (1.11) vanishes for systems with inversion symmetry, and does not vanish for systems with broken inversion symmetry. It is shown in Ref. [66] how the inversion symmetry is then broken if a longitudinal B-field is applied to the optical medium, for an optical transition with a spin 1/2 ground state.

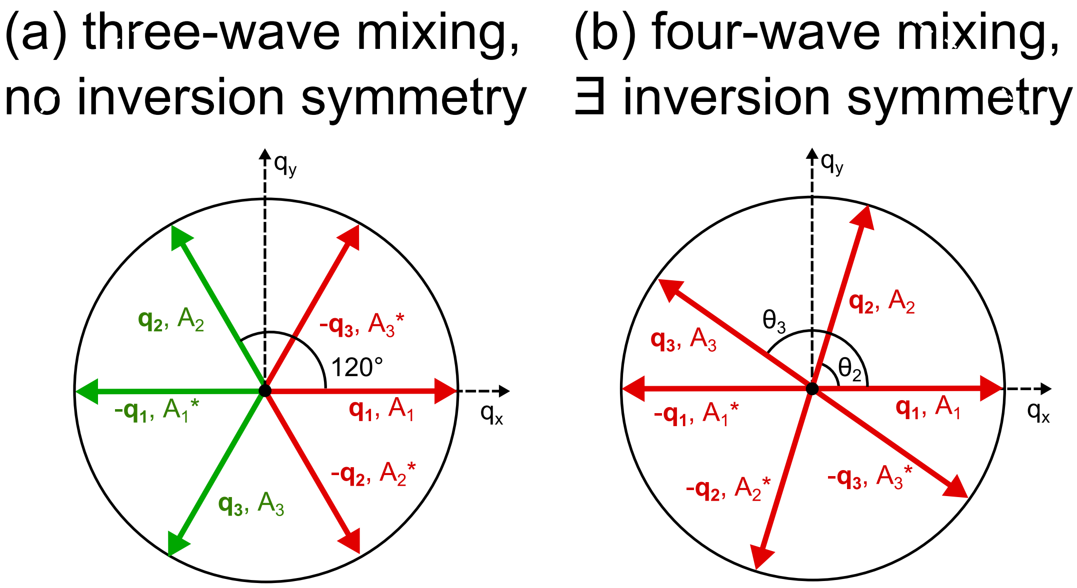

FIGURE 1.6: Selection of pattern symmetries. (a) the case of broken inversion symmetry of the system. (b) the case of preserved inversion symmetry of the system. Red arrows indicate the modes that participate in the amplitude equation for A_1 (1.11), green arrows indicate the modes that do not participate in the amplitude equation for A_1.

Chapter 2

Modeling the atom-light interaction

In this chapter the model of atom-light interaction between the pump laser and the Zeeman sublevels of the atomic medium is presented. The approach is based on Liouville equations for density matrix dynamics under a semiclassical Hamiltonian representing the action of laser driving. As was exemplified by discovery of the Bloch vector picture [67], one advantage of using the density matrix formalism in laser driven systems is that visualizing the dynamics of both diagonal and non-diagonal matrix elements can be done in an intuitive way. In two-level systems the problem is well understood, since the laser field only acts by rotating the 3 component vector made of all the independent density matrix elements. Understanding the dynamics in situations where the atomic Zeeman sublevel structure becomes relevant is a more involved task. For cases when the saturation parameter of the transition is very small, one can neglect the populations and coherences in the excited states and focus only on the dynamics of the ground level density matrix elements. An example of this is the $J = 1/2 \rightarrow J' = 1/2$ transition, which can be simplified to a two level system in the low saturation limit [68, 69, 70]. A common approach used in magnetooptics is the expansion of the ground level density matrix into tensor components with same symmetries as the elements of the electrostatic multipole expansion [71]. The atom-light interaction is then seen to be a consequence of the coupling of the multipole density matrix terms to the electric fields, e.g. spin in the $J = 1/2$ example. The system studied experimentally in this Thesis is the $F = 2 \rightarrow F' = 3$ transition of the D_2 line of ^{87}Rb atoms in the single-mirror feedback configuration. A minimal model of this transition is the $F = 1 \rightarrow F' = 2$ transition, which in the low saturation limit leads to a three ground level system, with multipole expansion terms up to the quadrupolar order. The model will be shown to capture all relevant physics of the magnetization patterns in the single mirror feedback configuration in Chapters 5 and 4. In this Chapter the equations of the $F = 1 \rightarrow F' = 2$ system are presented for the first time. The first Section deals with laying down the theoretical framework of semiclassical light-atom coupling in the density matrix approach and outlines the approximations used for deriving the equations. In the second Section the equations are presented and discussed for cases of only longitudinal B-field present (four equations), and the three-dimensional B-field case (eight equations). The expressions for atom-light coupling to the multipole terms are presented and discussed as well. In the final Section the results of numerical simulations of the full system (with excited state populations and coherences included) are shown to give good agreement to the results of the reduced system of equations for the relevant parameter region.

2.1 Theoretical framework

2.1.1 Semiclassical atom-light interaction

Atom-light interaction is modeled in the semiclassical limit where atomic energy levels are quantized and the laser electric field is classical. A density matrix approach is used to describe the system whose dynamical evolution the Heisenberg picture is described by a Liouville type equation for the density matrix $\hat{\rho} \equiv \rho$ with phenomenological decay and repopulation rates, given by $\hat{\Gamma}$ and $\hat{\Lambda}$ respectively,

$$i\,\hbar\,\frac{d\hat{\rho}}{dt} = [\hat{H}, \hat{\rho}] - i\,\hbar\,\frac{1}{2}(\hat{\Gamma}\,\hat{\rho} + \hat{\rho}\,\hat{\Gamma}) + i\,\hbar\,\hat{\Lambda}. \tag{2.1}$$

The decay matrix is a diagonal matrix with elements proportional to the ground and excited state decay and decoherence rates. The decay rates parametrize the decay of populations, while decoherence rates describe the decay of the off-diagonal (coherence) terms of the density matrix. The repopulation matrix describes the repopulation of the ground level populations and coherences by the decay of the excited levels. Written in this way, following Ch. 3 of Ref. [71], the repopulation matrix $\hat{\Lambda}$ consists of terms proportional to the decay or decoherence rates multiplied by the excited state density matrix elements. The equations for the density matrix elements derived from (2.1) are in the context of atom-light interaction called the *optical Bloch equations*. The density matrix ρ is a matrix with $((2F+1)+(2F'+1))^2$ elements, where $F,\ F'$ are the quantum numbers of the ground and excited state hyperfine angular momenta, so the equation (2.1) turns into a set of $((2F+1)+(2F'+1))^2$ coupled equations for as many density matrix elements (not all independent due to the density matrix being hermitian). The Hamiltonian H includes the electromagnetic dipole interaction between the classical electromagnetic field and the atoms. The level structure of the system is shown in Fig. 2.1, along with optical and magnetic couplings. The optical couplings are denoted by the Rabi frequencies of $\sigma^{\pm}$ circularly polarized light $\Omega_{\pm}$ and the magnetic couplings by the Larmor frequencies $\Omega_{x,y,z}$.

The total Hamiltonian can be divided into three parts

$$\hat{H} = \hat{H}_0 - \hat{\boldsymbol{\mu}}_E \cdot \hat{\mathbf{E}} - \hat{\boldsymbol{\mu}}_M \cdot \hat{\mathbf{B}}, \tag{2.2}$$

where $\hat{H}_0$ is the internal atomic part of the Hamiltonian, $\mathbf{E}, \mathbf{B}$ are electric and magnetic field operators, respectively and

$$\boldsymbol{\mu}_E = \mu_x \hat{\mathbf{x}} + \mu_y \hat{\mathbf{y}}, \quad \boldsymbol{\mu}_M = \mu_M(\hat{\mathbf{x}} + \hat{\mathbf{y}} + \hat{\mathbf{z}}) \tag{2.3}$$

are the electric and magnetic dipole operators (with $\hat{\mathbf{e}}_{\pm} \equiv \hat{\mathbf{e}}_{\pm 1} = \mp(\hat{\mathbf{e}}_x \pm i\hat{\mathbf{e}}_y)/\sqrt{2}$ and $\hat{\mathbf{e}}_x = -(\hat{\mathbf{e}}_+ - \hat{\mathbf{e}}_-)/\sqrt{2}$, $\hat{\mathbf{e}}_y = i(\hat{\mathbf{e}}_+ + \hat{\mathbf{e}}_-)/\sqrt{2}$), where $\mu_{x,y}$ can be expressed as

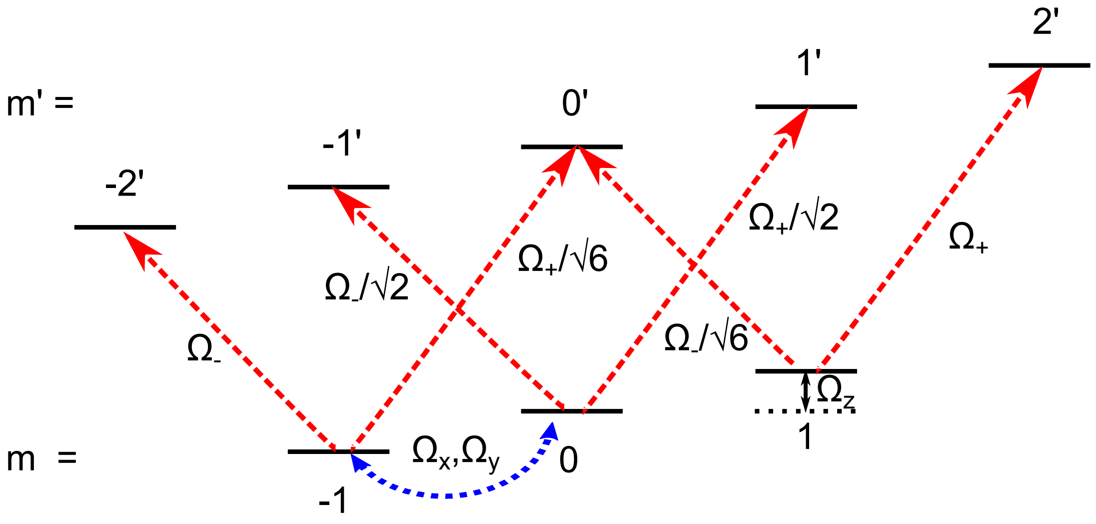

FIGURE 2.1: Hyperfine level structure of the simplified level system. Red dashed arrows: Optical coherences with relevant Clebsch-Gordan coefficients, blue dashed arrow: ground state coherences generated by transverse $B-$fields. Notation: $\Omega_{\pm}$ - Rabi frequencies, $\Omega_{x,y,z}$ - Larmor frequencies.

combinations of transition operators of $\sigma_{\pm}$ transition $\mu_{\pm}$ by

$$\mu_x = -\frac{1}{\sqrt{2}}\left(\mu_+ - \mu_-\right), \quad \mu_y = \frac{i}{\sqrt{2}}\left(\mu_+ + \mu_-\right). \tag{2.4}$$

It is convenient to write the electric field components $E_{\pm}$ in terms of on-resonance Rabi frequencies $\Omega_{\pm} = \frac{\mu_{dip}E_{\pm}}{2\sqrt{5}\hbar}$ where μ_{dip} is the reduced dipole matrix element. The absolute values of Rabi frequencies are related to the intensities of the $\sigma^{\pm}$ beam components as $|\Omega_{\pm}| = \Gamma_2\sqrt{\frac{I_{\pm}}{10I_{sat}}}$ where $\Gamma_2 = \frac{\Gamma_1}{2}$ is the optical decoherence rate related to the population decay rate $\Gamma_1 = 2\pi \times 6.066$ MHz and $I_{sat} = 1.669$ mW/cm^2 for circular light probing the $F = 2 \rightarrow F' = 3$ transition of the D$_2$ line of ^{87}Rb for all atoms in the stretched state $|m| = 2$ [22, 72]. The total electric field is given by [68]

$$\mathbf{E}(t) = \frac{1}{2}\sum_{q=\pm 1}(-1)^q E_q(t)\hat{\mathbf{e}}_{-\mathbf{q}}e^{i\omega t} + \text{c.c.} \tag{2.5}$$

Noting that the scalar product of vectors with complex components $\mathbf{a}$ and $\mathbf{b}$ is $(\mathbf{a},\mathbf{b}) = \mathbf{a}^* \cdot \mathbf{b}$, the relationship between the linear and circular electric field components is now given by

$$E_x = \hat{\mathbf{e}}_x^* \cdot \mathbf{E} = -\tfrac{1}{2\sqrt{2}}(E_+ - E_-) + \text{c.c.}, \quad E_y = \hat{\mathbf{e}}_y^* \cdot \mathbf{E} = \tfrac{i}{2\sqrt{2}}(E_+ + E_-) + \text{c.c.} \tag{2.6}$$

The normalized Hamiltonian $\hat{H}/\hbar$ of the system in the rotating wave approximation [22], with both quantization axis and the $B-$field in $z-$direction, is then

$$\begin{pmatrix}
g_g\Omega_z & 0 & 0 & -\Omega_- & 0 & -\frac{\Omega_+}{\sqrt{6}} & 0 & 0 \\
0 & 0 & 0 & 0 & -\frac{\Omega_-}{\sqrt{2}} & 0 & -\frac{\Omega_+}{\sqrt{2}} & 0 \\
0 & 0 & -g_g\Omega_z & 0 & 0 & -\frac{\Omega_-}{\sqrt{6}} & 0 & -\Omega_+ \\
-\Omega_-^* & 0 & 0 & 2g_e\Omega_z - \Delta & 0 & 0 & 0 & 0 \\
0 & -\frac{\Omega_-^*}{\sqrt{2}} & 0 & 0 & g_e\Omega_z - \Delta & 0 & 0 & 0 \\
-\frac{\Omega_+^*}{\sqrt{6}} & 0 & -\frac{\Omega_-^*}{\sqrt{6}} & 0 & 0 & -\Delta & 0 & 0 \\
0 & -\frac{\Omega_+^*}{\sqrt{2}} & 0 & 0 & 0 & 0 & -\Delta - g_e\Omega_z & 0 \\
0 & 0 & -\Omega_+^* & 0 & 0 & 0 & 0 & -\Delta - 2g_e\Omega_z
\end{pmatrix} \tag{2.7}$$

where g_g, g_e are Landé $g-$factors of the ground and excited levels, respectively. The Hamiltonian for the transverse field case is presented in A.2. Inserting the above Hamiltonian and the decay and repopulation rate matrices calculated by the AtomicDensityMatrix Mathematica package [71] into Equation (2.1) gives a system of 64 coupled differential equations for all of the density matrix elements. In Sections 2.2.1, 2.2.2 it will be shown how this reduces to systems of 4 (for only longitudinal B-field), and 8 (for a B-field with all three components) differential equations, in the low saturation approximation (see (2.14)).

2.1.2 Multipole decomposition of the density matrix

The description of atom-light interaction can be simplified by decomposing the density matrix in an appropriate basis. In the low saturation parameter limit (see

(2.14)), this basis commonly consists of components of irreducible tensor operators $\mathcal{T}_q^\kappa$ with rank κ [71]. The operators have rotational symmetries of real and imaginary parts of spherical harmonic functions with angular momentum numbers $l = \kappa$ and projection numbers $m = q$. Formally, the decomposition of a density matrix ρ describing a state with angular momentum F is written as

$$\rho = \sum_{\kappa=0}^{2F} \sum_{q=-\kappa}^{\kappa} \rho_q^\kappa \mathcal{T}^{q\kappa}, \tag{2.8}$$

where ρ_q^κ (scalar in Hilbert space) are called state multipoles of the density matrix and $\mathcal{T}^{q\kappa}$ is the contravariant [73] irreducible tensor operator. It is shown in Sec. 2.3.1 of Ref. [71] that the state multipoles are superpositions of density matrix elements $\rho_{m'm}$ written in the basis of *eigenvectors* of the B_z-field operator given by

$$\rho_q^\kappa = \mathrm{Tr}(\rho \mathcal{T}_q^\kappa) = \sum_{mm'} (-1)^{F-m'} \langle F, m; F, -m' | \kappa, q \rangle \rho_{m'm}, \tag{2.9}$$

which gives a convenient way to construct the state multipoles. The covariant $\mathcal{T}_q^\kappa$ and contravariant [73] tensor operators are related via the formula $\mathcal{T}_q^{\kappa\dagger} = (-1)^q \mathcal{T}_{-q}^\kappa = \mathcal{T}^{\kappa q}$ [71]. For $F = 1$ Zeeman ground sublevel system, the terms are: rank-0 (one component), rank-1 (three components) and rank-2 (five components). The tensors are commonly referred to in analogy with electrostatic multipole expansion terms as [71]: monopole (or population), dipole (or orientation, related to ρ_q^1) and quadrupole (or alignment, related to ρ_q^2), respectively. The rank zero tensor is the sum of ground state populations which is equal to 1 in the low saturation approximation. The components of the rank 1 and rank 2 tensors are

$$\begin{aligned}
&\rho^1_{-1} = -\tfrac{1}{2\sqrt{2}}(y_1 + z_1 + i(y_2 + z_2)),\\
&\rho^1_0 = \tfrac{1}{\sqrt{2}}w,\\
&\rho^1_{+1} = \tfrac{1}{2\sqrt{2}}(y_1 + z_1 - i(y_2 + z_2)),\\
&\rho^2_{-2} = \tfrac{1}{2}(u + iv),\\
&\rho^2_{-1} = \tfrac{1}{2\sqrt{2}}(z_1 - y_1 + i(z_2 - y_2)),\\
&\rho^2_0 = \tfrac{1}{\sqrt{6}}x,\\
&\rho^2_{+1} = \tfrac{1}{2\sqrt{2}}(y_1 - z_1 + i(z_2 - y_2)),\\
&\rho^2_{+2} = \tfrac{1}{2}(u - iv),
\end{aligned} \tag{2.10}$$

where the atomic variables used throughout this Thesis are

$$\begin{aligned}
&u = \rho_{-11} + \rho_{1-1},\\
&v = i(\rho_{-11} - \rho_{1-1}),\\
&w = \rho_{11} - \rho_{-1-1},\\
&x = \rho_{11} + \rho_{-1-1} - 2\rho_{00},\\
&y_1 = \rho_{-10} + \rho_{0-1},\\
&z_1 = \rho_{01} + \rho_{10},\\
&y_2 = i(\rho_{-10} - \rho_{0-1}),\\
&z_2 = i(\rho_{01} - \rho_{10}).
\end{aligned} \tag{2.11}$$

The terms most relevant for pattern formation studies performed in this Thesis are the orientation w, alignment x and coherences u and v.

For comparison, components of the $F = 2$ ground state system can now be calculated. Using the formula (2.8), the reduced density matrix components of $F = 2$

system up to quadrupole term are now

$$\begin{aligned}
\rho^1_{-1} &= -\tfrac{1}{\sqrt{5}}(\rho_{-1-2} + \sqrt{\tfrac{3}{2}}\rho_{0-1} + \sqrt{\tfrac{3}{2}}\rho_{10} + \rho_{21}),\\
\rho^1_0 &= -\tfrac{1}{\sqrt{10}}(2\rho_{22} + \rho_{11} - 2\rho_{-2-2} - \rho_{-1-1}),\\
\rho^1_{+1} &= \tfrac{1}{\sqrt{5}}(\rho_{-2-1} + \sqrt{\tfrac{3}{2}}\rho_{-10} + \sqrt{\tfrac{3}{2}}\rho_{01} + \rho_{12}),\\
\rho^2_{-2} &= \sqrt{\tfrac{2}{7}}(\rho_{0-2} + \sqrt{\tfrac{3}{2}}\rho_{1-1} + \rho_{20}),\\
\rho^2_{-1} &= -\tfrac{3}{\sqrt{7}}(\rho_{-1-2} + \sqrt{\tfrac{1}{6}}\rho_{0-1} - \sqrt{\tfrac{1}{6}}\rho_{10} - \rho_{21}),\\
\rho^2_0 &= \sqrt{\tfrac{2}{7}}(\rho_{-2-2} - \tfrac{1}{2}\rho_{-1-1} - \rho_{00} - \tfrac{1}{2}\rho_{11} + \rho_{22}),\\
\rho^2_{+1} &= \tfrac{3}{\sqrt{7}}(\rho_{-2-1} + \sqrt{\tfrac{1}{6}}\rho_{-10} - \sqrt{\tfrac{1}{6}}\rho_{01} - \rho_{12}),\\
\rho^2_{+2} &= \sqrt{\tfrac{2}{7}}(\rho_{-20} + \sqrt{\tfrac{3}{2}}\rho_{-11} + \rho_{02}).
\end{aligned} \tag{2.12}$$

An inspection of expressions (2.12) and (2.10) shows that the corresponding density matrix multipole expansion elements are equivalent, in the sense that each multipole element is equal to the $F = 1$ term but with extra terms added due to higher number of levels in the $F = 2$ case, and the numerical prefactors resulting from the different Clebsch-Gordan coefficients in the two cases.

The usefulness of density matrix decomposition in irreducible tensor basis is evident when one considers the angular momentum probability surface, defined as the probability of finding the system in the maximum projection state along axis with angles (θ, ϕ) with respect to the z-axis

$$\rho_{FF}(\theta,\phi) = \langle FF(\theta,\phi)|\rho|FF(\theta,\phi)\rangle. \tag{2.13}$$

Using the above expression with (2.8), and recalling that the symmetry of the matrix element $\langle FF(\theta,\phi)|\mathcal{T}^{q\kappa}|FF(\theta,\phi)\rangle$ is determined by real and imaginary parts of spherical harmonic functions $Y^{\kappa}_q(\theta,\phi)$, one can visualize the atomic polarization for a system described by a given state multipole ρ^{κ}_q (or a superposition thereof). The symmetries are important as they determine the anisotropy of optical properties such as absorption and refractive index.

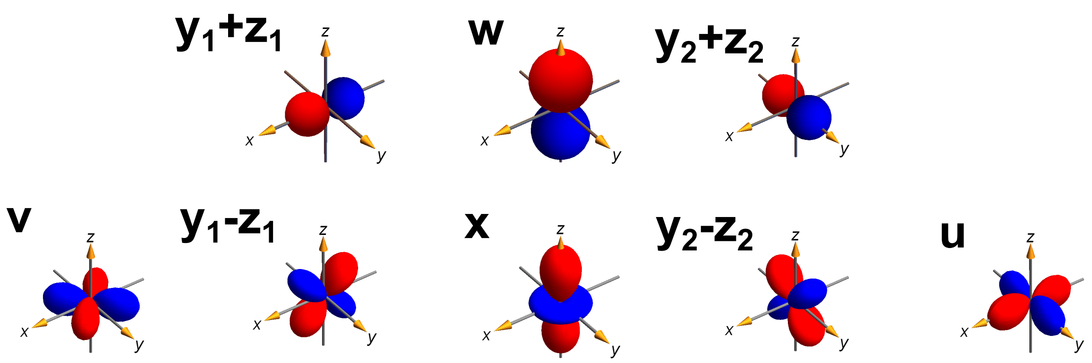

FIGURE 2.2: Spherical harmonics determining the symmetry of irreducible tensor components related to the indicated state multipoles. Red: positive, blue: negative values.

Spherical harmonic functions related to corresponding state multipoles of the $F = 1$ system are shown in Fig. 2.2. The dipole terms (orientation) are in the first row, while the quadrupole (alignment) terms are in the second. From the graphical representation it is evident that the dipole terms have both preferred axes and directions, whilst quadrupole terms have only preferred axes. Neglecting multipole terms in derivation of the system dynamics, described in Sec. 2.1.3 can now be explained from symmetry considerations. For the case when only B-field in the z-direction is present, optical pumping can drive w and x but cannot drive $y_1 \pm z_1$ and $y_2 \pm z_2$. The moments u and v are then not equal to zero because they are not driven directly by optical pumping but by the Raman-like two-level transition (in case of linearly polarized light). When either or both x and y $B-$fields are present, terms $y_1 \pm z_1$ and $y_2 \pm z_2$ can not be neglected because atoms polarize along other directions than z.

2.1.3 Deriving the equations

Patterns are observed in the low saturation limit where the detuned saturation parameter is

$$s(\Delta) = \frac{I}{I_{sat}} \frac{1}{1 + \left(\frac{\Delta}{\Gamma_2}\right)^2} \ll 1, \tag{2.14}$$

where I_{sat} is the saturation intensity of the transition, Δ is the beam detuning and Γ_2 is the optical decoherence rate. In the experiments, low saturation is achieved for high intensities by detuning the beam by $|\Delta| > 10\ \Gamma_2$ from resonance. As the excited state population of each of the two-level transitions is given by $\rho_{ee} = \frac{1}{2}\frac{s}{1+s}$ [22], this means that in first approximation the excited state populations can be neglected relative to ground state populations. Additional simplification comes from the fact that the optical coherences between excited and ground states created by the laser evolve on much faster timescales than the ground state populations and coherences, meaning that they can be adiabatically eliminated [68]. The adiabatic elimination is a way of reducing the number of temporally varying degrees of freedom in a system with multiple characteristic timescales.

The apparent difference of the system used in experiments with the theoretical model is the simplification from $F = 2 \to F' = 3$ to $F = 1 \to F' = 2$ transition. This however has proven not to be relevant, and even good quantitative agreement of simulation and experimental results is seen. The practice of using simplified models not exactly matching the experimental atomic transition is well known in atomic physics, with the most notable example being the work of Ref. [74] describing Sysiphus cooling. An advantage of using the simplified $F = 1 \to F' = 2$ system is in reducing the number of coupled differential equations from 24 to 8, which in turn reduces the computation time. This is important since e.g. in 2D simulations one deals with grids of 128×128 sites which are mutually interacting via mirror feedback. The reasons why even simpler models were not used are the following. The non-linearity in $F = 2 \to F' = 3$ is based on optical pumping into bright stretched states, and is therefore self-focusing, as is revealed by the lengthscale vs. mirror distance scan (see Fig. 6.2). This excludes models such as $F = 1/2 \to F' = 1/2$ and $F = 1 \to F' = 0$ for which pumping into dark state occurs. The simplest model where a pumping into the bright state occurs is $F = 1/2 \to F' = 3/2$. This model was used e.g. in investigations of the Gauthier group to explain the atom bunching induced optical non-linearity simultaneously cooling and polarizing the atoms [16, 17]. The emphasis of these papers was however on studying the effects of cooling of the atoms in a self-organized lattice, and no systematic investigation of polarization of the light scattered off the patterns was performed. The model has proved insufficient to explain some of the properties of the patterns reported in this Thesis, such as e.g. the B_z scan displayed in Fig. 4.8 of Ch. 4, so the next simplest model was needed. This is indeed the $F = 1 \rightarrow F' = 2$ transition.

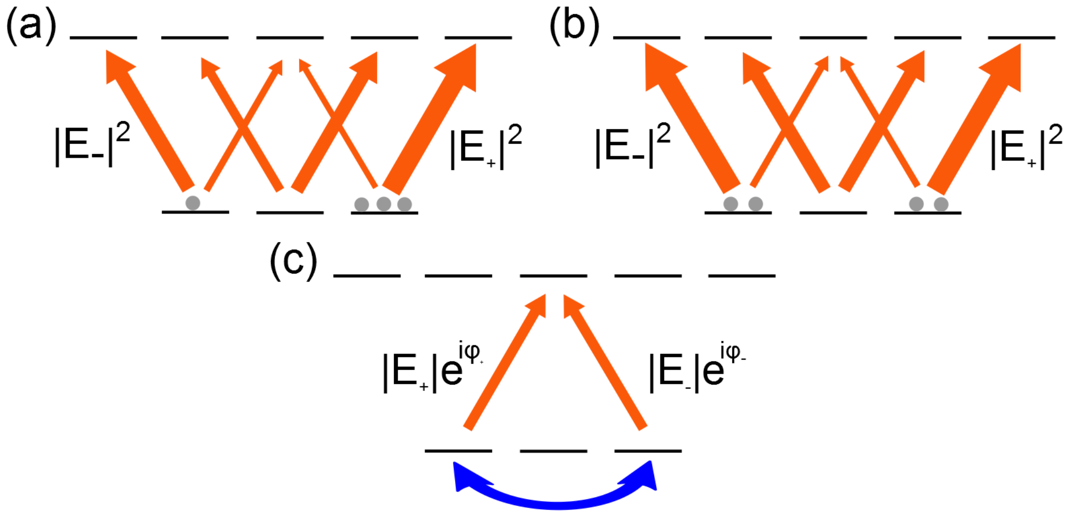

FIGURE 2.3: Schematics of optical driving of (a) orientation w, (b) alignment x and (c) ground state coherence terms u, v. The thickness of the arrows represents schematically the strength of the optical coupling of the ground and excited states. The dots represent schematically the populations in the stretched ground states, which is higher in the $m = 1$ state in case (a), equal in case (b) and not relevant in case (c). The orientation and alignment are driven by difference and sum of intensities, respectively, whereas the ground state coherence is driven by a phase sensitive multiplication of the electric fields of the form $|E_+||E_-|\exp i(\varphi_- - \varphi_+)$, where $|E_\pm|$ are amplitudes and $\varphi_\pm$ are phases of the circular components of the laser field.

There are three main quantities describing the atomic system: stretched state population difference (orientation w), stretched state and $m = 0$ state population difference (alignment x) and $\Delta m = 2$ ground state coherence (with real part u and imaginary part v), which couple to the light directly and determine the optical properties of the beam after the cloud. The mechanisms of optical driving of these multipoles are depicted in Fig. 2.3. The orientation is driven by the difference in the intensities of + and - circularly polarized light components $\sim |E_+|^2 - |E_-|^2$, while alignment is driven by the sum of the + and - light components $\sim |E_+|^2 + |E_-|^2$ i.e. either of them. The ground state coherence is on the other hand driven by real and imaginary parts of a phase sensitive multiplication of electric fields $E_+^* E_-$.

The $|\Delta m| = 1$ ground state coherences are neglected in cases when there is no transverse $B-$fields present, contrary to $|\Delta m| = 2$, which can have large values due to presence of Raman coupling. This coherence $|\Delta m| = 2$ is driven by phase sensitive pump rates which also regulate the coupling with orientation w and alignment x, as will be shown in Sec. 2.2. The driving term for w is $\mathcal{O}(B_z)$ for $|E_+| = |E_-|$ (linear input light), whereas the driving terms of other variables are $\mathcal{O}(1)$ in B_z field. The fact that the driving terms operate on *zero background* means the atomic variables are sensitive to small changes in them. The influence of B_z thus cannot be neglected for w equations, but can for the others. For reasons of mathematical convenience, B_z is neglected only for $|\Delta m| = 2$ ground state coherence, while w and x keep the dependence. The decay terms of the excited states, giving a transfer of population from excited to ground states, also operate on zero background so excited state populations and coherences cannot be neglected when they drive the ground state variables, and are thus adiabatically eliminated. The final approximation is in the Landé g-factors of ground and excited levels. In Refs. [23, 70], best quantitative agreement with experiment was seen when g-factors of the simplified system were equal to the g-factors of the transition excited in the experiment. For D_2 line of ^{87}Rb this would mean the $F = 2$ ground state factor would be $g_g = 1/2$, and the excited state $F' = 3$ one would be $g_e = 2/3$. For simplicity reasons the g-factors of the ground and excited levels are set to $g_g = g_e = 1$. This induces error on the Faraday rotation phase shift, but the change can only be quantitative as the signs of $g-$factors are equal in the two cases and their difference in the physical transition is $g_e - g_g \approx 0.17$.

A short summary of approximations used in deriving the equations is listed below:

- Excited state populations and coherences are neglected except when on *zero background*, in which cases they are adiabatically eliminated
- Optical coherences are adiabatically eliminated

- $|\Delta m| = 1$ ground state coherences are neglected except when transverse $B-$fields are present, $|\Delta m| = 2$ ground state coherences are never neglected
- Larmor frequencies are neglected compared to laser detuning only in the Raman transition pump rates
- Landé g-factors of excited and ground states are taken to be equal to 1

It will be shown that the equations written in this approximation provide good agreement with numerical results of the full system of equations, in the low saturation parameter regime.

2.2 Medium equations

In this Chapter the equations governing the dynamics of the atomic medium and its interaction with the laser field are presented. The details of the derivation can be found in A.1, and the approximations used are shown in 2.1.3.

2.2.1 Longitudinal $B-$field

The only quantities coupling directly to the light in the lowest order approximation are orientation w, alignment x and coherences u and v. Those are also the only quantities that are non-negligible in the case of only Ω_z present. The equations of medium dynamics are the following

$$\begin{aligned}
\dot{u} &= -\Gamma_c u + (2\Omega_z + \tfrac{5}{6}\mathcal{D}\bar{\Delta})v + \tfrac{1}{6}P_{\Lambda-}\bar{\Delta}w - \tfrac{1}{9}P_{\Lambda+}x + \tfrac{5}{18}P_{\Lambda+}, \\
\dot{v} &= -\Gamma_c v - (2\Omega_z + \tfrac{5}{6}\mathcal{D}\bar{\Delta})u + \tfrac{1}{6}P_{\Lambda+}\bar{\Delta}w + \tfrac{1}{9}P_{\Lambda-}x - \tfrac{5}{18}P_{\Lambda-}, \\
\dot{w} &= -\Gamma_w w - \tfrac{1}{6}P_{\Lambda-}\bar{\Delta}u - \tfrac{1}{6}P_{\Lambda+}\bar{\Delta}v - \tfrac{1}{9}\mathcal{D}x + \tfrac{5}{18}\mathcal{D}, \\
\dot{x} &= -\Gamma_x x - \tfrac{1}{3}P_{\Lambda+}u + \tfrac{1}{3}P_{\Lambda-}v + \tfrac{1}{3}\mathcal{D}w + \tfrac{5}{18}\mathcal{S}.
\end{aligned} \tag{2.15}$$

The detuning is written in units of coherence decay rate Γ_2 as $\bar{\Delta} = \frac{\Delta}{\Gamma_2}$. The pump rates are given by

$$P_+ = \tfrac{1}{\Gamma_2}\tfrac{|\Omega_+|^2}{1+\frac{(\Delta-\Omega_z)^2}{\Gamma_2^2}}, \quad P_- = \tfrac{1}{\Gamma_2}\tfrac{|\Omega_-|^2}{1+\frac{(\Delta+\Omega_z)^2}{\Gamma_2^2}}, \tag{2.16}$$

Driving terms are then given by

$$\begin{aligned} \mathcal{S} &= P_+ + P_-, & \mathcal{D} &= P_+ - P_- \\ P_{\Lambda+} &= \tfrac{1}{\Gamma_2}\tfrac{1}{1+\left(\frac{\Delta}{\Gamma_2}\right)^2}\left(\Omega_+^*\Omega_- + \Omega_+\Omega_-^*\right), & P_{\Lambda-} &= \tfrac{i}{\Gamma_2}\tfrac{1}{1+\left(\frac{\Delta}{\Gamma_2}\right)^2}\left(\Omega_+^*\Omega_- - \Omega_+\Omega_-^*\right). \end{aligned} \tag{2.17}$$

Finally, the decay rates of the atomic variables are

$$\Gamma_c = \gamma_1 + \frac{7}{6}(P_+ + P_-) - \frac{1}{3\Gamma_2}\frac{1}{1+\left(\frac{\Delta}{\Gamma_2}\right)^2}(|\Omega_+|^2 + |\Omega_-|^2),$$

$$\Gamma_w = r + \tfrac{1}{6}(P_+ + P_-), \quad \Gamma_x = r + \tfrac{11}{18}(P_+ + P_-), \tag{2.18}$$

where γ_1 is the ground state decoherence rate and r is the ground level depumping rate. The two rates will in general be taken to be equal in simulations. The origin of the decay rates γ_1 and r in hot vapors is the motion of atoms out of the laser beam, however in a typical cold atomic setup the rates are limited by the stray transverse B-fields ($\gamma_1,\ r \sim 2\pi \times 14$ kHz for a field of $B_{x,y} \sim 10$ mG, as calculated from Eq. (2.25)). Observing the form of Eq. (2.15), there are immediately some similarities to the $J = 1/2 \to J' = 1/2$ system described in [69]. Firstly, the decay rates of coherences u and v, alignment x and orientation w are proportional to γ_1, r and $\mathcal{S}$, while the driving of w is proportional to $\mathcal{D}$. Also, u and v transiently rotate with frequencies proportional to the Larmor frequency Ω_z and light shift $\mathcal{D}\bar{\Delta}$, analogously to the precession of the $\Delta m = 1$ ground state coherences in the $J = 1/2$ ground level system. This precession in the steady state amounts to a decay with a constant proportional to Ω_z and $\mathcal{D}\bar{\Delta}$. The differences with respect to the $J = 1/2$ system arise from coupling of the four atomic variables. The w variable couples to x, u and v via terms proportional to $\mathcal{D}$, $P_{\Lambda-}\bar{\Delta}$ and $P_{\Lambda+}\bar{\Delta}$, respectively. The x variable is always driven positively by w, whereas the converse is true for the

w variable as is clear from their definitions. The couplings of w to the u and v are mediated by terms with the form of light shift with phase sensitive Raman-type pump rates, whereas for x the couplings are proportional only to phase sensitive pump rates, i.e. without $\bar{\Delta}$. Real part of the ground state coherence is driven by $P_{\Lambda+}$, proportional to the real part of $\Omega_+^*\Omega_-$, whereas the imaginary part of ground state coherence is driven by $P_{\Lambda-}$, proportional to imaginary part of $\Omega_+^*\Omega_-$. An intuitive explanation of the driving terms $P_{\Lambda+}$ and $P_{\Lambda-}$ can be given by recalling that $E_\pm = \mp(E_x \pm iE_y)$. This means that $P_{\Lambda+} = 2\mathrm{Re}(\Omega_+^*\Omega_-) \sim (E_x^2 - E_y^2)$ and $P_{\Lambda-} = -2\mathrm{Im}(\Omega_+^*\Omega_-) \sim 4E_xE_y$. The driving of the u variable will thus be strongest for light linearly polarized along the x or y axis, whereas the driving of the v variable will be strongest for light polarized at 45° to these axes. This is in accordance with Fig. 2.2 where it is shown that the u variable is aligned along the x and y axes whereas the v is aligned at an angle of 45° with respect to the two axes.

2.2.2 Transverse $B-$fields

In order to fully account for behavior of the patterns the full three dimensional $B-$field needs to be included into the model. In this case, the system of equations (2.15) is augumented by four additional equations, meaning all multipoles of the irreducible tensor decomposition depicted in Fig. 2.2 are taken into account. The Hamiltonian is too involved to be written here and is instead given in Section A.1 of the Appendix by eq. (A.3). From (A.3) it is evident the field parallel to the linear light polarization (B_x) and the one orthogonal to it (B_y) are not treated on the same footing, namely there is a $\pi/2$ phase difference between the Larmor frequencies of the two fields. The equations when all three $B-$field components are present are then

$$
\begin{aligned}
\dot{u} &= -\Gamma_c u + \left(2\Omega_z + \tfrac{5}{6}\mathcal{D}\bar{\Delta}\right) v + \tfrac{1}{6}P_{\Lambda-}\bar{\Delta}w - \tfrac{1}{9}P_{\Lambda+}x + \tfrac{5}{18}P_{\Lambda+} - \tfrac{\Omega_x}{\sqrt{2}}(z_2 - y_2) + \tfrac{\Omega_y}{\sqrt{2}}(z_1 - y_1),\\
\dot{v} &= -\Gamma_c v - \left(2\Omega_z + \tfrac{5}{6}\mathcal{D}\bar{\Delta}\right) u + \tfrac{1}{6}P_{\Lambda+}\bar{\Delta}w + \tfrac{1}{9}P_{\Lambda-}x - \tfrac{5}{18}P_{\Lambda-} + \tfrac{\Omega_x}{\sqrt{2}}(z_1 - y_1) + \tfrac{\Omega_y}{\sqrt{2}}(z_2 - y_2),\\
\dot{w} &= -\Gamma_w w - \tfrac{1}{6}P_{\Lambda-}\bar{\Delta}u - \tfrac{1}{6}P_{\Lambda+}\bar{\Delta}v - \tfrac{1}{9}\mathcal{D}x + \tfrac{5}{18}\mathcal{D} - \tfrac{\Omega_x}{\sqrt{2}}(y_2 + z_2) - \tfrac{\Omega_y}{\sqrt{2}}(y_1 + z_1),\\
\dot{x} &= -\Gamma_x x - \tfrac{1}{3}P_{\Lambda+}u + \tfrac{1}{3}P_{\Lambda-}v + \tfrac{1}{3}\mathcal{D}w + \tfrac{5}{18}\mathcal{S} + 3\tfrac{\Omega_x}{\sqrt{2}}(y_2 - z_2) + 3\tfrac{\Omega_y}{\sqrt{2}}(y_1 - z_1),\\
\dot{y_1} &= -\Gamma_y y_1 + (\Omega_z + \bar{\Delta}\mathcal{D}_y)y_2 + \left(\tfrac{P'_-}{6} + \tfrac{1}{12}\left(\bar{\Delta}P_{\Lambda-} - P_{\Lambda+}\right)\right) z_1\\
&\quad + \left(\tfrac{\bar{\Delta}P'_-}{6} + \tfrac{1}{12}\left(\bar{\Delta}P_{\Lambda+} + P_{\Lambda-}\right)\right) z_2 + \tfrac{\Omega_x}{\sqrt{2}}v + \tfrac{\Omega_y}{\sqrt{2}}(w - x + u),\\
\dot{y_2} &= -\Gamma_y y_2 - (\Omega_z + \bar{\Delta}\mathcal{D}_y)y_1 - \left(\tfrac{\bar{\Delta}P'_-}{6} - \tfrac{1}{12}\left(\bar{\Delta}P_{\Lambda+} + P_{\Lambda-}\right)\right) z_1\\
&\quad + \left(\tfrac{P'_-}{6} + \tfrac{1}{12}\left(P_{\Lambda+} - \bar{\Delta}P_{\Lambda-}\right)\right) z_2 + \tfrac{\Omega_x}{\sqrt{2}}(w - x - u) + \tfrac{\Omega_y}{\sqrt{2}}v,\\
\dot{z_1} &= -\Gamma_z z_1 + (\Omega_z + \bar{\Delta}\mathcal{D}_z)z_2 + \left(\tfrac{P'_+}{6} - \tfrac{1}{12}\left(\bar{\Delta}P_{\Lambda-} + P_{\Lambda+}\right)\right) y_1\\
&\quad - \left(\tfrac{\bar{\Delta}P'_+}{6} + \tfrac{1}{12}\left(\bar{\Delta}P_{\Lambda+} - P_{\Lambda-}\right)\right) y_2 - \tfrac{\Omega_x}{\sqrt{2}}v + \tfrac{\Omega_y}{\sqrt{2}}(w + x - u),\\
\dot{z_2} &= -\Gamma_z z_2 - (\Omega_z + \bar{\Delta}\mathcal{D}_z)z_1 + \left(\tfrac{\bar{\Delta}P'_+}{6} - \tfrac{1}{12}\left(\bar{\Delta}P_{\Lambda+} - P_{\Lambda-}\right)\right) y_1\\
&\quad + \left(\tfrac{P'_+}{6} + \tfrac{1}{12}\left(\bar{\Delta}P_{\Lambda-} + P_{\Lambda+}\right)\right) y_2 + \tfrac{\Omega_x}{\sqrt{2}}(w + x + u) - \tfrac{\Omega_y}{\sqrt{2}}v.
\end{aligned}
\tag{2.19}
$$

The newly introduced pump rates and differences are now

$$
\begin{gathered}
P'_+ = \tfrac{1}{\Gamma_2}\tfrac{|\Omega_+|^2}{1+\frac{(\Delta-2\Omega_z)^2}{\Gamma_2^2}}, \quad P'_- = \tfrac{1}{\Gamma_2}\tfrac{|\Omega_+|^2}{1+\frac{(\Delta+2\Omega_z)^2}{\Gamma_2^2}},\\
\mathcal{D}_y = P'_+ - \tfrac{7}{12}P'_-, \quad \mathcal{D}_z = \tfrac{7}{12}P'_+ - P'_-,
\end{gathered}
\tag{2.20}
$$

whereas the rest are given by Eqs. (2.16), (2.17), (2.18). The decay rates of $|\Delta m| = 1$ ground state coherences are

$$
\Gamma_y = \gamma_1 + P'_+ + \tfrac{7}{12}P'_-, \quad \Gamma_z = \gamma_1 + \tfrac{7}{12}P'_+ + P'_-. \tag{2.21}
$$

Orientation in z direction w is coupled to orientations in x direction $y_1 + z_1$ and y direction $y_2 + z_2$ by fields B_y and B_x, respectively. The alignment x and coherences u, v are in turn coupled only to quadrupole moments $y_1 - z_1$ and $y_2 - z_2$ via transverse B-fields. The structure of equations for $y_{1,2}$ and $z_{1,2}$ are reminiscent of the structure of coherences in the two-level $J = 1/2$ system described e.g. in [69]. Using the substitution for dipolar magnetization components: $m_x = u \rightarrow (y_1 + z_1)$, $m_y = v \rightarrow -(y_2 + z_2)$, $m_z = w \rightarrow w$ one recovers the form of equation (10) in [69]. The discrepancies arise due to presence of Raman transition and non-equal Clebsch-Gordan coefficients in the $J = 1$ case. The classical equation for dipole evolution in external B-field proportional to $\mathbf{\Omega}$: $\dot{\mathbf{m}} = \mathbf{m} \times \mathbf{\Omega}$ agrees as well with the B-field interaction terms of Eq. (2.19). Comparison with equations for $J = 1 \to J' = 0$ system, published e.g. in [75] yields similar agreement with quadrupolar terms, giving only discrepancies in numerical prefactors due to different Clebsch-Gordan coefficients.

2.2.3 Optical response

Optical response of the medium is determined by the polarization components $P_\pm$

$$\mathbf{P}(z,t) = \frac{1}{2}\sum_{q=\pm}(-1)^q P_q(z,t)\hat{\mathbf{e}}_{-\mathbf{q}} e^{i\omega t - ikz} + \text{c.c.} \tag{2.22}$$

These components are calculated in A.3 to be given by

$$P_\pm = \varepsilon_0 \chi_l^\pm \left(\left(1 \pm \frac{3}{4} w + \frac{1}{20} x \right) E_\pm + \frac{3}{20}(u \mp iv) E_\mp \right), \tag{2.23}$$

where the linear susceptility $\chi_l^\pm = 2\alpha_l^\pm / k$ is often parametrized via

$$\alpha_l^\pm = -\frac{b_0 \Gamma_2}{2L} \frac{i\Gamma_2 + (\Delta \mp \Omega_z)}{\Gamma_2^2 + (\Delta \mp \Omega_z)^2}. \tag{2.24}$$

The first term on the RHS of the optical response equations (2.23) describes light absorption and phase shift, whereas the second term generates light of opposite circular polarization if a finite $|\Delta m| = 2$ ground state coherence exists. Generation of light of opposite circular polarization by ground state coherences is known to occur in systems exhibiting effects like electromagnetically induced transparency (EIT) and coherent population trapping (CPT) [76]. The input polarization of the experimental pump beam is linear, i.e. with equal amplitudes of σ^+ and σ^- light. The observed patterns are however complementary, i.e. the regions of excess σ^+ and σ^- are spatially separated. The x and u variables treat both circular polarizations the same way, meaning the patterned beam for linear input is still linearly polarized at every point. This means that the instability arising from a modulation in these variables is not a *polarization instability* since there is no gain in the polarization component orthogonal to the input light. As will be discussed in Chapter 5, the main driver of patterns is the spin w instability. The particular dependence of optical response on w is equal (up to the factor 3/4) to the one of Ref. [70], however with the opposite signs due to optical pumping into bright as opposed to dark states. With this response, the two opposite circular polarizations receive phase shifts of equal magnitude but opposite signs which via Talbot diffraction in the SFM configuration converts to complementary modulations of $P_\pm$ pumping and leads to a polarization instability (as outlined in Chapter 1).

2.3 Numerical results

In this Section the steady state numerical solutions of the full system of 64 equations for the $F = 1 \to F' = 2$ transition are compared to the solutions of the reduced system (2.19) with the goal of checking the validity of the approximations used in their derivations. An excellent agreement is found in the experimental region of interest of $|\Delta| > 5\ \Gamma_1$, $|B_{x,y,z}| < 2$ G and $I = 0 - 600$ mW/cm^2 ($\Omega_0 = 0 - 4\ \Gamma_1$). Throughout this Section the Rabi frequencies of $\sigma^\pm$ light $\Omega_\pm$ are expressed in units of two-level Rabi frequency Ω_0 and the B-fields $B_{x,y,z}$ are parametrized via the Larmor frequencies $\Omega_{x,y,z}$. These units are related to the experimentally measured quantities $B_{x,y,z}$ and $I_\pm$ as

$$\Omega_0 = \Gamma_1 \sqrt{\frac{I_\pm}{2I_{sat}}}, \quad \Omega_{x,y,z} = 0.23 \times B_{x,y,z}\, \frac{\Gamma_1}{\mathrm{G}}, \tag{2.25}$$

where the value $I_{sat} = 1.669$ mW/cm^2 for circularly polarized light [72] of the $F = 2 \to F' = 3$ transition in stretched states was used.

2.3.1 Longitudinal B-field

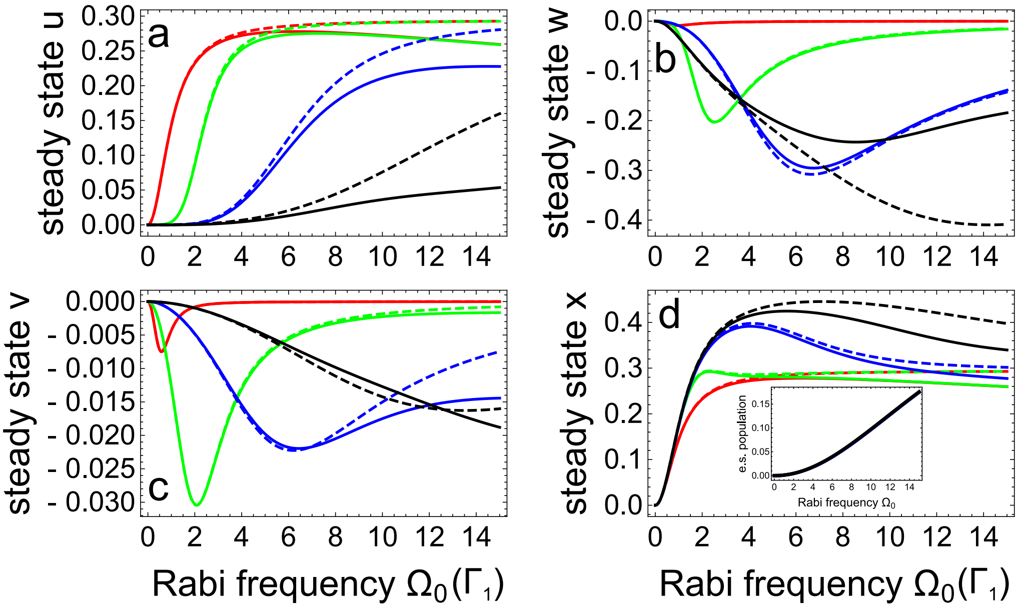

FIGURE 2.4: Steady state atomic variables: (a) real part of ground state coherence u, (b) orientation w, (c) imaginary part of ground state coherence v and (d) alignment x. Inset: total excited state population. Full lines: solutions of the full system of equations. Dashed lines: solutions of the approximate system of equations (2.15). Red: $\Omega_z = 10^{-4}$ ($B_z = 0.4$mG). Green: $\Omega_z = 0.01$ ($B_z = 43.4$mG). Blue: $\Omega_z = 0.1$ ($B_z = 434$mG). Black: $\Omega_z = 0.5$ ($B_z = 2.17$G). The x axis is the Rabi frequency Ω_0 related to the circular components of (2.7) as $\Omega_+ = \Omega_- = \Omega_0/\sqrt{20}$, corresponding to total beam intensity range $I = 0-1.5$ W/cm^2. The beam detuning is $\Delta = -7\Gamma_1$, the ground state decoherence and depopulation rates are $\gamma_1 = r = 10^{-3}\Gamma_1$.

Plots of solutions of the full system of 64 equations and the reduced system (2.15) are shown in Figs. 2.4, 2.5 for linear and elliptical light, respectively. Different colors correspond to different longitudinal B-fields, ranging from $0.0004-2.17$ G. The insets show total population in the excited states, given by $\rho_{2',2'} + \rho_{1',1'} + \rho_{0,0} + \rho_{-1',-1'} + \rho_{-2',-2'}$, which provides a good estimation of departure from the low saturation approximation. From the two plots it is evident that the departure from low saturation begins when total excited state populations exceed 5% but the approximation is still reasonably valid for values up to 10%. The agreement is very good in the experimental region of interest, i.e. $I = 0-150$ mW/cm^2, $\Delta = -10 - -5\Gamma_1$ and moderately good up to ~ 1.5 W/cm^2.

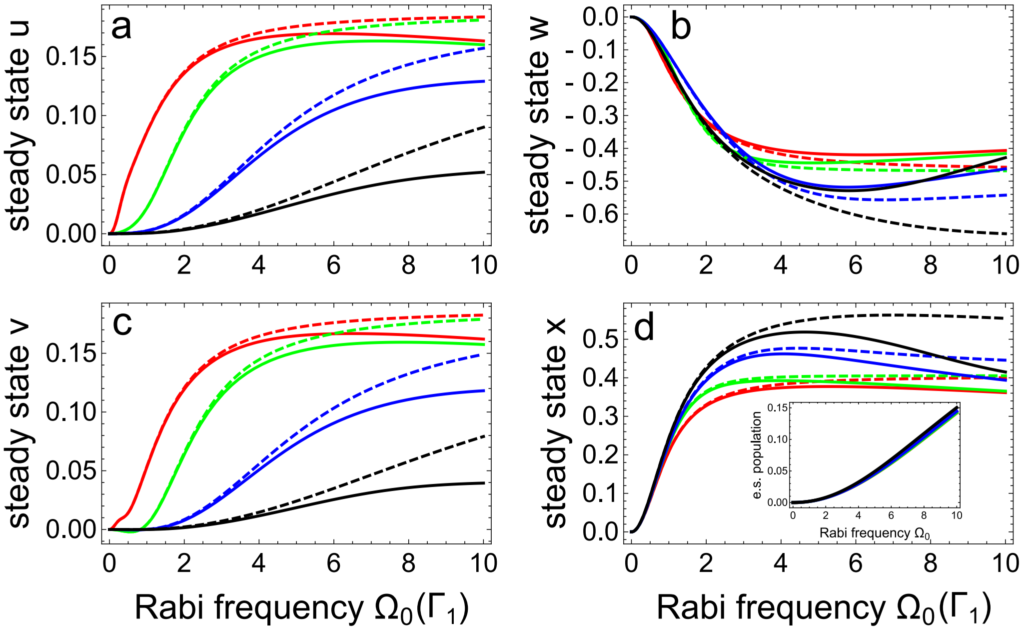

FIGURE 2.5: Steady state atomic variables: (a) real part of ground state coherence u, (b) orientation w, (c) imaginary part of ground state coherence v and (d) alignment x. Full: solutions of the full system of equations. Dashed: solutions of the approximate system of equations (2.15). Red: $\Omega_z = 10^{-4}\ \Gamma_1$ ($B_z = 0.4$ mG). Green: $\Omega_z = 0.01\ \Gamma_1$ ($B_z = 43.4$ mG). Blue: $\Omega_z = 0.1\ \Gamma_1$ ($B_z = 434$ mG). Black: $\Omega_z = 0.5\ \Gamma_1$ ($B_z = 2.17$ G). Inset: total excited state population. The x axis is the Rabi frequency Ω_0 related to the circular components of (2.7) as $\Omega_+ = \Omega_0/\sqrt{20}$, $\Omega_- = (1+i)\Omega_0/\sqrt{20}$, corresponding to beam intensity range $I = 0-1$ W/cm^2. The beam detuning is $\Delta = -7\ \Gamma_1$, the ground state decoherence and depopulation rates are $\gamma_1 = r = 10^{-3}\ \Gamma_1$.

Fig. 2.4 shows the influence of detuned linearly polarized light on the atoms. Two mechanisms govern the steady state solutions: the Raman process and optical pumping. For effectively zero B-field (red curves), the optical pumping is virtually non-existent, due to linear polarization of the beam, as is evident from the fact that $w = 0$ in this regime. The alignment x is however in this case not equal to 0, but saturates at $x \approx 0.3$. The driver of x is the parameter $\mathcal{S}$. For small longitudinal B-field the value of the imaginary part of coherence v is low, due to the input light being polarized linearly along the x-axis (see discussion in Subsection 2.2.1). Increasing the longitudinal B-field to positive values introduces optical pumping into $m = -1$ state due to Zeeman shift causing a stronger coupling of the σ^- light. The increase of $|w|$ however peaks at a certain value $\propto \Omega_z$ after which $|w|$ starts decreasing again. For higher B_z-fields the steady state values of u decrease and stronger w variable pumping occurs, indicating that a competition between the two variables may exist in this system. The peaks in v are caused by the coupling to w, which is positive since both couple more strongly to light not polarized along the x-axis. The x is driven positively by w, and features a “bump” corresponding to the w increase after which it saturates to a finite value with increasing Ω_0.

The elliptically polarized light case with $\Omega_+ = \Omega_0$, $\Omega_- = (1+i)\Omega_0$ is shown in Fig. 2.5. The most notable difference with respect to the previous Fig. 2.4 is the increase of the value of v variable. The rise in v is a consequence of the departure of light polarization away from x-axis, and for the same reason the u is decreased. Strong pumping of w now exists even for effectively zero B_z field because the intensity of the σ^- beam is twice that of the σ^+.

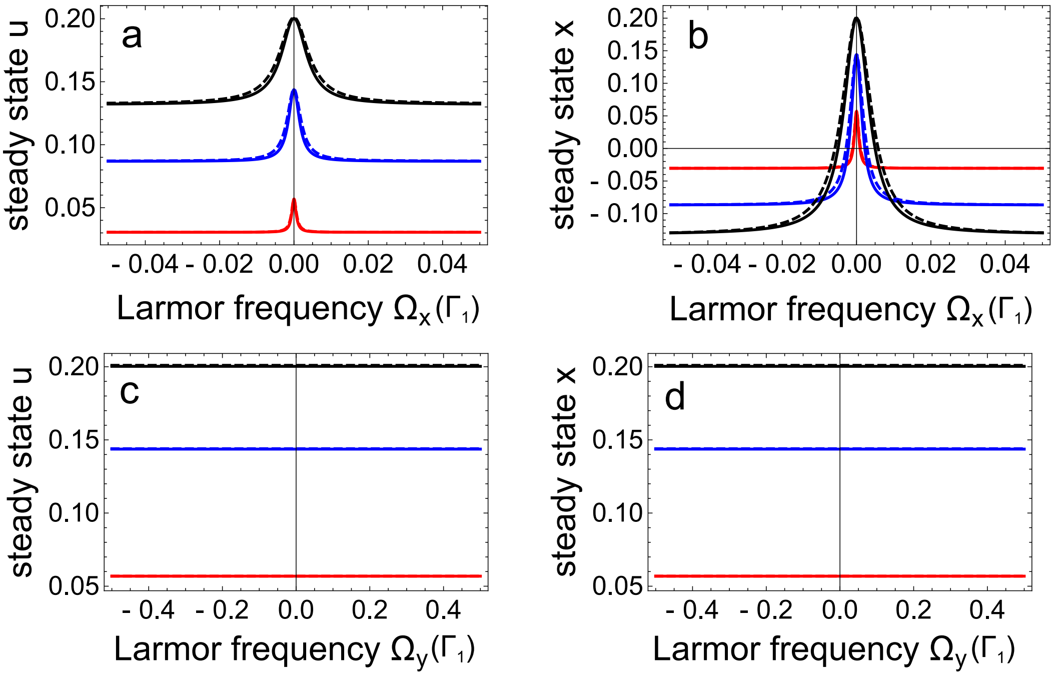

FIGURE 2.6: Steady state atomic variables: (a) real part of ground state coherence u, parallel Larmor frequency scan, (b) alignment x, parallel Larmor frequency scan, (c) real part of ground state coherence u, orthogonal Larmor frequency scan and (d) alignment x, orthogonal Larmor frequency scan. Full lines: solutions of the full system of equations. Dashed lines: solutions of the approximate system of equations (2.19). Red: $\Omega_0 = 0.5\ \Gamma_1$ ($I_+ = I_- = 0.84$ mW/cm^2). Blue: $\Omega_0 = 1\ \Gamma_1$ ($I_+ = I_- = 3.3$ mW/cm^2). Black: $\Omega_0 = 1.5\ \Gamma_1$ ($I_+ = I_- = 7.5$ mW/cm^2). The beam detuning is $\Delta = -7\ \Gamma_1$, ground state decoherence and depopulation rates are $\gamma_1 = r = 10^{-3}\ \Gamma_1$ and the Larmor frequencies of the fields not scanned are equal to zero. Imaginary part of ground state coherence v and orientation w are equal to zero for the given parameters.

2.3.2 Transverse B-fields

The dependence of atomic variables on the transverse fields is depicted in Fig. 2.6. The field parallel to input light polarization (B_x) causes a decay of the central feature in u and x, caused by population trapping in stretched states, whereas the orthogonal field (B_y) does not induce such a decay. The fact that the effect of the scan of the two B-fields are not equal was expected from inspection of the Hamiltonian (A.3). The v and w variables are zero for parameters of Fig. 2.6. The agreement between full theory and the reduced equations is again very good. To confirm the validity of Eqs. (2.19) under different conditions, the parallel and orthogonal B-field scans for linear light polarized along x-axis are shown in Figs. 2.7, 2.8. The agreement of approximate equations (dashed lines) with full theory

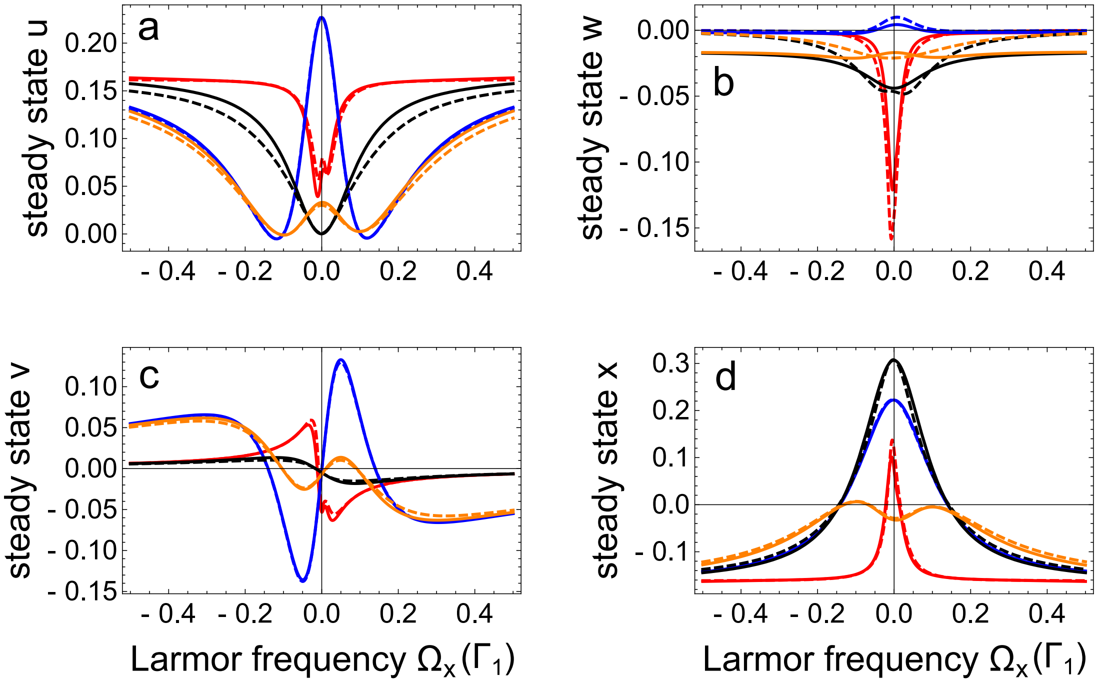

FIGURE 2.7: Steady state atomic variables: (a) real part of ground state coherence u, (b) orientation w, (c) imaginary part of ground state coherence v and (d) alignment x. Full lines: solutions of the full system of equations. Dashed lines: solutions of the approximate system of equations (2.19). Red: $\Omega_z = 0.01$, $\Omega_y = 0.01$ ($B_z = 43.4$mG, $B_y = 43.4$mG). Blue: $\Omega_z = 0.01\ \Gamma_1$, $\Omega_y = 0.1\ \Gamma_1$ ($B_z = 43.4$ mG, $B_y = 434$ mG). Black: $\Omega_z = 0.1\ \Gamma_1$, $\Omega_y = 0.01\ \Gamma_1$ ($B_z = 434$ mG, $B_y = 43.4$ mG). Orange: $\Omega_z = 0.1\ \Gamma_1$, $\Omega_y = 0.1\ \Gamma_1$ ($B_z = 434$ mG, $B_y = 434$ mG). The x axis is the parallel Larmor frequency Ω_x. The beam component intensities are $I_+ = I_- = 13.4$ mW/cm^2, detuning is $\Delta = -7\ \Gamma_1$, the ground state decoherence and depopulation rates are $\gamma_1 = r = 10^{-3}\ \Gamma_1$.

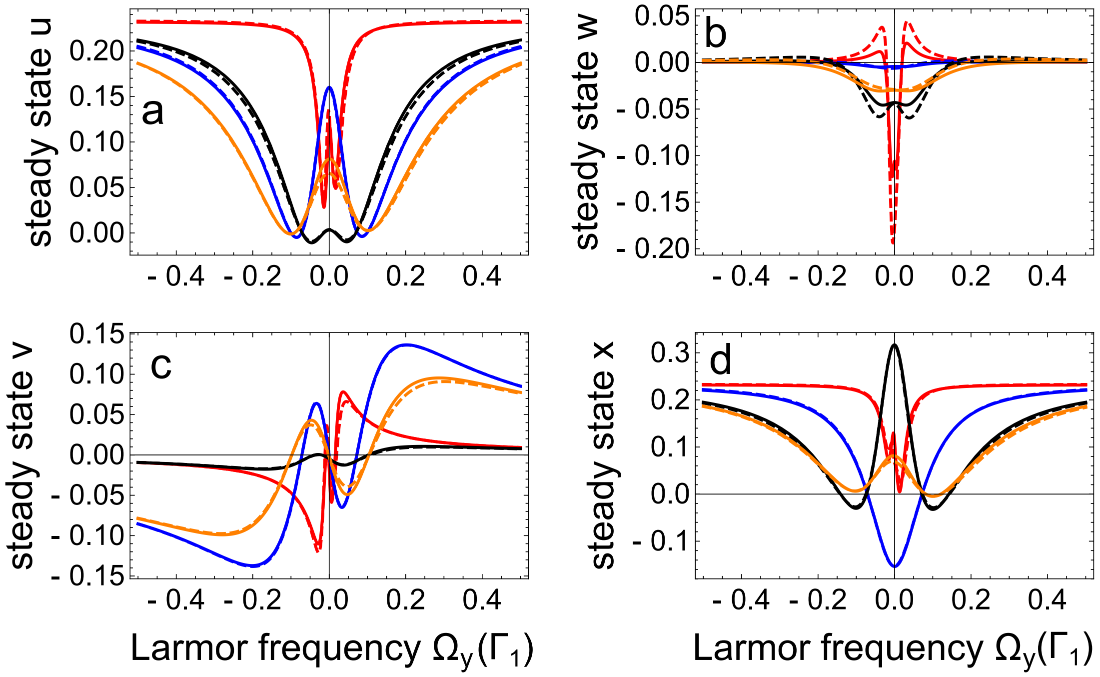

FIGURE 2.8: Steady state atomic variables: (a) real part of ground state coherence u, (b) orientation w, (c) imaginary part of ground state coherence v and (d) alignment x. Full lines: solutions of the full system of equations. Dashed lines: solutions of the approximate system of equations (2.19). Numerical and plot parameters are the same as in Fig. 2.7 with substitution $\Omega_x \to \Omega_y$.

(full lines) is again very good, especially for low B-fields and light intensities. The general consequence of both B_x and B_y fields is the decay of the central features of all the atomic variables. The presence of B-fields with all three components causes asymmetries and complicated features to arise, however a deeper investigation of these complicated features is beyond the scope of this Thesis.

2.3.3 Optical properties

Phase shift and absorption are calculated by inserting the expression (2.23) into the paraxial wave equation [54]. For purely circular input polarization, the optical properties of the medium are governed by the quantity $\alpha_\pm$, which depends on the atomic variables w and x as

$$\alpha_\pm = -\frac{b_0}{2L}\frac{i\Gamma_2 + (\Delta \mp \Omega_z)}{\Gamma_2^2 + (\Delta \mp \Omega_z)^2}\left(1 \pm \frac{3}{4}w + \frac{1}{20}x\right), \tag{2.26}$$

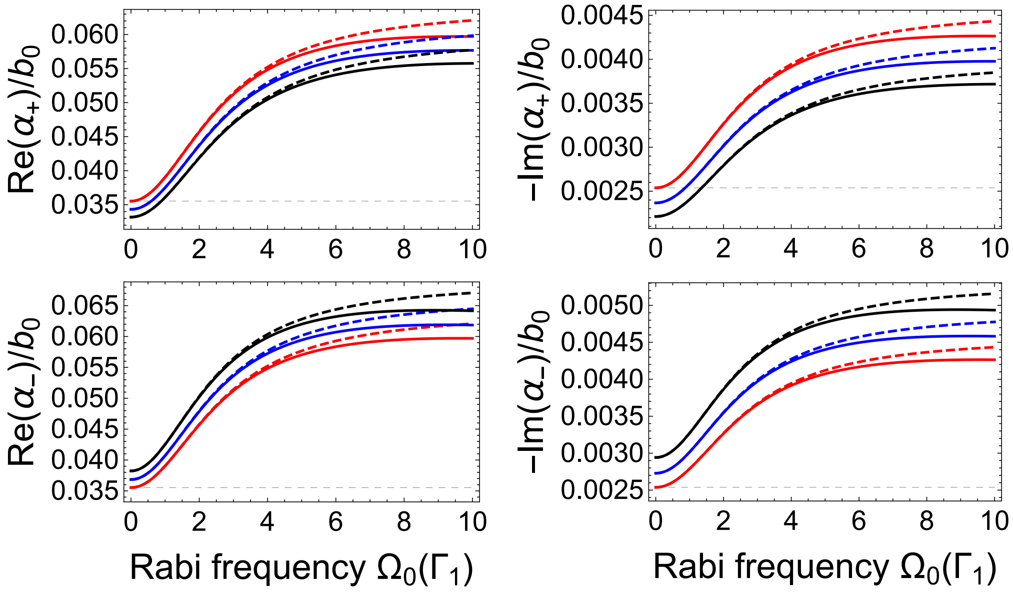

FIGURE 2.9: Real and imaginary parts of $-\alpha_{\pm}$L (2.26) for: (a) σ^+ transition, real part, (b) σ^+ transition, imaginary part, (c) σ^- transition, real part and (d) σ^- transition, imaginary part. Horizontal dashed line: linear susceptibility for $\Omega_z = 0$. Full lines: solutions of the full system of equations. Dashed lines: solutions of the approximate system of equations (2.15). Red: $\Omega_z = 10^{-4}$ Γ_1 ($B_z = 0.4$ mG). Blue: $\Omega_z = 0.25\ \Gamma_1$ ($B_z = 1.1$ G). Black: $\Omega_z = 0.5\ \Gamma_1$ ($B_z = 2.17$ G). The x axis is the Rabi frequency Ω_0 related to the circular components of (2.7) as $\Omega_+ = \Omega_0/\sqrt{20}$ (a and b) and $\Omega_- = \Omega_0/\sqrt{20}$ (c and d), corresponding to beam intensity range $I = 0 - 335$ mW/cm^2. The beam detuning is $\Delta = -7\ \Gamma_1$, ground state decoherence and depopulation rates are $\gamma_1 = r = 10^{-3}\ \Gamma_1$.

where b_0 is the on-resonance optical thickness and L is the length of the optical medium. The beam with electric field E_0 is then modified to $E_0 \exp(-i\alpha_{\pm}\mathrm{L})$ after traversing the atomic cloud. The factors $\Delta \mp \Omega_z$ describe the linear Faraday rotation, giving phase shifts of opposite signs for a same longitudinal B-field to the two circular components [77]. The factor "±" in front of the w variable also gives an opposite phase shift for same value of w. The term $\pm\frac{3}{4}w$ is the non-linear Faraday rotation, an effect generally more sensitive to the longitudinal B-field than linear Faraday rotation, for the optimal parameter values [78]. The effect is used for minimizing the stray B-fields in the experiment, as shown in Chapter 3. Fig. 2.9 shows the real and imaginary parts of the factors $-\alpha_{\pm}$L (normalized to b_0) for both circular polarizations, giving phase shift and absorption, respectively. The absorption is seen to increase by a factor $\sim 9/5$ for high beam intensities, a well known consequence of pumping into bright stretched states [22]. The phase shift ($\propto$ refractive index) also increases with intensity, which is due to the medium non-linearity being self-focusing. For the detuning of $|\Delta| = 7\ \Gamma_1$, the phase shift

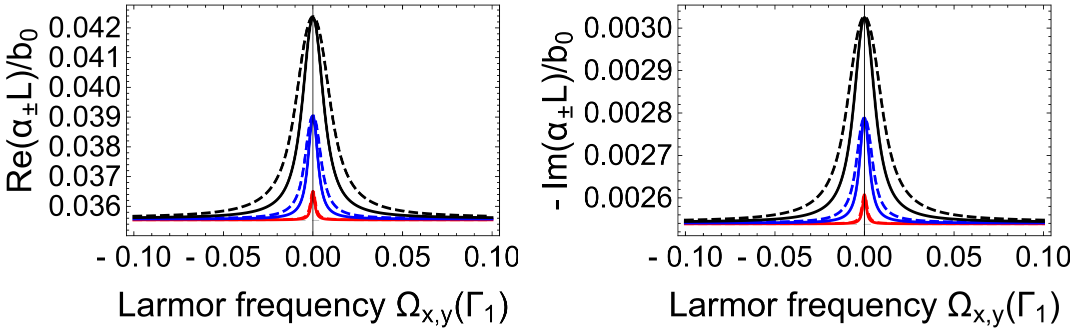

FIGURE 2.10: Real and imaginary parts of $-\alpha_{\pm}$L (2.26) for: (a) σ^+ transition, real part, (b) σ^+ transition, imaginary part, (c) σ^- transition, real part and (d) σ^- transition, imaginary part. Horizontal dashed line: linear susceptibility for $\Omega_z = 0$. Full lines: solutions of the full system of equations. Dashed lines: solutions of the approximate system of equations (2.15). Red: $\Omega_z = 10^{-4}$ Γ_1 ($B_z = 0.4$ mG). Blue: $\Omega_z = 0.25\ \Gamma_1$ ($B_z = 1.1$ G). Black: $\Omega_z = 0.5\ \Gamma_1$ ($B_z = 2.17$ G). The x axis is the Rabi frequency Ω_0 related to the circular components of (2.7) as $\Omega_+ = \Omega_0/\sqrt{20}$ (a and b) and $\Omega_- = \Omega_0/\sqrt{20}$ (c and d), corresponding to beam intensity range $I = 0 - 335$ mW/cm^2. The beam detuning is $\Delta = -7\ \Gamma_1$, ground state decoherence and depopulation rates are $\gamma_1 = r = 10^{-3}\ \Gamma_1$.

is enhanced by a factor of ~ 7 with respect to absorption, justifying the neglect of absorption in the qualitative treatment of pattern formation. The gray dashed lines are the linear phase shift and absorption for zero B-fields. Changing the longitudinal B-field to positive values illustrates the linear Faraday rotation, reducing the phase shift of σ^+ light and increasing it for σ^- light. Fig. 2.10 shows the effect of transverse fields on $-\alpha_{\pm}$L. The pumping effects decay to the linear value (gray line) with both the parallel (B_x) and orthogonal (B_y) fields, a consequence of destroying the optical pumping by transverse field Larmor precession.

Chapter 3

Experimental setup

In this Chapter the experimental setup used to study the formation of magnetization patterns in a cold atomic medium is described. The first part is devoted to the description of the setup and mechanism of magneto-optical trapping, used to prepare the optical medium for the pattern formation experiment. The second part deals with the details of the pattern formation experiment. Some relevant points regarding the study of magnetization patterns such as polarization sensitive near- and far-field imaging of the patterned light, monitoring of pump pulse intensity fluctuations and control of the external B-fields are described.

3.1 Preparation and characterization of the optical medium

In this Section the basics of preparation and characterization of the cold atomic medium used in the non-linear pattern formation experiments are outlined.

3.1.1 Laser cooling and trapping of neutral atoms

Using photon momentum to “push” matter is an idea dating back to the end of the 19th century with the development of classical electromagnetic theory by Maxwell

[79]. First experiments performed by Lebedev [80] and Nichols and Hull [81] measured the radiation pressure of incoherent light on small pieces of reflective metal, which was followed by R. Frisch's experiments with atoms [82]. After Ashkin's pioneering demonstration of atom trapping and acceleration by laser light [83], the conventional molasses cooling was devised by Hänsch and Schawlow [84]. In recognition of many useful and interesting subsequent developments in the field of laser cooling of thermal (non-degenerate) atoms the Nobel Prize in 1997 was awarded to S. Chu, W.D. Phillips and C. Cohen-Tannoudji for their work concerning magneto-optical trapping (MOT) and sub-Doppler cooling reported e.g. in Refs. [85, 86, 87, 88, 74].

The technique of MOT is in recent times often utilized in initial stages of producing bosonic [89, 90, 91, 92] and fermionic [93, 94, 95] quantum gases. Thermal cold atomic ensembles prepared by the technique of MOT however still constitute a platform for studying novel physics in state of the art experiments. Recent years have seen thermal cold atoms being used in a number of experiments studying collective and cooperative effects arising due to optical dipole-dipole interactions in ground level and Rydberg excited atoms [96, 97, 98, 99, 100]. Another use is found in the fields of quantum information and measurements, where e.g. quantum memories [101, 102], quantum repeaters [103], and spin squeezing [104, 105] were demonstrated in the free space configuration, and spin entanglement [106] and single photon switching [107] for thermal ensembles confined inside an optical cavity by a far detuned dipole beam. More closely related to the subject of this Thesis, the experiments performed in the group of D. Gauthier have studied pattern formation in elongated MOT clouds pumped by two counterpropagating beams [15, 16, 17]. Progress has also been made towards using MOT clouds in plasma and astrophysical simulations [108, 109]. In addition to these and many other examples, miniaturized MOT setups hold promise for increasing the sensitivities of magnetic and rotational sensors while optical clocks based on cold atoms could in the future be used for more precise navigation [110, 111].

3.1.2 Principle of magneto-optical trapping

The physics of magneto-optical trapping is explained in great detail in myriad research articles, review papers and textbooks [22, 112, 113, 114, 115]. Briefly, laser cooling is achieved through imparting the photon momentum to the atoms via their relatively narrow optical transitions. For producing localized clouds of atoms, typically six laser beams are used, counterpropagating along the three orthogonal space directions. To successfully cool the atoms, a laser frequency lower than the atomic transition frequency is needed. Along a single axis, the atoms moving towards one direction will then preferentially absorb photons coming towards it, and have a lower probability of absorbing the photons traveling in the same direction as the atoms, due to Doppler shift. This will produce a cloud with the slowest atoms localized at the intersection of the six cooling beams.

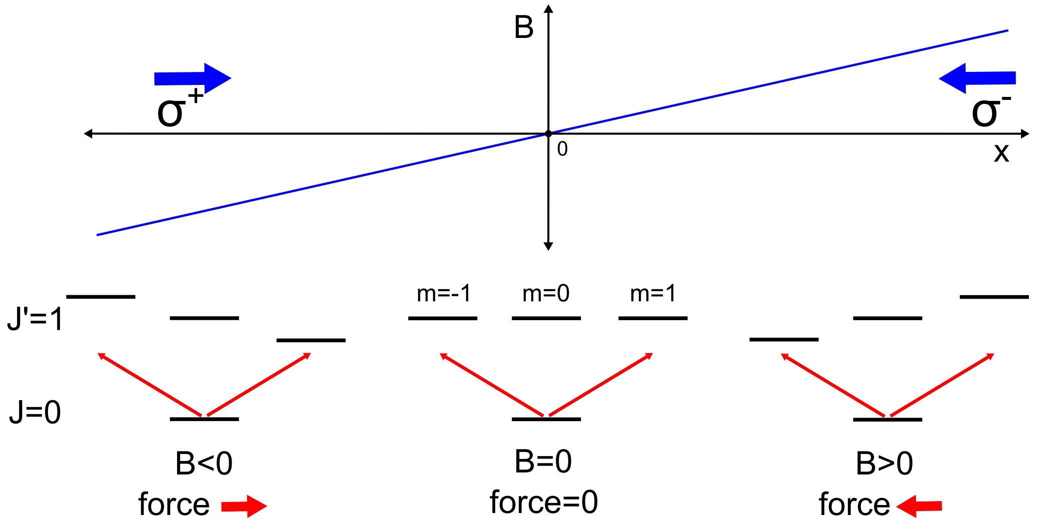

FIGURE 3.1: Principle of magneto-optical trapping in a simplified $J = 0 \rightarrow J' = 1$ system. The quadrupole coils provide the B-field gradient required to spatially engineer the absorption probabilities of right and left propagating beams.

Atoms can then be trapped by using a technique called magneto-optical trapping, outlined in Fig. 3.1. The technique is based on spatially engineering the absorption probabilities of photons coming from different directions via spatially varying

Zeeman shifts. For the two counterpropagating oppositely circularly polarized beams, the linear magnetic field gradient causes Zeeman shifts which bring the atoms in the positive (negative) part of the quantization axis closer to resonance with the σ^+ (σ^-) photons coming from the left (right), resulting in a restoring scattering force with a linear dependence on distance from cloud centre [22]. This force is of dissipative nature and the cooling temperature of the cloud is limited to the Doppler temperature $T_{Doppler} = \hbar\Gamma_1/2k_B$ [22], where Γ_1 is the excited state population decay rate, by random motion of the atoms after spontaneous photon emission. If the B-field gradient is sufficiently low, an effect known as Sisyphus cooling can take place to cool the atoms down to single photon recoil limit [86].

3.1.3 Laser system

The schematics of the hyperfine transitions of the ^{87}Rb D$_2$ line is depicted in Fig. 3.2a. Two diode lasers with emission wavelengths of $\lambda = 780$ nm are used in the experiment. The MOT laser is locked to the $F = 2 \rightarrow F' = 3$ transition and detuned by $\Delta = -2.8\ \Gamma_1$ with a pair of acousto-optical modulators (AOMs) to allow for efficient cooling and trapping. The beam used for pattern formation with single mirror feedback is derived from the same laser, but higher detuned (typically $\sim -7\ \Gamma_1$). The repumper laser is locked to a crossover $F = 1 \rightarrow F' = 0,\ 2$ transition and detuned by $\Delta = 114.6$ MHz into resonance with the $F = 1 \rightarrow F' = 2$ line. In general, a repumper laser is needed in laser cooling setups to repump the atoms into the bright (in this case $F = 2$) ground state due to the fact that there is a finite probability of atoms decaying into the dark (in this case $F = 1$) ground state. The repumper optically pumps the atoms back into the bright state by exciting the atoms into the excited state (in this case $F' = 2$) with a finite probability of decaying into the bright ground state.

The diodes have free running linewidths of ~ 10 MHz [116]. To efficiently cool the atoms close to the Doppler limit the frequency of the laser needs to be stable to temperature and mechanical fluctuations and the linewidth needs to be below the natural atomic linewidth Γ_1 of the cooling transition. In the case of the cooling transition used in this Thesis, this value is $2\pi \times 6.066$ MHz. This means some form of active stabilization of laser frequency is required to successfully perform the cooling of the atoms and pumping of the patterns.

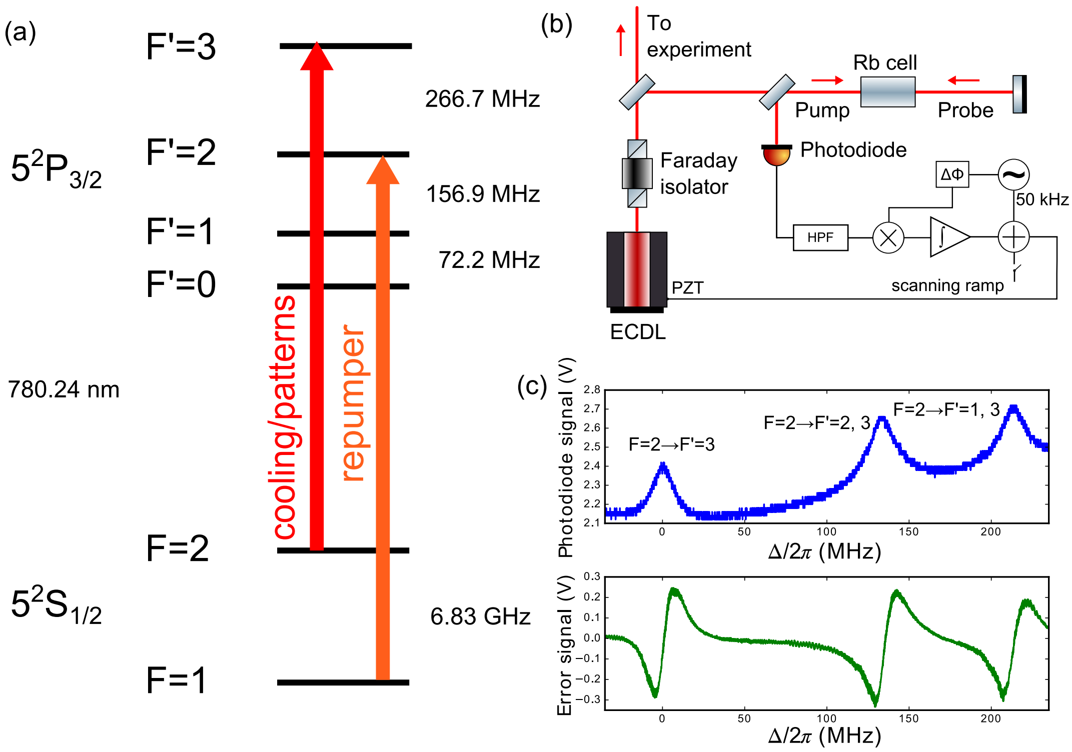

FIGURE 3.2: Details of the laser setup. (a) hyperfine levels of the D_2 line of ^{87}Rb with cooling/pump and repumper transitions indicated. (b) saturation spectroscopy setup and locking mechanism. HPF: high-pass filter, ×: demodulator, ΔΦ: phase shifter, ∼: 50 kHz modulation, $\int$: integrator, +: adder, PZT: piezoelectric transducer, ECDL: external cavity diode laser. (c) photodiode and error signal for scanning ramp applied to the PZT, linearly ramping the frequency of the laser.

The method commonly used for ^{87}Rb laser cooling applications is *saturation spectroscopy* [117]. It is based on pumping the atoms inside a room temperature vapor cell, with full width at half maximum (FWHM) Doppler broadening of ~ 0.5 GHz, and probing the saturated transitions. Due to the Doppler effect, the pump (frequency ω, wavevector $\mathbf{k}$) is resonant with atoms moving with velocity $\mathbf{v}$ satisfying the relation

$$\omega_{at} + \mathbf{k} \cdot \mathbf{v} = \omega \tag{3.1}$$

where ω_{at} is the frequency of the optical atomic transition. The same beam, when reflected (frequency ω, wavevector $-\mathbf{k}$), will be resonant with atoms moving with velocity $-\mathbf{v}$, satisfying the same relation, and out of resonance with all other atoms, including ones moving with $\mathbf{v}$. The signal for such frequencies ω results in the wide Doppler broadened ($\sim$ 500 MHz) absorption dips seen as the slowly varying background in the frequency peaks of Fig. 3.2c. The locking however relies on atoms moving at velocities $\mathbf{v} \approx 0$. Those atoms are pumped when laser is at frequency $\omega = \omega_{at}$. The pump beam has powers of $\sim 100\ \mu$W and waist of $w = 1$ mm, translating into relatively high intensities of $I = 26$ mW/cm^2. Such high intensities are needed because the pump beam has to deplete the ground state populations to reduce the absorption of the reflected probe by "bleaching" the atoms to the probe light. As seen in Fig. 3.2c, the reduced absorption results in photodiode signal peaks. In addition to peaks at $\omega = \omega_{at}$, additional, crossover peaks are present. Crossover peaks appear at frequencies for which $(\omega_{at}^{(1)} + \omega_{at}^{(2)})/2 = \omega$, where ω_{at}^1, ω_{at}^2 are frequencies of two atomic hyperfine levels. In this case the pump light is resonant with atoms moving at $\mathbf{v}$ and satisfying the relation $\omega_{at}^{(1)} + \mathbf{k} \cdot \mathbf{v} = \omega$, whereas the probe light is resonant with the same velocity class of atoms satisfying the relation $\omega_{at}^{(2)} - \mathbf{k} \cdot \mathbf{v} = \omega$.

The locking signal is given by the saturation spectroscopy peaks, and the locking itself is performed electronically by a lock-in amplifier and a servo loop sending feedback to the piezo-electric transducer (PZT) of the external cavity diode laser (ECDL). The ECDL consists of a 780 nm laser diode and a grating in Littrow configuration [118]. The zeroth order of the grating is sent to the experiment and the first order is reflected back to the laser diode, serving as laser feedback. For a constant diode current, the angle of the grating can be varied by a PZT to slowly scan the laser frequency for fine adjustments. To get an error signal, which is in this case proportional to the derivative of the saturation spectroscopy peaks, a fast modulation of $\nu_m = 50$ kHz is applied to the PZT. The modulation around frequency ν with amplitude $\Delta\nu$ results in a photodiode signal

$$V(\nu + \Delta\nu \sin(\nu_m)t) = V(\nu) + \Delta\nu \frac{\mathrm{d}V}{\mathrm{d}\nu} \sin(\nu_m t) + \frac{(\Delta\nu)^2}{2!} \frac{\mathrm{d}^2 V}{\mathrm{d}\nu^2} \sin^2(\nu_m t) + ... \quad (3.2)$$

Multiplying this voltage by $\sin(\nu_m)t$ gives terms oscillating at harmonics of ν_m, which is known as demodulation. The higher harmonics are subsequently filtered by an integrator serving as a low pass filter. Demodulating the terms oscillating at ν_m, one gets [116]

$$V(\nu + \Delta\nu \sin(\nu_m)t) \approx \left(V(\nu) + \Delta\nu \frac{\mathrm{d}V}{\mathrm{d}\nu} + \frac{\Delta\nu^3}{8}\frac{\mathrm{d}^3V}{\mathrm{d}\nu^3} + \frac{\Delta\nu^5}{192}\frac{\mathrm{d}^5V}{\mathrm{d}\nu^5} + ... \right) \sin(\nu_m t) \tag{3.3}$$

If $V(\nu)$ is a saturation spectroscopy peak, its shape is Lorentzian, meaning the i-th derivative terms decay as $\left(\frac{\Delta\nu}{\Gamma_1}\right)^i$ and for $\Delta\nu \ll \Gamma_1$ it is justified to neglect terms with higher order than $i = 1$. The resulting signal is then proportional to a derivative of the voltage $V(\nu)$ and can be used as an error signal for frequency locking. The schematics of the locking circuit is depicted in Fig. 3.2b and more details can be found e.g. in Ref. [119]. The error signal, which is an inverted derivative of the saturation spectroscopy peaks, is integrated and sent to the piezoelectric transducer. The main source of noise in the ECDL are the drifts in diode temperature and grating angle, both thermal effects with sub-Hertz bandwidth. The slope of the error signal, related to the height of the peaks, is crucial for stable locking and in general some effort is required to optimmize the circuit parameters, e.g. modulation amplitude and circuit gain. Using the described locking method both the cooling and repumper laser linewidths were reduced to FWHM of 1.2 MHz with the frequency locks lasting for several hours.

The laser diodes output a beam with a maximum power of 50 mW, a value that would reduce to ~ 20 mW after the beam passes through all optical elements: two AOMs and a single mode fiber. The number of atoms N in a magneto-optical trap scales as $N \sim V^{1/3}$ with trapping volume V [119], and cooling beam intensities higher than I_{sat} are needed to reach optimal N values. Increasing the cooling beam power is then a necessary step for producing a large and optically dense cloud of cold atoms. For this purpose a tapered amplifier (TA) diode, of model 0780-2000-DHP is used in the setup. The TA diode amplifies the seed beam with 22 mW power to the power of ~ 2 W at current $I = 3.6$ A. The available cooling beam power is then reduced to 360 mW after losses due to passing through an

AOM in the double-pass configuration and coupling to a single mode fiber. The measured intensity of each of the 2 inch diameter beams is ~6.5 I_{sat}, which is enough to saturate the number of atoms in a MOT.

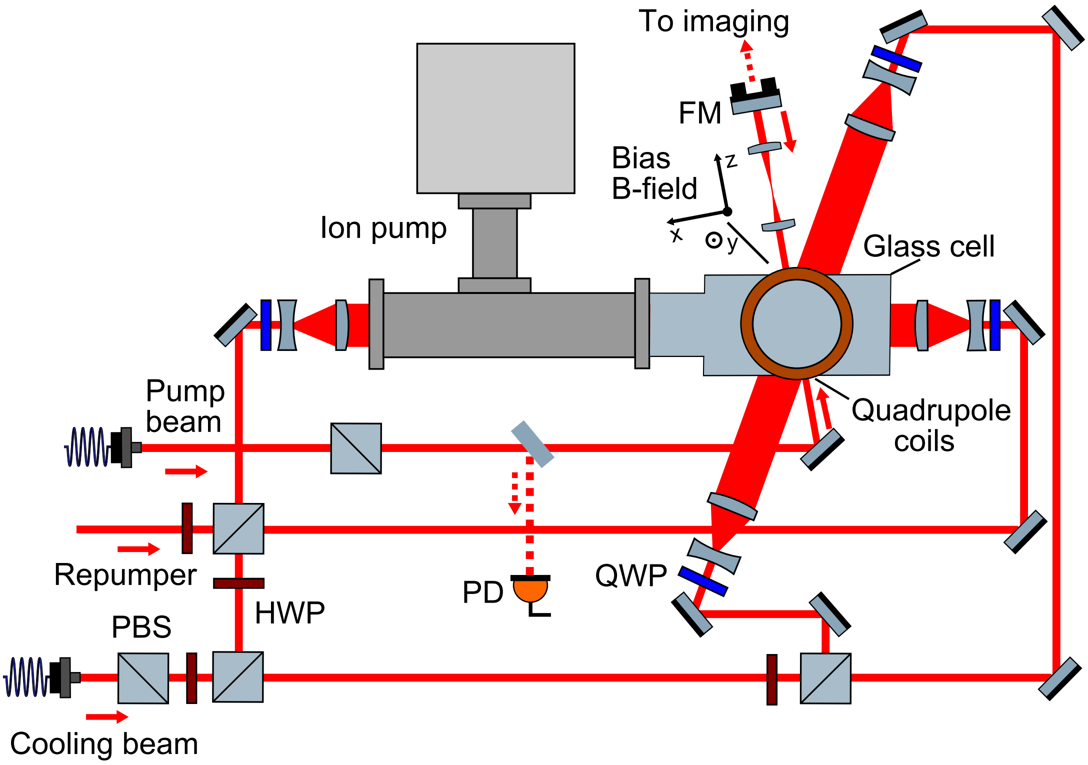

FIGURE 3.3: Schematics of the MOT and pattern formation setup. The 6 trapping beams overlap at the center of the coil pair in the anti-Hemholtz configuration, inside the glass cell. The repumper beam copropagates along one axis of the cooling beam setup. The linearly polarized pump beam is in the double pass configuration. The pump beam forms an 8°, and the cooling beam in the image plane a -17° angle with the cell normal. PBS: polarizing beam splitter. QWP/HWP: quarter/half wave plate. PD: photodiode. FM: feedback mirror.

3.1.4 Setup for laser cooling and trapping

The schematics of the MOT and pattern formation setup is shown in Fig. 3.3. To achieve spatial filtering the beam is coupled to a single mode fiber with a mode radius of 5 μm. After exiting the fiber the beam is collimated to a waist radius of ≈ 1 mm and passed through a PBS (polarizing beam splitter) to remove the influence of temperature induced polarization noise of the beam exiting the fiber on the intensity noise creating the intensity imbalance between the cooling beams. In this way shot-to-shot fluctuations in atom number are greatly reduced. The beam power after the first PBS is 360 mW. The beam is then split into 6 beams of equal power by an array of PBSs and half-wave plates (HWPs) which are transformed from linear to circular polarizations by quarter-wave plates (QWPs) prior to entering the cell. To increase the trapping volume, the beam waists are increased by pairs of divergent ($f = -16$ mm) and convergent ($f = 240$ mm) lenses to a diameter of 2 inches. In spite of the rather large beam diameters, the effective trapping volume is $1.5 \times 1.5 \times 1.5$ cm^3, limited by the small glass cell dimensions. The Rb atoms are then dispensed into the cell by running a current of $I_{getters} = 4.3$ A through the solid state getters.

The repumper is made to copropagate with the cooling beams by a PBS, splitting the power into two equal intensity parts, counterpropagating along one of the cooling axes indicated in Fig. 3.3. The power of the repumper beam is ≈ 15 mW, which is sufficient to provide pumping into the bright $F = 2$ state of the ^{87}Rb D$_2$-line [119].

The pump beam has a waist with $1/e^2$ radius of $w \approx 800$ μm and powers ranging from $0 - 1.5$ mW. This translates into intensities of $0 - 150$ mW/cm^2 by formula $I = \frac{2P_0}{w^2\pi}$. To ensure complete horizontal linear polarization, the pump beam is sent through a PBS. The beam intensity after the PBS is monitored by a calibrated photodiode (PD) outputting to a NI-6251 DAQ card. The beam is then sent to the cloud and reflected from a feedback mirror with reflectivity of $R = 0.95$. In between the feedback mirror and the glass cell, there is a pair of lenses with focal lengths of $f = 125$ mm in the $4f$ configuration. As explained in Ref. [120], in this setup the mirror is effectively imaged at a distance $d \lesseqgtr 0$ from the cloud center, given by the mirror distance from the focal point of the lens closest to it.

The cooling beam enters the cell at a -17° angle to normal. The chosen deviation from complete orthogonality of the cooling axes is a consequence of the rectangular shape of the cell, allowing only for highly non-normal incidence for the pattern pump beam if all cooling beams are orthogonal. Initial experiments were done with all cooling axes orthogonal and the pump at $\sim 50\ ^\circ$ angle to the normal. This caused astigmatism in the pattern wave vectors, causing the Talbot rings to deform into ellipsoids with stronger ellipticities for mirror distances close to the center of the cloud. To prevent this, a smaller pump beam angle to cell normal of 8° was used, therefore one of the cooling axes needed to be rotated. A non-zero pump beam angle was chosen due to high intensity of the pump beam (up to 100 mW/cm^2), causing $\sim$3.4% of the 780 nm light to reflect from each facet of the quartz glass cell [121], which can "seed" the patterns. This resulted in a complete pinning of hexagons at $B_z \neq 0$ and rhombs at $B_z \approx 0$, inhibiting the spontaneous rotational symmetry breaking inherent in the single-mirror setup and limiting the investigation of allowed symmetries in the four wave mixing case. The s and p reflection coefficients of quartz at 8° angle are $R_s = 0.035$ and $R_p = 0.033$ for vacuum to glass interface and $R_s = 0.036$ and $R_p = 0.032$ for glass to vacuum interface. For the σ^+ electric field component E_+, this will generate a small σ^- component when passing through the interfaces, with intensity $I_- = \left(\frac{t_s - t_p}{t_s + t_p}\right)^2 I_+$. Considering the transmission coefficients above are given for the electric fields, the generated σ^- intensity in vacuum to glass interface will be $I_- = 2.68 \times 10^{-7} \times I_+$, and $I_- = 1.07 \times 10^{-6} \times I_+$ in glass to vacuum interface. As discussed in Ch. 4, the slight polarization asymmetry is too small to cause a noticeable effect on diffracted powers in the two circular polarization channels.

3.1.5 Optical thickness optimization and measurements

The main property of the atomic cloud determining the threshold and contrast of the magnetization patterns studied in this thesis is the on-resonance optical thickness b_0. The optical thickness is limited by the atomic density which is in turn limited by multiple scattering of the photons inside the cloud [122]. The process of multiple scattering consists of one atom absorbing and spontaneously emitting a photon which is then absorbed by another atom in the cloud, causing a recoil away from the first atom. The force one atom exerts on the other can be calculated to decay with distance as $1/r^2$ [122], which saturates the density of atoms at cloud center. This can be mitigated by using the MOT compression technique [123], and ODs of ~ 100 can be reached in a non-elongated MOT cloud [98]. The basic idea of the technique is sketched in Fig. 3.4. Initially, a steady state MOT (sMOT) is loaded from vapor, with most of the atoms in the bright state $F = 2$. Reducing the repumper power, the atoms have higher probabilities of being in the dark $F = 1$ state after scattering the cooling photons. This reduces the multiple scattering and causes the cloud to compress, however the atoms in the cloud center are lost from the trap due to light assisted and hyperfine changing collisions [123]. To mitigate this, the MOT detuning is increased, causing the effective trap volume to increase which then traps more atoms to replenish the loss at cloud center. Experimental parameters of the cMOT stage are given in Sec. 3.2.1.

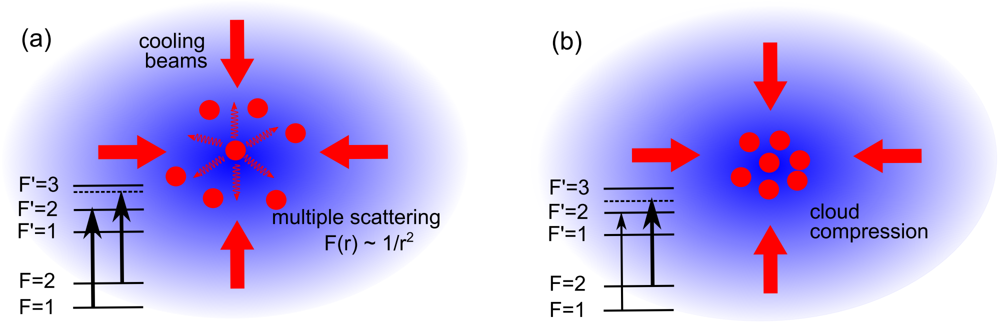

FIGURE 3.4: Schematics of the MOT compression technique. (a) In the steady state MOT (sMOT), the majority of the atoms are in the bright state. For a dense cloud, this means there is a high probability of multiple scattering of photons, causing an effective repulsive force between the atoms. (b) Reducing the repumper power, many atoms are pumped into the dark state after scattering the cooling photons, reducing the repulsive multiple scattering force.

The optical thickness and atom number in a MOT is routinely measured via absorption imaging, where a weak probe beam irradiates the cloud and creates a shadow image of it on a CCD [89]. Direct measurement of on-resonance optical thickness b_0 in samples with $b_0 \geq 5$ is difficult due to the finite spectral width of the probe laser and finite signal to noise, so measurement is done by fitting a Lorentzian to measurements of off-resonance optical thickness b_Δ at different detunings Δ [124]. Detuned transmission coefficient $T_\Delta(x,y)$ at a pixel with center located at point (x,y) (where x and y in this and the next Section mark the horizontal and vertical axes of the imaging plane) is given by Beer's law

$$T_\Delta(x,y) = \frac{I(x,y)}{I_0} = \exp\left(-b_\Delta(x,y)\right), \tag{3.4}$$

where $I(x,z)$: beam intensity after the cloud, I_0 : input probe beam intensity, $b_\Delta(x,y)$: off-resonance optical thickness at point (x,y) and detuning Δ. In experiments, the optical thickness varies over the area of the cloud due to its Gaussian shape. To get the b_0 one then averages the transmission $T_\Delta(x,y)$ over the experimental region of interest, which is determined by the pattern pump beam waist with radius of $w \approx 800\ \mu$m. Off-resonance optical thickness depends on the detuning Δ as a Lorentzian

$$b_\Delta = \frac{b_0}{1+\left(\frac{\Delta}{\Gamma_2}\right)^2}. \tag{3.5}$$

The optical thickness b_0 is proportional to the integral of the atomic density distribution $n(x,y,z)$ along line of sight [124]

$$b_0 = \sigma_0 \int n(x=0,\ y=0,\ z)\mathrm{d}z, \tag{3.6}$$

where σ_0 is on-resonance scattering cross section. Assuming a Gaussian density distribution with variances $\sigma_x,\ \sigma_y,\ \sigma_z$, the number of atoms can be calculated from peak density n_0 as $N = (2\pi)^{3/2}\sigma_x\sigma_y\sigma_z n_0$. The on-resonance optical thickness b_0 can then be related to number of atoms as

$$N = \frac{2\pi\sigma_x\sigma_y b_0}{\sigma_0}. \tag{3.7}$$

Assuming the cloud has the same dimension along x and z axes, $\sigma_x = \sigma_z$, the peak atomic density can also be calculated from

$$n_0 = \frac{b_0}{\sqrt{2\pi}\sigma_0\sigma_x} \tag{3.8}$$

Fig. 3.5a shows the optical thickness measurements of the MOT. The measurements were performed by shining a weak $P = 7$ μW probe beam pulse for $t = 250$ μs and integrating for $\tau = 300$ μs by a CCD. The cMOT properties after a waiting time of $\Delta t = 0.5$ ms are: $N = 9 \times 10^8$, $b_0 = 31.6$, $n_0 = 1.8 \times 10^{11}$ cm^{-3}. In Figs. 3.5b and 3.5c it is seen how both the peak density n_0 and the optical thickness decay due to cloud expansion, leaving $b_0 = 27.4$ at the time of flight point $\Delta t = 3.5$ ms after turning off the gradient coil.

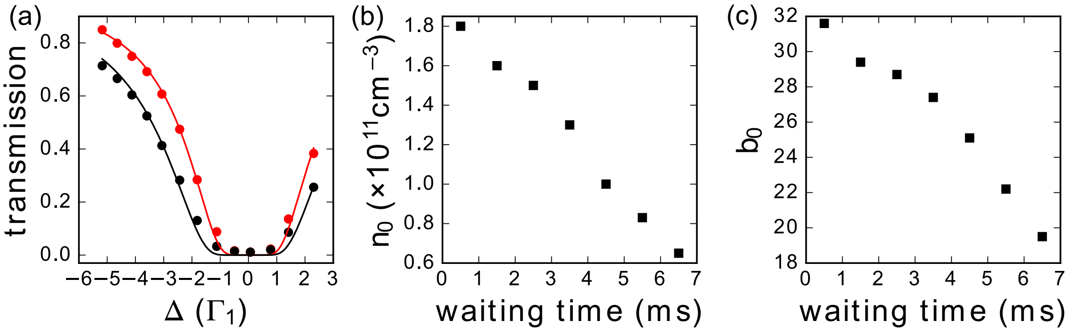

FIGURE 3.5: Properties of the compressed MOT (cMOT). (a) comparison of transmission of the MOT (red) and cMOT (black) clouds. The MOT cloud has an on-resonance optical thickness $b_0 = 19.4$ and the cMOT cloud has $b_0 = 31.6$. The decay of (b) peak atom density and (c) on-resonance optical thickness for a cMOT upon a time-of-flight interval after the gradient field is switched off.

3.1.6 Temperature measurements

Time of flight (TOF) technique is a widely used method for measuring the temperature of a thermal cold atom cloud [86]. It is based on measuring the rate of cloud expansion and fitting it to temperature using the equipartition theorem to relate the cloud kinetic energy with the temperature associated with its motion. Temperatures related to cloud expansion in x and y directions, $T_{x,y}$, are then calculated via

$$\sigma_{x,y}(\Delta t) = \sqrt{\sigma_{x,y}^2(0) + \frac{k_B T_{x,y}}{m} \Delta t^2}. \tag{3.9}$$

In Fig. 3.6 a TOF measurement of the atomic cloud expansion after the cMOT stage is presented. The 1D profiles in x and y direction are calculated by binning the near field images, resulting in smoothed out curves. The Gaussian shape of the fluorescence is a consequence of detuning the beam to $-2.8\ \Gamma_1$ and a waiting time of 6 ms after the release of the cloud.

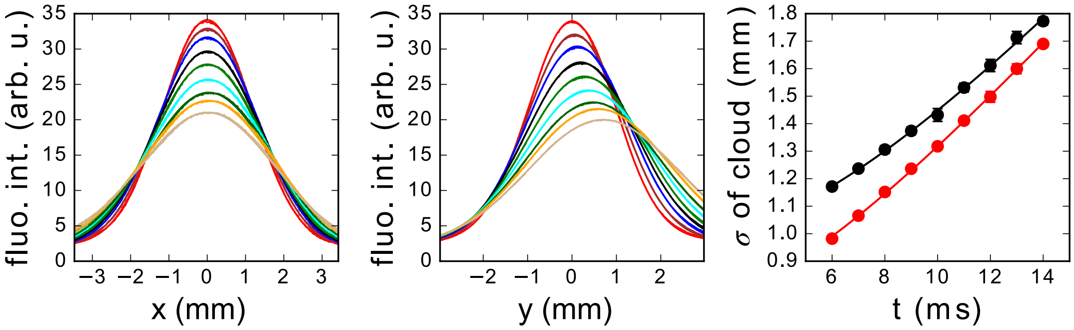

Figure 3.6: Time of flight measurement of cMOT cloud temperature. The images are averaged over ten realizations and the horizontal (x) and vertical (y) profiles are calculated by binning the 2D fluorescence image. The binned fluorescence signal with a Gaussian fit are shown in the first two plots from the left. Third plot shows the evolution of σ radii of the 1D Gaussian fits and a temperature fit calculated via the equipartition theorem. Black: σ_x radius (circles) and a temperature fit (line) yielding $T_x = 118\ \mu K$, red: σ_y radius (circles) and a temperature fit (line) yielding $T_y = 123\ \mu K$. The drift of the center of the Gaussian in the middle picture is due to gravity, and the center moves in positive direction due to the image inversion by the imaging telescope.

The temperatures are calculated from the fit to be $T_x = 118\ \mu$K and $T_y = 123\ \mu$K, giving a mean temperature of $\langle T \rangle = 120.5\ \mu$K. The mean temperature is lower than the Doppler limit for the ^{87}Rb D$_2$ line, $T_D = 146\ \mu$K. The reason for this is the cMOT stage, where the cloud radius is lowered ($\sigma_x \approx 1$ mm, $\sigma_y \approx 0.7$ mm), and the cooling beam detuned to $-6\ \Gamma_1$. This allows for a significant fraction of the atoms to be cooled below the Doppler limit [86]. The images of the cloud compression are shown in Fig. 3.7.

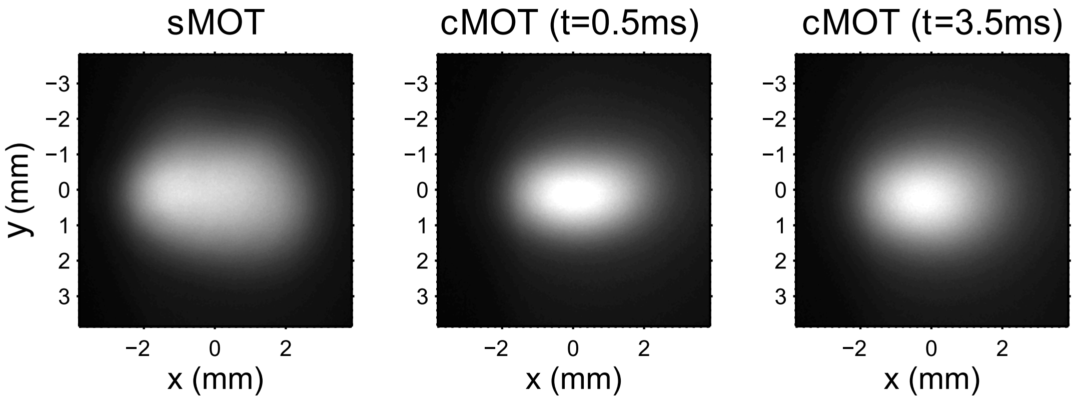

FIGURE 3.7: Fluorescence images of the MOT cloud at various stages. The steady state MOT (sMOT) is compressed in two stages: 15 ms of MOT detuning ramp ($\delta = -2.8\ \Gamma_1 \rightarrow \Delta = -6\ \Gamma_1$) and 15 ms of reduced repumper power ($P = 14.5\text{mW} \rightarrow P = 5\text{mW}$). The compressed MOT (cMOT) images are taken at 0.5 and 3.5 ms after turning off the cooling beam and B-field gradient, and the size of the MOT is seen to increase during the time of flight of 3 ms, decreasing the effective atomic density and consequently the optical thickness.

3.2 Pattern measurements

In this Section the methods and procedures of the pattern formation experiment are outlined. The first Subsection 3.2.1 describes the experimental sequence of the optical medium preparation and pattern formation. The succeeding Sections deal with near- and far-field imaging techniques used for monitoring the patterns and their properties, monitoring the fluctuations of pattern pump beam intensity and the B-fields inside the cloud. This provides an introduction to the next Chapter in which results of the experimental measurements of the magnetization patterns are described.

3.2.1 Experimental sequence

A typical experimental sequence is comprised of three stages: MOT loading, MOT compression and pattern formation measurement. The atoms loaded into a MOT are compressed by pumping into dark states (as described in Sec. 3.1.5) to increase the OD of the medium. After 3.5 ms of time-of-flight waiting time after the MOT beam and the quadrupole coils are switched off, required for the B-field to relax to the set value (see Sec. 3.2.4), the pump beam is turned on and pattern formation stage begins. Depending on the beam intensity, the patterns reach optimum contrast, i.e. steady state, at pump time of $t_p \approx 200$ μs. The patterns are then imaged in a polarization sensitive way for $5 - 60$ μs, depending on the desired signal range and whether the imaging is done in the near or far field. After the imaging stage, MOT loading stage begins again and the experimental sequence restarts.

The experiment is controlled by outputting voltages via two National Instruments Data acquisition (NI-DAQ) card models NI-6713 and NI-6251. To interface with the NI-DAQ cards a MATLAB code written by Nicolas Mercadier at INLN was used. The experimental sequence, along with the parameters used, is outlined in Fig. 3.8.

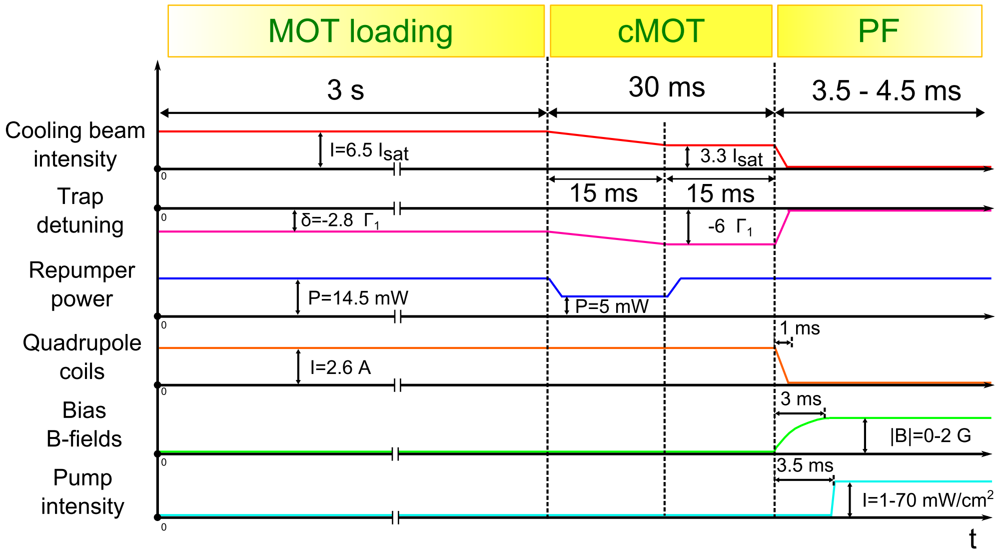

FIGURE 3.8: Typical experimental sequence of pattern formation measurements. A 3 s trap loading stage is followed by a 30 ms compression stage to reach higher optical thickness, after which the cooling beams and the gradient B-field is switched off. After a 3.5 ms of B-field relaxation time, the prepared optical medium is irradiated by the pump beam and patterns are imaged on the charge-coupled devices.

During the MOT stage, each of the six cooling beams have an intensity of $I = 6.5$ I_{sat} and detuning of $\Delta = -2.8$ Γ_1. The repumper beam with power of 14.5 mW copropagates with the two MOT beams along one of the axes. After the 3 s MOT stage, a 30 ms cMOT stage ensues, where the repumper beam is reduced to approximately a third of its initial value to enable the pumping of atoms into the dark $F = 1$ ground state, and the MOT beam is detuned to increase the effective trapping volume and replenish the lost atoms. The repumper beam power and cooling beam detuning in the first part of the cMOT stage are 5 mW and $-6\ \Gamma_1$, respectively. Due to the low AOM efficiency at high detunings, the cooling beam intensity also drops to $\approx 3.3\ I_{sat}$. In the second part of the cMOT stage, the repumper intensity is ramped back to its original value, to prevent the loss of atoms. After a cloud with an optimal OD of $b_0 \approx 30$ is prepared, the MOT beam and quadrupole coils are turned off. A constant external B-field of up to 2 G is then turned on to facilitate the study of the magnetization patterns. After a 3.5 ms B-field relaxation period, a cloud with an OD of $b_0 \approx 25$ is prepared for pattern formation experiments. The pump beam is then turned on and patterns are observed. After acquiring the pattern images, the sequence repeats for up to 500 iterations, depending on the number of scanned parameters and averages.

3.2.2 Near and far field imaging

Just as the pattern formation itself, the observation of patterns is based on Talbot effect. The magnetization patterns, resulting in phase modulation (neglecting here the amplitude modulations due to “thick medium” effects [125]) at the end of the cloud, produce a fully amplitude modulated image in a plane $z_T/4$ from the end of the cloud, where z_T is the Talbot length defined in Ref. [52] as the distance after which a phase/amplitude grating reproduces itself due to diffraction. The intensity modulated image transmitted through a $R = 95\%$ mirror and imaged on a CCD is equivalent to the feedback intensity modulation the cloud receives. This means the near field images correspond to images of phase modulation of the beam at the end of cloud, which are in turn a consequence of the distribution of population in Zeeman sublevels. Information about the magnetization profile is obtained by imaging the two linear or circular photon polarizations simultaneously by using either a half- (HWP) or quarter-wave plate (QWP), respectively, and spatially separating the two components with a polarizing beam-splitter (PBS). For simultaneous near- (NF) and far-field (FF) imaging this requires using four charge-coupled devices (CCD) triggered by the same source.

The CCDs used in the experiments are PointGrey Chameleon cameras with a USB interface and 8- or 16-bit pixel depth. The triggering is done by sending four pulses of 5 V from the DAQ card breakout box to the triggering pins of GPIO connectors. The images are then sent to the computer via USB interface and saved by the PointGrey FlyCap software.

Schematics of the NF imaging setup is depicted in Fig. 3.9a. The intensity modulated image of the beam phase after the cloud (C) is transmitted through the virtual mirror (M) with reflectivity of $R = 95\%$. After that a telescope is placed, with lenses L1 (focal length $f_1 = 50$ mm) and L2 ($f_2 = 125$ mm) in telescope configuration with total magnification of $M = 2.5$. In between the two NF imaging lenses, due to spatial constraints, a Newport model 10B20NP.27 50:50 non-polarizing beam splitter is placed (not shown) to split the beam for simultaneous FF imaging. The beam splitter is specified to have s- and p-polarization components matched to within 5 %, which is accounted for when taking quantitative data, as explained in the description of FF imaging. The linear/circular polarization components are then spatially separated by a HWP/QWP and a PBS and imaged onto two CCD cameras. The exposure time of NF imaging ranges from 20-60 μs with gain ranging from $G =$ 0-20.

Fig. 3.9b shows an example of NF imaging of σ^+ light for a hexagonal pattern (HX$^+$) with long range order. No noise subtraction has been performed on the image and the image has been rotated to make the peak rows parallel to the plot axes. Cross sections through the center of the image along dashed lines in 3.9b are shown in Figs. 3.9c and 3.9d. Long range order of patterns is confirmed by cross section scans. The y cross section is along the direction orthogonal to $\mathbf{q}_i$, and the spatial period of the peaks is half the spatial period of the x cross section. The intensity of the image ranges from 3-72 in arbitrary units.

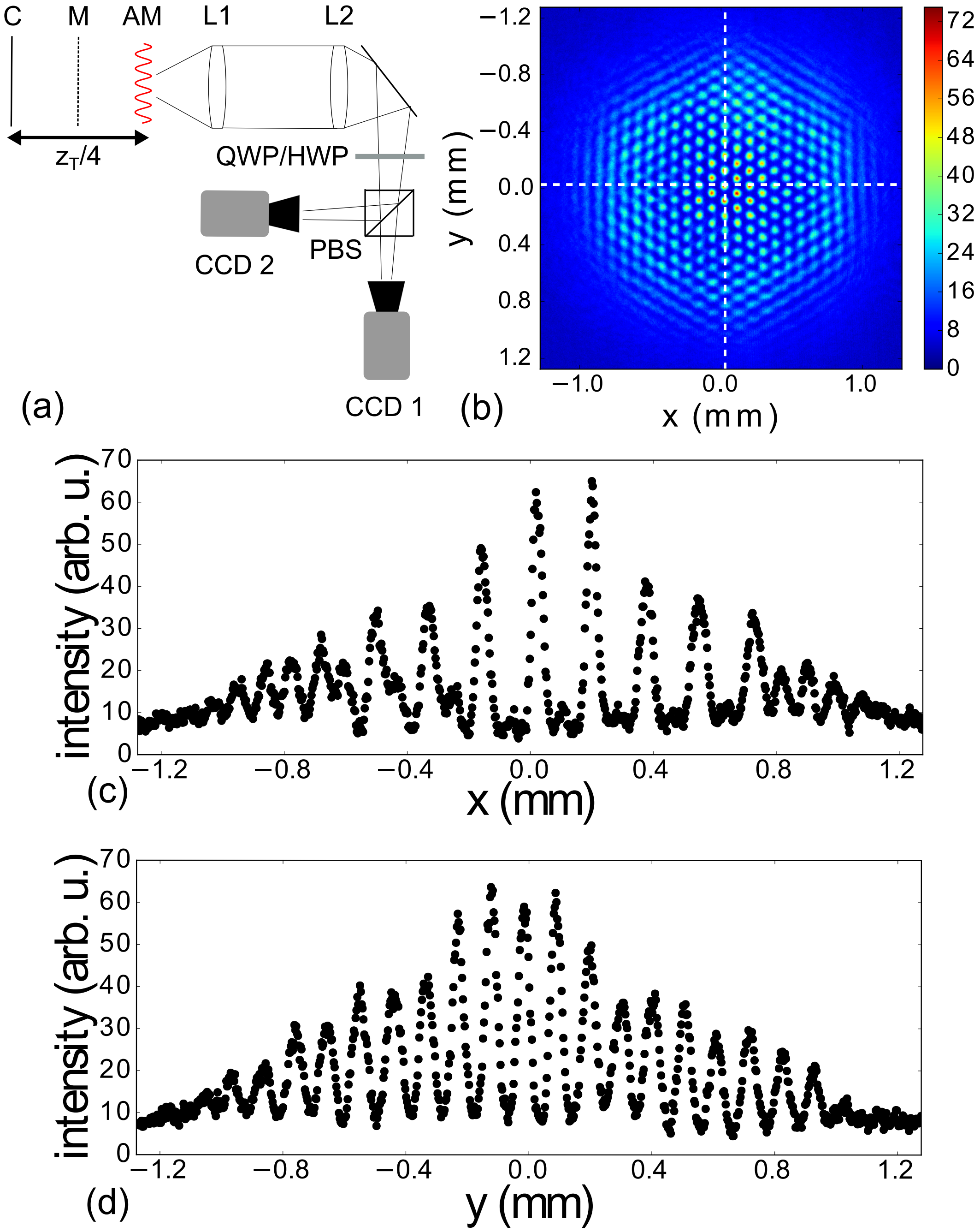

FIGURE 3.9: Schematics (not to scale) and example of near field imaging. (a) Schematics of near field, polarization selective imaging of the patterns. C: end of atomic cloud, M: virtual mirror, AM: amplitude modulation, L1: lens 1, $f_1 = 50$ mm, L2: lens 2, $f_2 = 125$ mm, QWP/HWP: quarter and half-wave plates, PBS: polarizing beam splitter, CCD: charge-coupled device. (b) example near field image, (c) scan through the horizontal line indicated in (b), (d) scan through vertical line indicated in (b).

Near-field imaging is used only for observation of pattern symmetries, and quantitative data such as diffracted power is extracted via far-field images.

Pure electric field Fourier transforms, i.e. FF images, provides a more accurate representation of the spatial spectrum than numerical Fourier transforms of NF images. This is because the NF images are an intensity profile, given by Eq.

$$I(x,y) = |\mathbf{E}(\mathbf{r})|^2 = |\mathbf{E}_0(1 + \Delta n(\cos(\mathbf{q}_1 \cdot \mathbf{r}) + \cos(\mathbf{q}_2 \cdot \mathbf{r}) + \cos(\mathbf{q}_3 \cdot \mathbf{r})) + ...)|^2 \quad (3.10)$$

where $\mathbf{E}_0$ is the electric field amplitude at the end of the medium, Δn is the refractive index modulation and the ellipsis denotes the h.o.t. in Δn and consequently in $\mathbf{q}_i$. Keeping only the first order terms, the numerically calculated Fourier spectrum will already have both pure $(\exp(2i\mathbf{q}_i \cdot \mathbf{r}))$ and mixed $(\exp(i(\mathbf{q}_i + \mathbf{q}_j) \cdot \mathbf{r}))$ second order terms (harmonics). This is a misrepresentation of the Fourier spectrum both in peak position and total diffraction intensity.

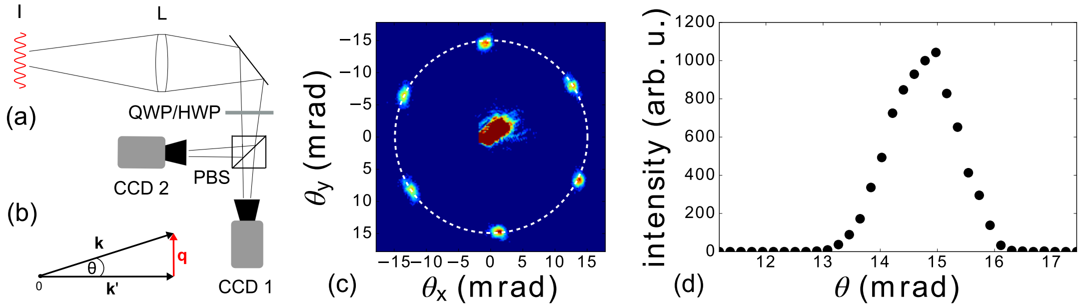

FIGURE 3.10: Schematics (not to scale) and example of far field imaging. (a) Schematics of polarization selective FF imaging. I - NF image plane, L - lens, $f = 50$ mm, QWP/HWP - quarter and half-wave plates, PBS - polarizing beam splitter, CCD - charge-coupled device. (b) definition of angle θ, wavevectors: $\mathbf{k}$ - beam exiting the atomic medium, $\mathbf{k}'$ - input light, $\mathbf{q}$ - transverse wave vector. (c) example FF image, (d) example azimuthal integration of 10 images for same parameters.

The schematics of FF imaging setup and an example result for a hexagonal pattern is depicted in Fig. 3.10. The schematics shows an imaging lens L (with focal length $f = 50$ mm) with its focus placed in the NF imaging plane. The FF images of the two polarization components are then projected on the CCD in the same way as in the NF case. Fig. 3.10b defines the angle θ between the input beam propagation direction $\mathbf{k}'$ and the beam direction after the cloud $\mathbf{k} = \mathbf{k}' + \mathbf{q}$. A horizontal distance x' in the CCD image is converted to an angle $\theta_{x'}$ via the relation $\theta_{x'} = \frac{x'}{f}$. The angles in the horizontal and vertical directions θ_x, θ_y are related to the cone angle θ via $\theta = \sqrt{\theta_x^2 + \theta_y^2}$. The pattern periodicity Λ is then calculated from the conical θ, determining the radius of the Talbot ring, and the relation $\theta = \lambda/\Lambda$. Figs. 3.10c and 3.10d shows an example of a FF image for a hexagnoal pattern. The CCD exposition time is $\tau = 40$ μs and background noise with pixel height ≤ 2 is subtracted. Longer sampling time serves to increase the signal to noise ratio by factor of $\sqrt{\tau}$ [126]. Subtracting the background is important in order to remove the linear increase of intensity with r in the radial profile, an artifact due to azimuthal integration of random noise. The diffracted power is then calculated by integrating under the peak in the radial profile.

The following procedure was used to account for birefringence imperfections of the non-polarizing and polarizing beam splitters. A HWP was put into the setup in front of a PBS (depicted in Fig. 3.10). An angle of the HWP for which the beam is horizontally linearly polarized was determined by finding the orientation at 45° angle from the two HWP angles that minimize the transmission. After this, a QWP was put into the setup, and incrementally varied. For each QWP angle, two sets of data were taken, one with light polarized horizontally and the other with the light polarized vertically to the table. The QWP angle which splits the light into circularly polarized components was then determined as the one for which the powers in the reflecting and transmitting PBS channels exchange place after rotation of the input polarization from horizontal to vertical. For horizontal light, one of the PBS channels (subsequently determined to be σ^-) has 45% and the other (σ^+) has 55% of the total beam power. To account for this asymmetry, the power in the σ^- channel was multiplied by 1.1, and the power in the σ^+ channel was multiplied by 0.9.

3.2.3 Monitoring pump intensity

Due to the fact that pattern formation is based on optical non-linearity of the system, fluctuations in the input light intensity will introduce significant noise in measured signal, i.e. diffracted power. As shown in Fig. 4.6, the total diffracted power varies linearly with input intensity, with a discontinuity at threshold for $B_z \neq 0$.

In the setup, the pump beam is derived from the cooling beam, which passes through a tapered amplifier (TA). After the TA, the beam passes through an AOM in double pass configuration, and the first diffracted order is coupled to a Thorlabs single-mode optical fiber with a 5 μm mode radius. The AOM and TA introduce a pointing instability in the mode profile of the beam, causing intensity fluctuations of the pattern pump beam exiting the fiber. The time scale of the fluctuations is thermal ($\nu_{fluct} \sim 1$ Hz) whereas the pump time of the pattern formation and imaging is $\Delta t_{pump} \sim 300$ μs, meaning the main contribution to the noise is due to shot-to-shot fluctuations, as the duration of MOT loading stage is $\Delta t_{MOT} = 3$ s.

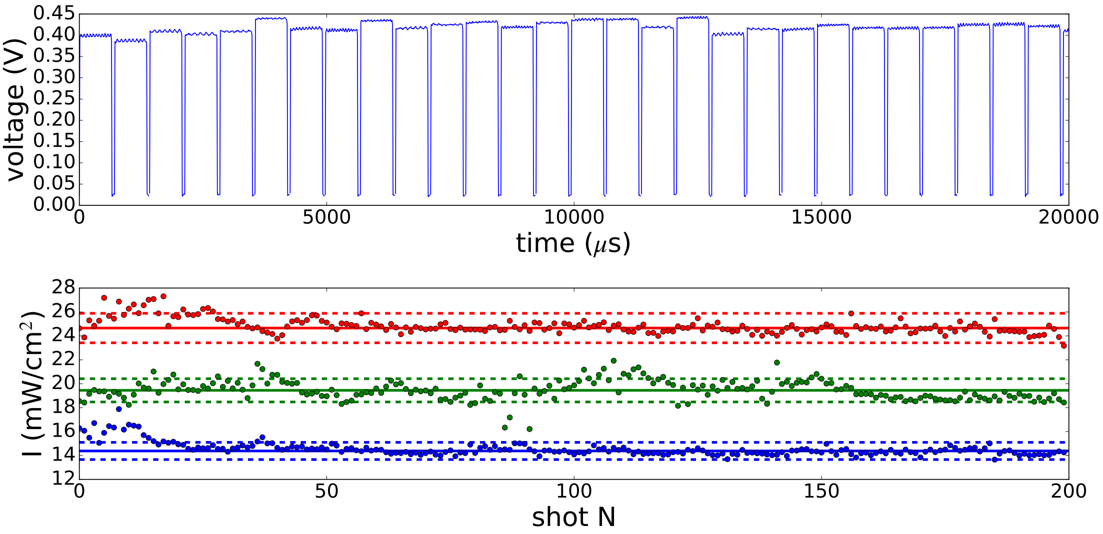

FIGURE 3.11: Monitoring shot-to-shot intensity fluctuations of the pump beam. (a) photodiode signal read by the analog input of the NI-DAQ device, (b) average intensities per shot for a sequence of $N = 200$ shots. Solid lines: average intensities $I = 14$ mW/cm^2 (blue), $I = 19$ mW/cm^2 (green), $I = 24$ mW/cm^2 (red), dashed lines: cut-off intensities for a tolerance of 5 %.

The input beam intensity is measured by a photodiode, with calibration $I = ((\langle V\rangle - 0.026 \times V) \times \frac{63.4}{V} + 0.98)$ mW/cm^2, and read by an analog input of the NI-DAQ 6713 device. For each experimental realization a set of 65 samples with duration 10 μs is taken and then averaged over a section of 550 μs duration. The effective integration time of 550 μs is longer than beam pumping time due to limitation caused by bandwidth of the photodiode, and is justified by the fact that thermal noise is not a relevant factor at these timescales.

In Fig. 3.11a raw output of the photodiode read by the DAQ card is shown. The acquisition is triggered simultaneously with the pump pulse lasting 650 μs in the displayed case. Each pulse is then averaged and displayed in Fig. 3.11b. The initial noise (first N $\sim$ 30 pulses) is due to thermal effects in the AOM and all the points with N $<$ 30 are discarded, and the solid lines represent a mean of the remaining data points. As active stabilization of $\sim$ 300 μs pulses proved to be a relatively involved task, reduction of the diffracted power errors was achieved by discarding the data points with high input intensity fluctuations, and the dashed lines in Fig. 3.11b represent intensities with tolerance 5 % of the mean, a cut-off value for this procedure.

3.2.4 B-field control and measurements

The B-fields in the experiment are controlled by sending a control voltage to the 4 circuits controlling the current through the Helmholtz and anti-Helmholtz coils around the MOT cell. The schematics of the circuit is depicted e.g. in Fig. D.6 of Ref. [119]. The circuit consists of a differential amplifier and an integrator, which outputs to the gate pin of a current controlling MOSFET. The voltage drop across a resistor in the coil circuit is sent to the non-inverting input of the differential amplifier. In this way, the inductance spikes arising from rapid switching of the coil current are filtered out by a low pass filter of an integrator, using a feedback loop sensing the current through the coils. The field is ramped on/off in the period of 1 ms. However, the presence of eddy currents lasting up to 3 ms after the switch-off start was detected by Gaussmeter measurements (see Fig. 3.12). As is seen in Fig.

3.12, a waiting time of 3.5 ms is a sufficient waiting time for the B-field to reach steady state. The Gaussmeter is expected to provide accurate measurements of the B-fields in the center of the cloud due to relatively narrow dimensions of the cell, allowing for placing the device near the cell center. Subsequent measurements of non-linear Faraday rotation at different points of time after B-field switching confirmed this conclusion.

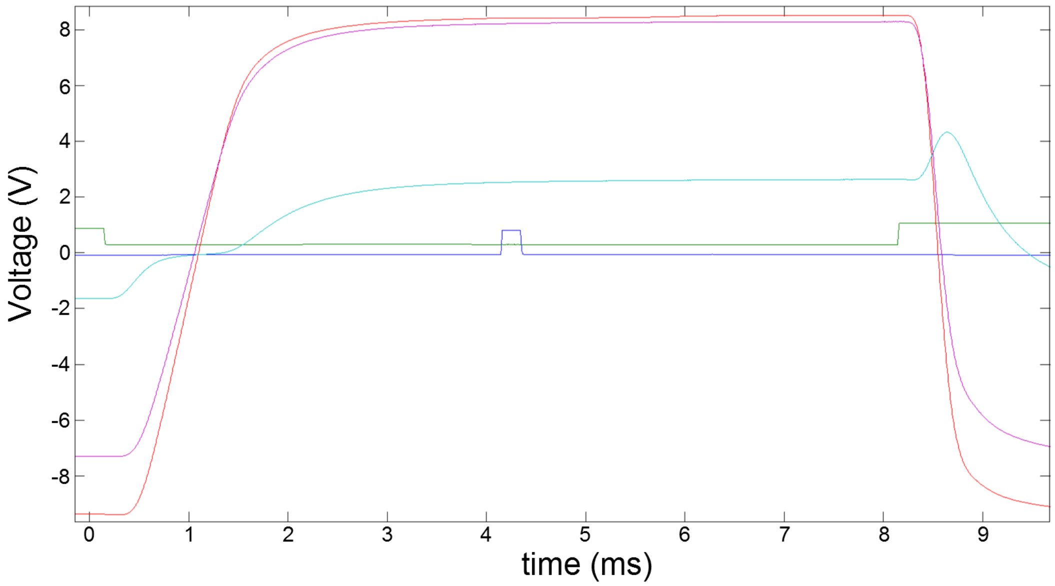

FIGURE 3.12: B-field switching. The fields in x (parallel), y (orthogonal), and z (longitudinal) directions are measured by a Gaussmeter with conversion factor of 10 V/G. Blue: pump beam detected by a photodiode, which marks the start of the pump process (rising edge). Green: MOT beam detected by a photodiode, marking the start of the B-field switching process (falling edge). Magenta: longitudinal B-field (B_z). Red: parallel B-field (B_x). Cyan: orthogonal B-field (B_y). During the switching process the anti-Helmholtz coil was turned off and a B-field in the orthogonal direction added via one of the Helmholtz coils, to illustrate the behavior for a typical experimental run.

The complex Zeeman sub-level structure of the $F = 2 \rightarrow F' = 3$ transition offers myriad mechanisms for measuring the B-field via polarization sensitive atom excitation and light detection [71, 127]. However, as only the zero of the field was needed, the simple non-linear Faraday effect [78] could be used to minimize the field. Using the coil current values for cancelling the external B-fields, the absolute value of the B-field inside the atomic cloud was determined by calibrating the bias coils with a Gaussmeter placed near the cell.

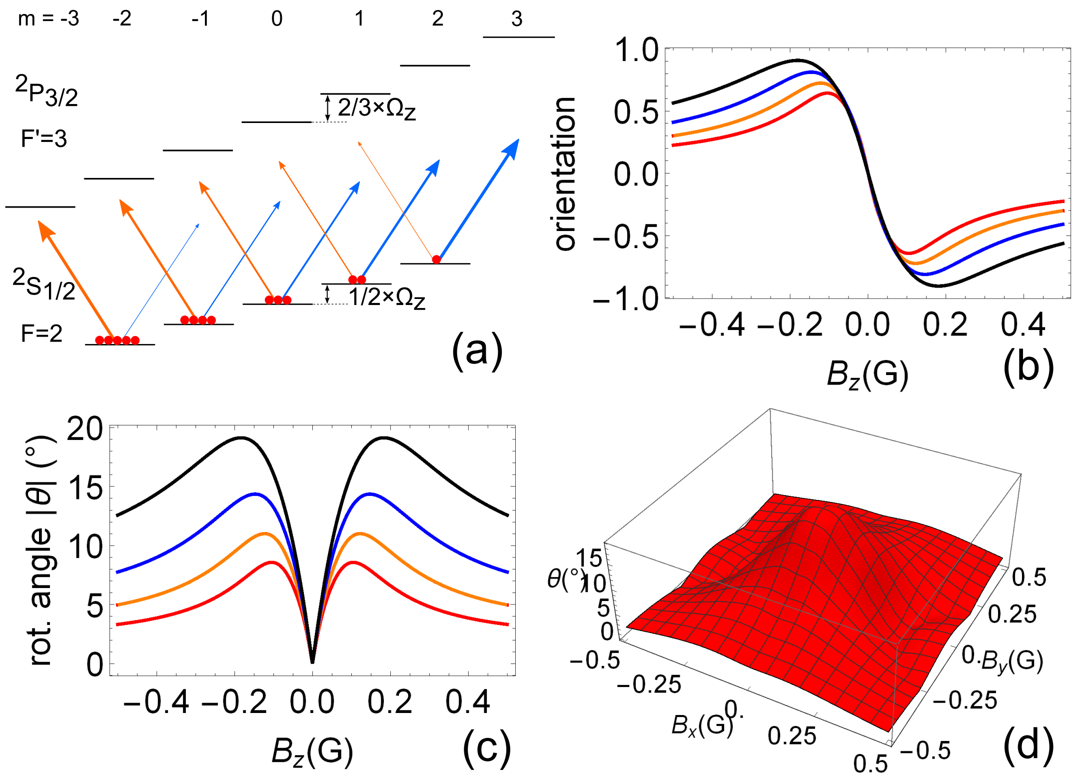

FIGURE 3.13: Simulations of the non-linear Faraday effect used to find the minimum of the B-field. (a) schematics of atom-light coupling of the $\sigma^{\pm}$ transitions and the population imbalance, caused by the asymmetry in the effective detuning of the two circular light components. (b) orientation, as defined in Sec. 2.1.2, vs. the B_z field. Simulation parameters: $B_x = B_y = 0$. Red: $\Delta = -8\Gamma_1$. Orange: $\Delta = -7\Gamma_1$. Blue: $\Delta = -6\Gamma_1$. Black: $\Delta = -5\Gamma_1$. (c) absolute value of rotation angle θ. Simulation parameters: $I_0 = 70$ mW/cm^2, $B_x = B_y = 0$. Colors same as in (b). (d) rotation vs. the two transverse B-field components. Simulation parameters: $B_z = 0.15$ G, $\Delta = -5\ \Gamma_1$. For all plots transient relaxation and repopulation rates $r = 0.001\ \Gamma_1$, optical thickness $b_0 = 30$ and the input beam intensity $I_0 = 70$ mW/cm^2.

Fig. 3.13 shows the mechanism of measuring the B_z field. For high pump intensities $I > I_{sat}$, the horizontally linearly polarized detuned light pumps predominantly into one of the stretched states of the $F = 2$ ground level when Zeeman splitting by the B_z field is present. For a red detuned beam ($\Delta < 0$) and positive

$B_z > 0$, the detuning for the positive circular component is higher than the detuning for the negative circular component. For small B_z fields of $|B_z| = 0 - 500$ mG, the Zeeman shifts are $\Omega_z = 0 - 0.115\ \Gamma_1$ and the linear Faraday rotation is small due to $\Omega_z \ll \Gamma_2, \Delta$ [77]. Due to the asymmetry caused by the small B_z, the high intensity beam pumps the atoms preferentially into $m < 0$ states for $B_z > 0$ and $m > 0$ for $B_z < 0$, creating a population imbalance, which will result in an asymmetry of phase shifts $\varphi_+ \neq \varphi_-$, and ultimately a rotation of the linear polarization.

To see how the difference in phase shifts causes a rotation of the beam polarization, one can write the linear components of the light as $E_x = \frac{1}{2}(E_+ + E_-)$ and $E_y = \frac{i}{2}(E_+ - E_-)$ (using now the electric field convention where $E_+ = (E_x - iE_y)/\sqrt{2}$ and $E_- = (E_x + iE_y)/\sqrt{2}$), their initial field amplitudes for horizontally linearly polarized light are $E_+ = E_- = E_0$. The phase shifts of the two circular components acquired by passing through the medium are then $E_0 e^{i\varphi_\pm}$. The parallel (E_x) and orthogonal (E_y) beam components, analyzed by a PBS and measured by a detector are then $I_{x,y} = |E_{x,y}|^2 = \frac{|E_0|^2}{2}(1 \pm \cos(\varphi_+ - \varphi_-))$. The difference in effective phase shifts caused by population asymmetry is now seen to cause the field to rotate and acquire a component E_y in the axis orthogonal to the input light, and Fig. 3.13c shows the variation of absolute value of the rotation angle $\theta = \arctan(E_y/E_x)$ with the B_z field. The depumping of orientation caused by the transverse fields is shown in Fig. 3.13d to cause a decay of the rotation feature, and the fields were minimized by measuring this decay in experiment.

The experimental measurements of the Faraday rotation angle are depicted in Fig. 3.14. The maximum rotation angle is $|\theta| \approx 22.5°$, which agrees well with the simulation results of Fig. 3.13, for the depumping rate $r = 0.001\ \Gamma_1$ (free parameter) chosen. The width of the rotation dip of the longitudinal field scan is slightly higher than expected from the theory curves at the detuning $\Delta = -5\ \Gamma_1$, which is likely a result of stray B-field gradients due to the ferromagnets in the ion pump, located ≈ 50 cm from the MOT chamber. The stray gradient B-field can not be canceled in the present setup, where the current through the coil pairs of the bias coils in the Helmholtz configuration is varied. The cancellation of the gradient would require the current in each coil of the pair to be varied independently. The transverse fields increase the depump rate of the spin, which reduces the steady state w and consequently the rotation angle.

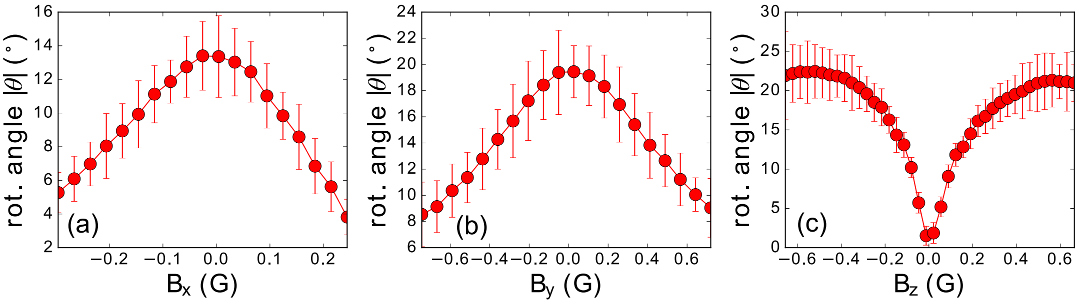

FIGURE 3.14: Absolute value of the polarization rotation angle θ, rotated by the non-linear Faraday effect. Lines are guide to the eyes. Scans of: (a) parallel B-field B_x, (b) orthogonal B-field B_y, (c) longitudinal B-field B_z. Experimental parameters (common to a, b, c): $\Delta t = 300\ \mu$s, $b_0 = 25$, $I = 70$ mW/cm^2, $\Delta = -5.34\ \Gamma_1$. (a) $B_y = 0$, $B_z = 0.15$ G, (b) $B_x = 0$, $B_z = 0.36$ G, (c) $B_{x,y} = 0$.

Non-linear Faraday rotation provides a simple and convenient means to minimize the B-fields in the experiment. The procedure was applied routinely to determine the minima of the B-fields, required for both optimal MOT preparation and controlled pattern formation experiments.

Chapter 4

Experimental results

In this Chapter the results of the magnetization pattern formation experiments are presented. The properties of the magnetization patterns are dependent on the direction and strength of the applied external B-field. The B-field affects the dynamics of the atomic magnetic moments through the interaction part of the Hamiltonian, which in turn affects their optical properties. For the system with feedback this means that the pattern properties will also depend on the B-field. The switching between pattern formation based on four-wave mixing and three-wave mixing is demonstrated to be a result of the applied longitudinal field, breaking the inversion symmetry of the system. A wealth of pattern symmetries is observed in the four-wave mixing case. Application of the longitudinal B-field also breaks the symmetry between the diffracted power in the two circular polarization channels, while the transverse B-fields cause the diffracted power to decay. The magnetization pattern phase space with respect to beam detuning and intensity is mapped, and its properties compared to that of the patterns with optomechanical and two-level non-linearities.

4.1 Region of instability

The region of existence of the polarization instability is shown in Fig. 4.1. This plot shows the diffracted power in the polarization channel orthogonal to input polarization, normalized to maximum, for parameters: $d = -4.16$ mm (distance from the center of the cloud to the mirror), $B_{x,y,z} = 0$, $\Delta t = 300$ μs and $b_0 = 27$. The patterns are seen to exist for detunings of $\Delta < -4\ \Gamma_1$ with the lower limit of intensity in the ~ 5 mW/cm^2 range. For an input beam with lower detuning the absorption prevents the pattern formation by decreasing the transmission and consequently the amount of light in the mirror feedback loop. The contrast peaks at detunings of $-12 < \Delta < -8\ \Gamma_1$ and intensities $50 < I < 200$ mW/cm^2. At the intensities of $I > 450$ mW/cm^2 the contrast again decays due to bleaching of the atoms by saturation, while the decrease of contrast at detunings of $\Delta < -12\ \Gamma_1$ is a consequence of the decrease of the linear refractive index, reducing the atom-light interaction and thus reducing the amplification of fluctuations inside the cloud by the single-mirror feedback loop.

The observed threshold intensities of the magnetization patterns on the order of 5 mW/cm^2 are lower than the ones for optomechanical instabilities reported in Ref. [18]. In this paper the threshold for a cloud with $b_0 = 20$ was measured to be 457 mW/cm^2 at detuning of $\Delta = +6\ \Gamma_1$. The instabilities based on the saturable non-linearity have even higher thresholds, with appreciable pattern contrast starting for an optical thickness of $b_0 = 90$ for a fixed input intensity of $I = 457$ mW/cm^2 and detuning $\Delta = +6\ \Gamma_1$, as reported in Ref. [18]. At fixed $b_0 = 210$ the lowest threshold intensities of $I = 100$ mW/cm^2 were observed, as reported in Ref. [19]. The threshold properties support the conclusion that the optomechanical and saturable non-linearities are not expected to be the primary drivers of the instability observed in this Thesis.

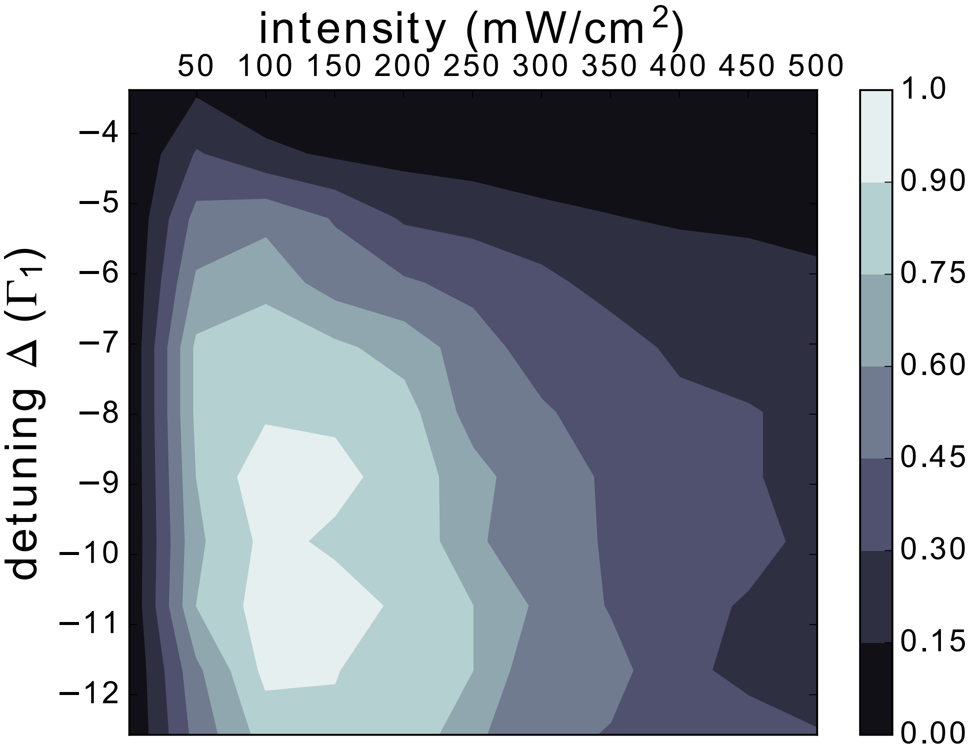

Figure 4.1: Diffracted power in the orthogonal polarization channel (normalized to maximum) for parameters: mirror distance $d = -4.2$ mm, B-fields $B_{x,y,z} = 0$, pump time $\Delta t = 300$ μs and on-resonance optical thickness $b_0 = 27$.

4.2 Breaking of inversion symmetry

As explained in Chapter 1, the allowed symmetry of a patterned state depends on whether the inversion symmetry is present or not in the system. In the lowest order approximation (i.e. near threshold), the hexagons are the only allowed patterns if the inversion symmetry is broken, whereas any pattern can occur in a system where inversion symmetry is preserved [23]. The near-field (NF) images of patterns at various B-fields are shown in Fig. 4.2. The first column shows images of pattern realizations for $B_z = -80$ mG, the second for $B_z \approx 0$ (where the "≈" symbol means the B-field was minimized to the experimentally available limit, as described in Sec. 3.2.4) and the third for $B_z = 120$ mG. The first row shows σ^+ light, the second σ^- light and the third a subtraction of σ^+ and σ^-. For $B_z < 0$ the σ^- light forms positive hexagonal patterns (HX$^+$) and the σ^+ light forms negative hexagonal patterns or honeycombs (HX$^-$), and the situation is reversed for $B_z > 0$. In the realization shown in Figs. 4.2b, e, h for $B_z \approx 0$ the patterns have a rectangular (RC) symmetry, however it needs to be noted that for $B_z \approx 0$ other symmetries can also appear near threshold, as shown in Fig. 4.4.

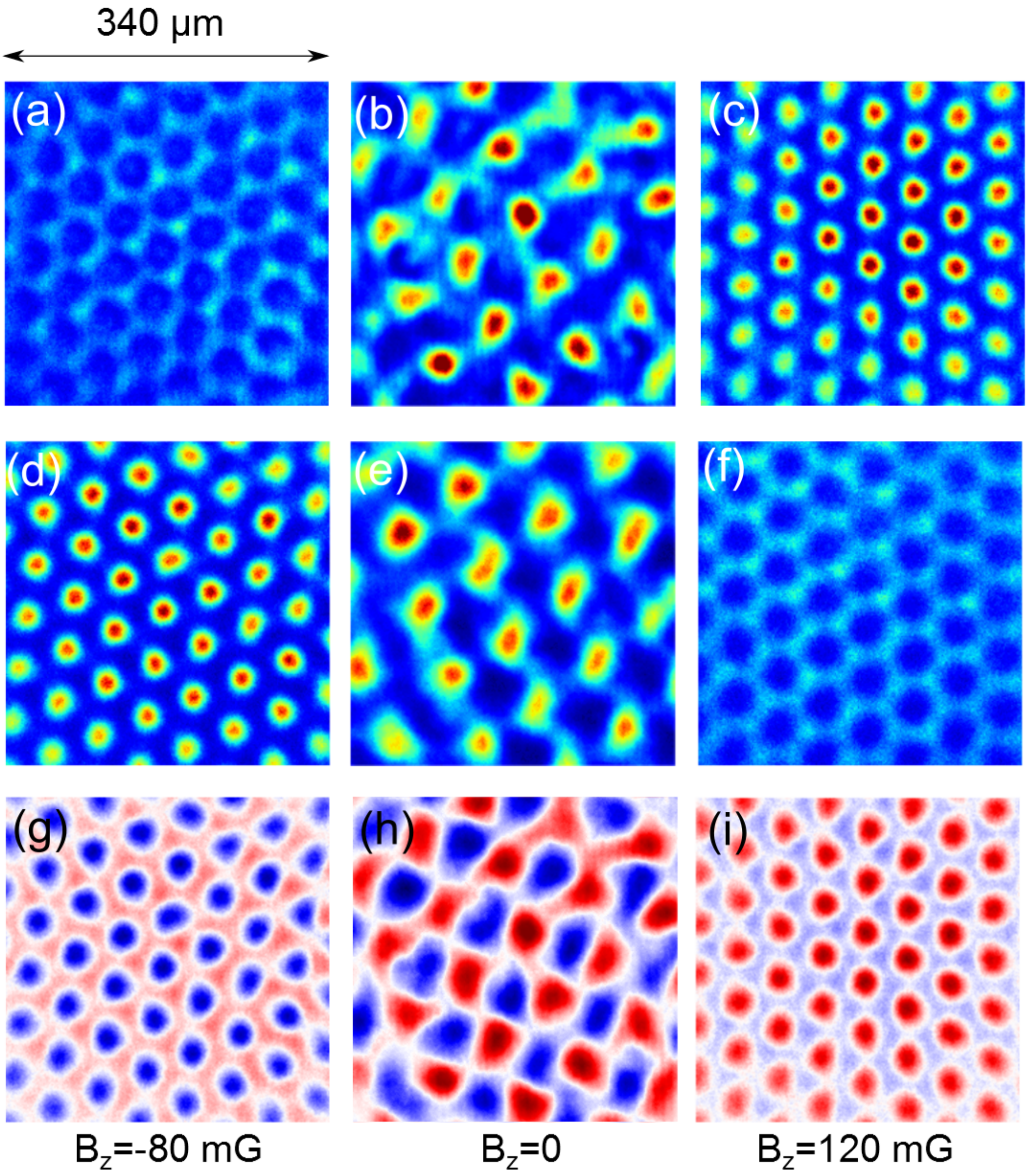

FIGURE 4.2: Breaking of the inversion symmetry by Faraday rotation. The near field imaging is done in the plane a quarter of the Talbot distance from the end of the cloud, where beam phase modulations are fully converted into amplitude modulations. Columns: images for $B_z = -80$ mG (first) $B_z \approx 0$ mG (second) and $B_z = 120$ mG (third). Rows: σ^+ polarization channel (first), σ^- polarization channel (second) and the difference between the two channels (third). Experimental parameters: $I \approx 10$ mW/cm^2, $\Delta = -7\ \Gamma_1$, $d = -2.88$ mm (first and third columns), $d = 2.2$ mm (second column), $\Delta t = 250\ \mu$s.

The subtracted images in the last row of Fig. 4.2 show clearly the complementarity of the regions of dominant $\sigma^{\pm}$ light. The complementary modulation of $\sigma^{\pm}$ light is a consequence of the instability being based on the spin variable w, as will be discussed in Chapter 5. The feedback, maximizing the spin modulation, forms two sublattices, one for the σ^{+} light, and one for the σ^{-} light. The difference of the near field images of $\sigma^{\pm}$ light patterns, shown in Figs. 4.2g, h, i, is proportional to the driving term $\mathcal{D}$ of the spin variable w, as defined in Chapter 2. These images can then be interpreted to be proportional to the atomic spin variable w, and the transverse pattern symmetries related to the phases of atomic magnetization. For $B_z > 0$ the modulation depth of the σ^{+} hexagonal lattice is greater than the modulation depth of the σ^{-} hexagonal lattice, while the converse is true for $B_z < 0$. For $B_z \approx 0$, the modulation depths of the two lattices are approximately equal. The $B_z \neq 0$ phase is thus analogous to the *antiferromagnetic* phase, while the $B_z < 0$ and $B_z > 0$ phases are analogous to the *ferrimagnetic* phase in condensed matter systems. By definition, the antiferromagnetic ordering has two magnetic sub-lattices with spins of equal magnitude and opposite orientation, while the magnetization sub-lattices in a ferrimagnetic ordered system have spins of opposite orientation and unequal magnitude [128]. One notes that both the interpretation and the analogy of the patterns with magnetic phases does not change for the $B_z = 0$ case for symmetries other than rectangular or square.

To estimate the number of atoms in each peak of the near-field image one can first estimate the total number of transverse peaks to $\gtrsim 100$ (see Fig. 3.9). The depth of field of the 2.5× magnifying imaging setup (with a numerical aperture of ~ 0.1) is ~ 100 μm. The total number of atoms in the cloud is $\sim 10^9$, and the length of the cloud is 1 mm. From these numbers one calculates the upper estimate of $\sim 10^6$ atoms per peak.

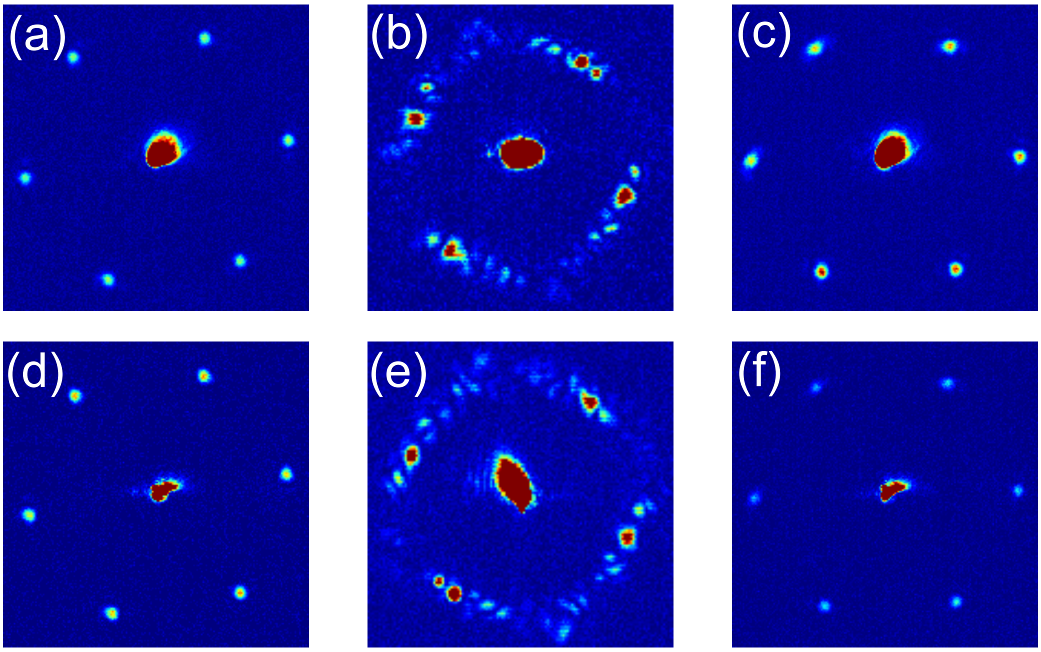

FIGURE 4.3: Far-field images taken simultaneously as near-field images of Fig. 4.2. The parameters and the image ordering are the same as in Fig. 4.2.

Figure 4.3 shows far-field (FF) data of the same patterns observed simultaneously. The FF images show the zero order peak of the transmitted Gaussian envelope, and the well defined sideband peaks with the three axes at angles of 60° for $HX^{\pm}$ and the two axes at 75° for RC. As was explained in Chapter 1, the interference of the zero order and the sidebands causes the amplitude modulation of the beam at the quarter of the Talbot distance. The amplitude of the sidebands (proportional to the diffracted power) of the σ^+ lattice is higher than the amplitude of the σ^- lattice for $B_z > 0$, while the converse is true for the $B_z < 0$ case. For $B_z \approx 0$ the amplitudes are approximately equal. The axis angles of a few other pattern realizations at $B \approx 0$ are denoted in Fig. 4.4, where squares (SQ), rectangles (RC), rhombs (RB) and stripes (ST) are shown. The angles of the sideband axes fluctuate randomly from shot to shot, and a wide range of angles has beed observed experimentally, implying that the factors $g_{il}(\theta_{il})$ in the threshold equations of the type (1.11) vary weakly on the angles θ_{il}.

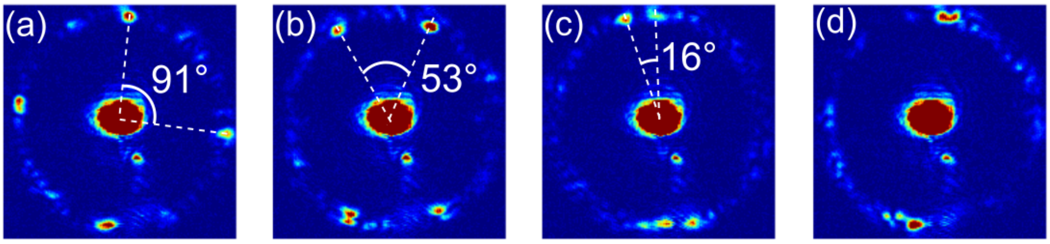

FIGURE 4.4: Examples of observed pattern symmetries for the inversion symmetric case ($B_z = 0$): (a) squares (SQ), (b) rectangles (RC), (c) rhombs (RB), (d) stripes (ST). All images are in the far-field of the σ^+ polarization channel. The experimental parameters for this data are: $d = -3.5$ mm, $I = 7$ mW/cm^2, $B_{x,y,z} = 0$, $\Delta = -7\,\Gamma_1$, $\Delta t = 300\ \mu$s, $b_0 = 27$.

The presence of a longitudinal B-field provides a mechanism for breaking the inversion symmetry of the system. This is done by changing the optical response of the atomic medium (i.e. its refractive index) for σ^+ and σ^- light components. As will be discussed in Section 4.5, the previous experiments in hot vapours reported in Refs. [129, 130] used less direct ways of breaking the inversion symmetry.

4.3 Instability onset

Fig. 4.5 shows the diffracted power against pump time for three different input beam intensities. Each data point corresponds to a single realization of the pattern, without accounting for input beam intensity noise. The pumping time required for reaching the patterned steady state is dependent on the input intensity, as is expected for a non-linearity based on optical pumping into magnetic sublevels, where a certain number of photons needs to be absorbed and spontaneously emitted for pumping to occur. The timescales of $10 - 100\ \mu$s are consistent with the interpretation that the non-linearity is based on Zeeman sublevel optical pumping. The scattering rate of photons by a single atom is given by [22]

$$\Gamma_{scatt} = \Gamma_2 \frac{s(\Delta)}{1 + s(\Delta)} \tag{4.1}$$

where $\Gamma_2 = \Gamma_1/2 = 19.06$ MHz [72] is the optical coherence decay rate and s is given by Eq. (2.14). For a circularly polarized beam with intensity of $I = 5$

mW/cm^2 ($I_{sat} = 1.669$ mW/cm^2 [72]) and detuning $|\Delta| = 14\ \Gamma_2$, a photon will on the average be scattered each $\tau = 1/\Gamma_{scatt} = 3.5\ \mu$s. Considering that the number of photons scattered to reach steady state is on the order of $5-10$, the timescales are on the order of $17.5-35\ \mu$s, which is consistent with the results shown in Fig. 4.5, where for the beam of total intensity $I = 9.3$ mW/cm^2 (meaning each circular component has $I_\pm = 4.65$ mW/cm^2) noticeable diffraction starts around $t \approx 25\ \mu$s of pumping time.

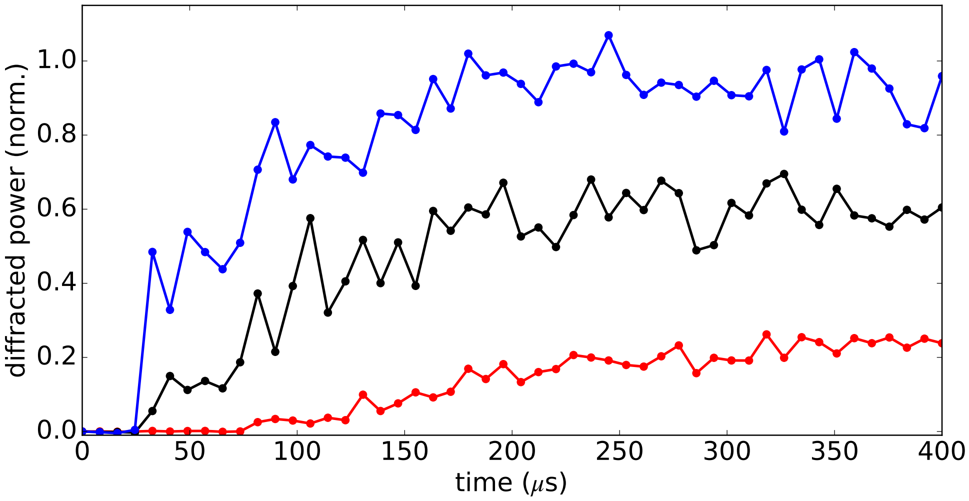

FIGURE 4.5: Dependence of the total diffracted power (normalized to maximum) on pump duration Δt for parameters: $d = -4.2$ mm, $\Delta = -7\ \Gamma_1$, $B_{x,y,z} = 0$ and $b_0 \approx 27$. Red: $I = 3.6$ mW/cm^2. Black: $I = 6.8$ mW/cm^2. Blue: $I = 9.3$ mW/cm^2.

In the previous work with optomechanical [18] and saturable [19] non-linearities, the timescales were on the order of 0.1 ms and ~ 100 ns, respectively. In these experiments the timescales of pattern onset and decay were crucial in providing the signatures used to determine the types of non-linearities responsible for the pattern formation. In the Zeeman non-linearity case, the origin of the non-linearity is clear from the start. One reason for this is because both of the competing non-linearities (i.e. optomechanical and saturable) are insensitive to the light polarization, meaning that the vectorial aspect of the electric field can be ignored. In addition to the absence of modulated light at the polarization orthogonal to the input polarization, another reason for this was the complete independence of pattern properties on the applied B-fields, as reported in Refs. [18, 19], which is not the case for patterns observed in this Thesis.

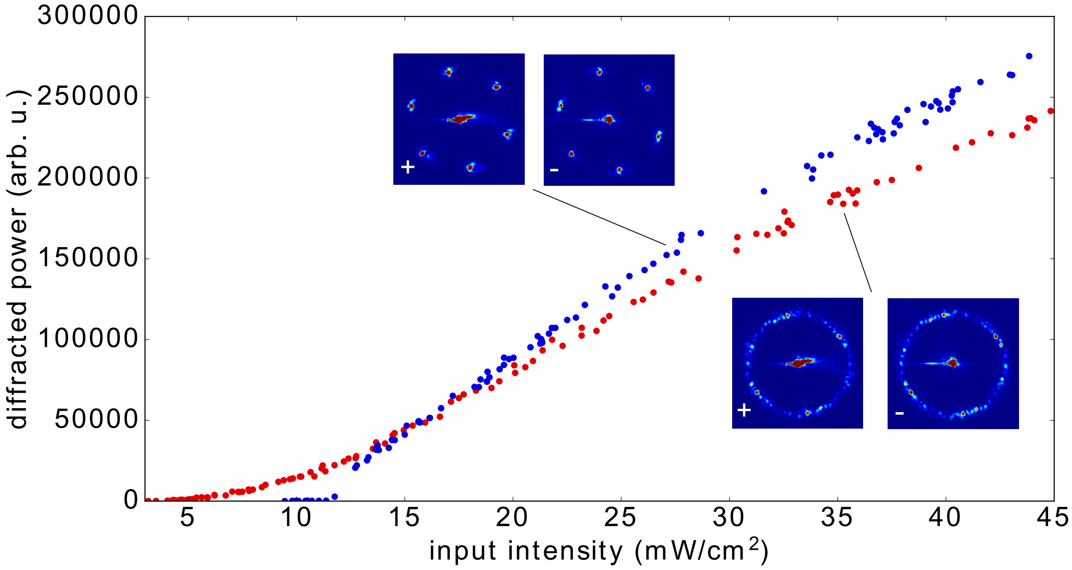

FIGURE 4.6: Total diffracted power for varying input beam intensity. Red: $B_z \approx 0$. Blue: $B_z = 130$ mG. Experimental parameters: mirror distance $d = -2.9$ mm, detuning $\Delta = -7\ \Gamma_1$, B-fields $B_{x,y} = 0$, pump time $\Delta t = 300\ \mu$s, and on-resonance optical thickness $b_0 \approx 27$.

In spite of the fact that the optomechanical non-linearity most likely plays a negligible role in the self-organization procedure, there is no reason to a priori exclude the existence of atomic density modulations in the transverse plane. However, probing the interplay between cooling of the atomic motional degrees of freedom and spin self-organization is beyond the scope of this Thesis.

Fig. 4.6 shows the total diffracted power for $B_z = 130$ mG (blue) and $B_z \approx 0$ (red) and the measured far-field images at the denoted intensities. Each data point represents a single realization (shot) of the patterns, and the input beam intensity is monitored by a photodiode. The gain is seen to be slightly higher for the $B_z = 130$ mG case and the thresholds roughly coincide. The $B_z = 130$ mG patterns show a discontinuity at $I \approx 12$ mW/cm^2, whereas the $B_z \approx 0$ patterns show a more continuous increase. This is an indication that the bifurcation for the

$B_z = 130$ mG is subcritical, whereas the $B_z \approx 0$ patterns are supercritical, and also a confirmation that the wave mixing process in the $B_z \approx 0$ case is four-wave and in the $B_z = 130$ mG case it is three-wave. In Fig. 4.7 the diffracted power divided by the input power (normalized to maximum) is plotted for the same data as in Fig. 4.6. The displayed quantity is now anticipated to be proportional to the order parameter, and the curves are reminiscent of the curves for first and second order phase transitions [131].

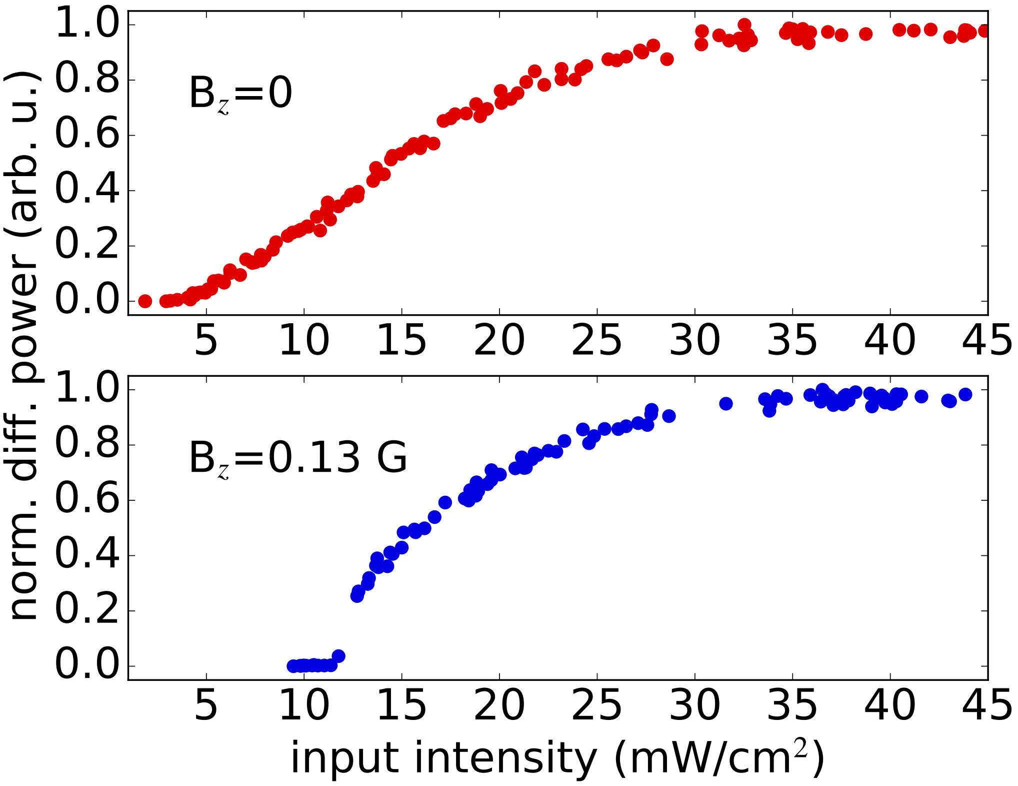

FIGURE 4.7: Total diffracted power normalized to the input power. Red: $B_z \approx 0$. Blue: $B_z = 130$ mG. Experimental parameters are the same as in Fig. 4.6.

4.4 Scanning the B-fields

Fig. 4.8 shows a scan of the B_z field up to $|B_z| \approx 150$ mG for three input intensities. To minimize the noise induced by fluctuations of the pump intensity, for each shot the intensity was measured, and subsequently the data point discarded if the value deviated by more than 5% from the mean intensity value, as was described in Sec. 3.2.3. The points in the plot correspond to the mean values of diffracted power, averaged typically for more than 5 shots. An excess of σ^+ (σ^-) diffracted light for $B_z > 0$ ($B_z < 0$) is observed, along with the decay of diffracted power in both channels at higher B_z (i.e. $|B_z| \approx 150$ mG, for $I = 14$ mW/cm^2).

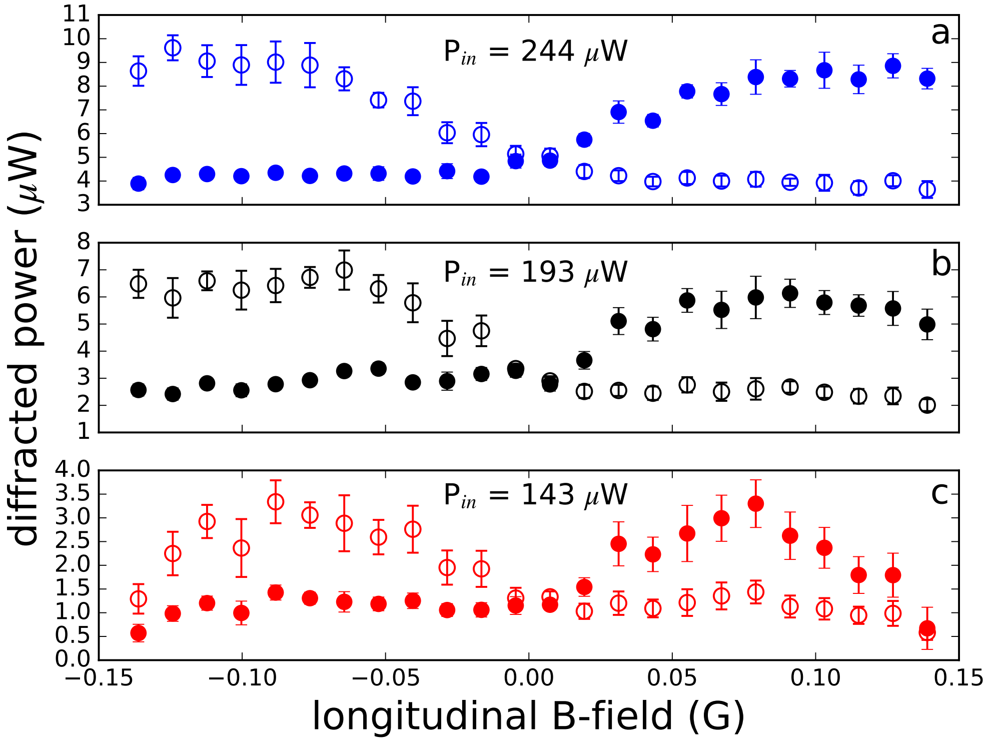

FIGURE 4.8: Scan of the longitudinal field B_z for small values around $B_z = 0$. (a) $I = 24$ mW/cm^2. (b) $I = 19$ mW/cm^2. (c) $I = 14$ mW/cm^2. Full circles: σ^+ light, empty circles: σ^- light. Experimental parameters: mirror distance $d = -2.9$ mm, detuning $\Delta = -7\ \Gamma_1$, B-fields $B_{x,y} = 0$, $\Delta t = 300$ μs and on-resonance optical thickness $b_0 \approx 27$.

The error bars of the hexagonal ($|B_z| \geq 30$ mG) phase typically are larger than the error bars of the stripe/rectangle phase. This is in accordance with data shown in Fig. 4.6 where a discontinuity was observed for a finite B_z. The B_z field scan shows a clear asymmetry in the diffracted power for the case of $|B_z| \gtrsim 15$ mG, and a symmetry for the $B_z < 15$ mG case.

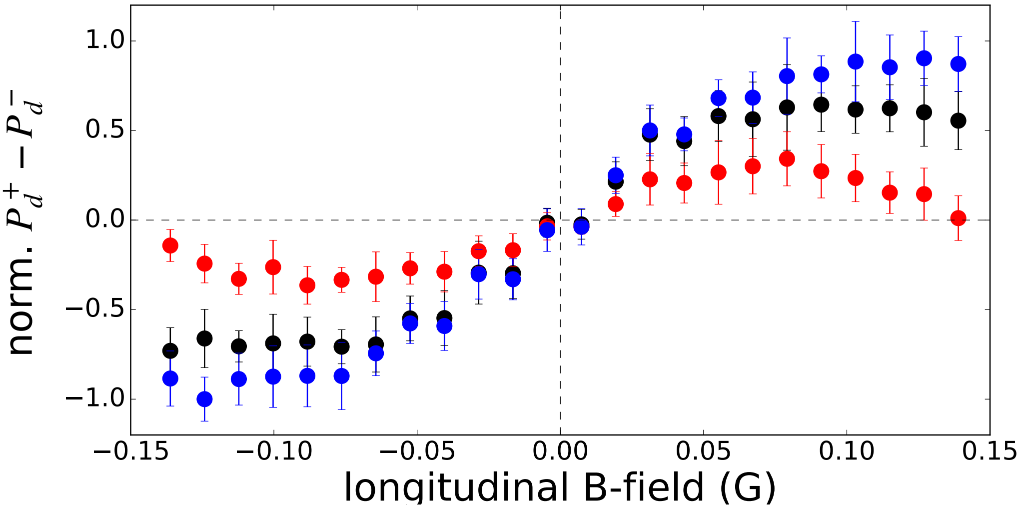

FIGURE 4.9: Difference of the diffracted powers in the $\sigma^{\pm}$ polarization channels. Experimental parameters are the same as in Fig. 4.8.

The diffracted power asymmetry is further illustrated in Fig. 4.9, where the difference of diffracted power in the two circular polarization channels is plotted against B_z, for the same data as in Fig. 4.8. The difference in the diffracted power initially grows for small B_z fields, and then starts dropping. The width of the pattern existence region increases with the input pump power, which will also be the case for the simulation results of Ch. 5. The plot shows a clear imbalance between the diffracted power in the two channels for an applied B_z field, with σ^+ light being dominant for $B_z > 0$ and the σ^- dominating for $B_z < 0$. The quantity can be related to the total dipolar magnetism in the transverse plane of the cloud, where a presence of an excess modulation of the spin $\delta w > 0$ ($\delta w < 0$) sublattice for $B_z > 0$ ($B_z < 0$) can be inferred from this data. This supports the conclusion that the magnetism in the $B_z \neq 0$ case is ferrimagnetic, while in the $B_z = 0$ case it is antiferromagnetic (see Sec. 5.3.1).

The total diffracted power is plotted against B_z field in Fig. 4.10. The maximum diffracted power for the given parameters is at $B_z = 0$. The diffracted power decays completely at $|B_z| = 0.4$ G and then starts increasing again for higher $|B_z|$ values. The maximum B_z field in the negative direction is limited by the fact that the Helmoholtz coil pair used to set the field is also used to minimize the stray B-fields, so the range is fixed by the current direction.

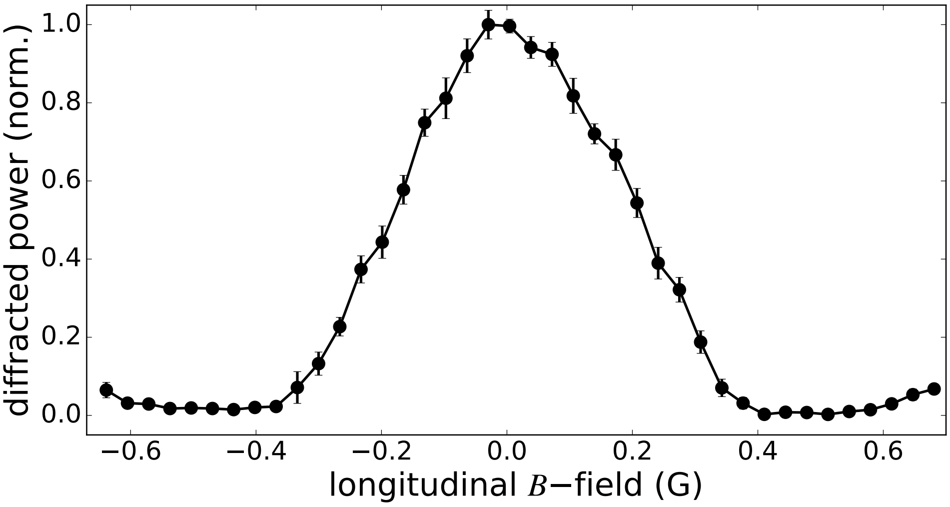

FIGURE 4.10: Total diffracted power normalized to maximum. The experimental parameters are: pump intensity $I = 17$ mW/cm^2, mirror distance $d = -4.2$ mm, detuning $\Delta = -7\ \Gamma_1$, B-fields $B_{x,y} = 0$, $\Delta t = 300\ \mu$s and on-resonance optical thickness $b_0 \approx 27$.

The transverse field scans are shown in Fig. 4.11. The effect of both of the transverse B-fields in the directions parallel and orthogonal to the input beam polarization are seen to be roughly equal. As can be inferred for the scans at different input powers, the fields work to reduce the diffracted power and increase the threshold intensity. It is expected that the transverse field reduces the optical pumping by spin flips which can then prevent the pattern formation driven by the orientation. The results of Fig. 4.11 are then a further confirmation of the conclusion that the patterns are indeed in the magnetic dipole (spin) degree of freedom of the atoms inside the cloud.

The measured pattern properties will be reproduced by the simulations, as presented in simulation results shown in Chapter 5.

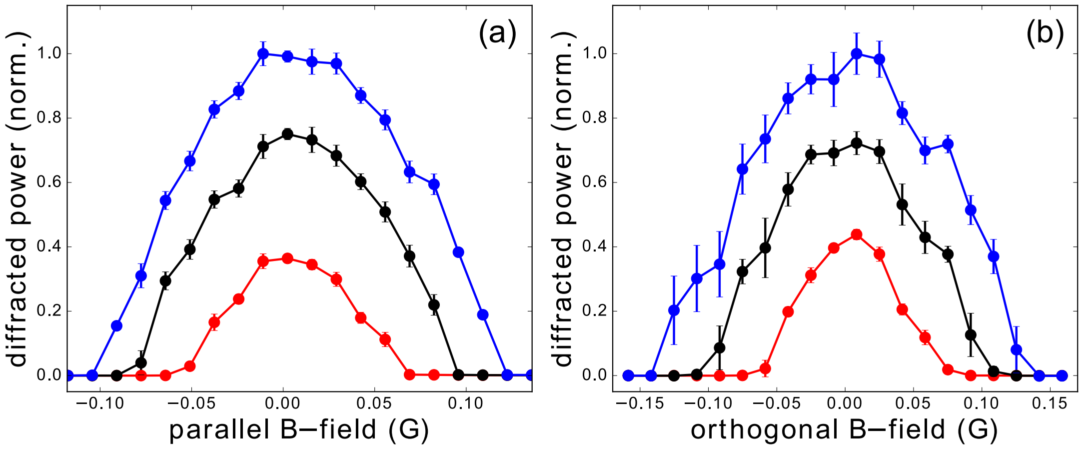

FIGURE 4.11: Total diffracted power vs. transverse B field scans. (a) B_x scan and (b) B_y scan. Red: $I = 7$ mW/cm^2. Black: $I = 10$ mW/cm^2. Blue: $I = 12$ mW/cm^2. The experimental parameters are: mirror distance $d = -4.2$ mm, detuning $\Delta = -7\ \Gamma_1$, B-fields zero unless indicated, $\Delta t = 300\ \mu$s and on-resonance optical thickness $b_0 \approx 27$.

From the variation of the diffracted power at fixed input power with the B_z-field (Fig. 4.10) one can expect that also the thresholds for pattern formation will vary with the B_z-field. These results are shown in Fig. 4.12. The threshold intensity rapidly increases until $B_z = 0.23$ G, after which it starts decreasing and reaches a constant value of $I_{th} \approx 4$ mW/cm^2 for $B_z > 0.7$ G.

As noted before, the pattern symmetries also depend on the applied B_z-field. The red shading in Fig. 4.12 indicates the phase where rectangles, squares and stripes are a typical solution, going from $B_z = 0$ to $B_z = 0.04$ G. For B_z fields in the range $0.04 < B_z < 0.23$ G (blue) the solutions are hexagons with the diffracted power from the σ^+ sublattice being clearly greater than the diffracted power in the σ^- sublattice, as is shown in Fig. 4.9. For even higher B_z-fields (magenta), until the maximum B_z value applied ($B_z = 1.33$ G), the typical solutions are rectangles and stripes. The diffracted power of σ^- light is now greater than the diffracted power of σ^+ light, opposite to the case of moderate B_z-field (blue). The theoretical investigation of this high B_z phase is still ongoing.

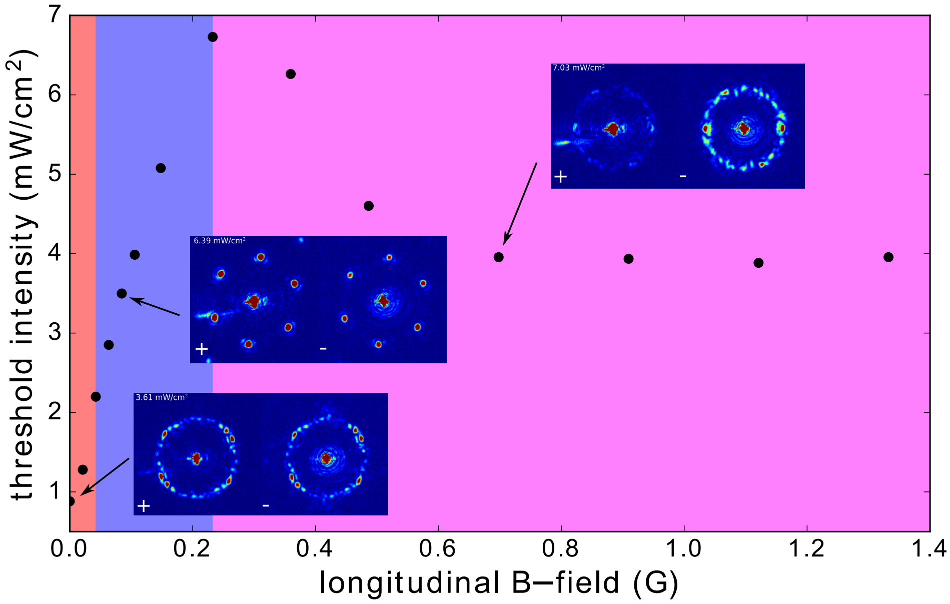

FIGURE 4.12: Pattern threshold intensities for varying the B_z-field. The shaded regions indicate the regions of symmetry of the patterns with the insets showing the typical FF data in the $\sigma^{\pm}$ polarization channels of the pattern realizations in the given region, for the denoted values of beam intensity and longitudinal B-field. The experimental parameters are: mirror distance $d = 1.28$ mm, detuning $\Delta = -7\ \Gamma_1$, transverse B-fields $B_{x,y} = 0$, pump time $\Delta t = 300$ μs and on-resonance optical thickness $b_0 \approx 27$.

4.5 Relation to previous work

Previous experimental work on Zeeman instabilities in hot Na vapours was performed with both circular [13, 14] and linear input light [129]. In the case of circular light, the inversion symmetry of the system is broken by the input light, and the pattern symmetries are hexagonal. As there is no generation of modulated light with a polarization mode orthogonal to that of the input light, the physics can in this case be treated in a quasi-scalar framework. This also means that the interpretation of the patterns as magnetization patterns is not plausible.

In the case of linear input light polarization, the quasi-scalar treatment fails, as the vectorial nature of the light in the feedback loop becomes important. The breaking of the inversion symmetry causing squares (rectangles) to switch to hexagons is done in a less direct way. One way of breaking the inversion symmetry is by increasing the ellipticity of the input light. The change of polarization of the input light from linear to elliptical results in a finite homogeneous solution for the spin variable w_h, which breaks the inversion symmetry of the system [129].

Another way of breaking the inversion symmetry of the system is by light shift or Zeeman splitting. This was done by adding a transverse B-field to the system. The transverse field flips the spins more strongly for a beam close to the resonance of the transition. Adding the light shift or Zeeman splitting (for a fixed detuning Δ), one of the $\sigma^{\pm}$ light components can be brought closer to resonance, increasing the rate of the spin flips by transverse fields. Since the individual circular light components pump into the dark states, the component for which the spin flipping is stronger will couple more strongly to the light, thus breaking the inversion symmetry of the system.

Additional difference from the previous experiments in Na vapours arises from the fact that the previous experiments were done with a $J = 1/2 \rightarrow J' = 1/2$ transition, which allows only dipole physics. The preliminary simulations of the dipole model (i.e. with only w variable included) indicate that the model is insufficient to reproduce the experimental results of Section 4.4, indicating that the influence of the quadrupolar terms on the steady state pattern solution is not completely negligible.

In the experiments performed with hot Na vapors the intensity was scanned across the threshold in both positive and negative directions [132]. For the square phase the scan was shown to fall on a single continuous line, as expected for a supercritical bifurcation, while the hexagons showed a hysteresis, as is characteristic for a subcritical bifurcation. The cold atom experiment described in this Thesis could in the future be modified to detect such a hysteresis, e.g. by inserting a photodiode to continuously measure the sideband power during a millisecond ramp of the input beam intensity. One limiting factor for cold atom experiments with respect to hot vapor experiments is that the scan time is limited by cloud expansion, meaning that (i) the optical thickness is reduced and (ii) the cloud center falls due to gravity for time of flight times on the order of 10 ms. An experimental challenge is then to balance the pump time duration to reach steady state of the patterns on the order of 50 μs (see Fig. 4.5 and discussion thereof) with the transient decay of optical thickness on scales of a few milliseconds. One way to calibrate the ramp time would be to measure first the curve for $B_z \approx 0$, and modify the ramp time to reach lowest hysteresis, and then do the same scan for $B_z \neq 0$ to see the area under hysteresis curve get larger.

Chapter 5

Simulating the magnetization patterns

Single feedback mirror self-organization theory for hot atoms with spin 1/2 was written by Scroggie and Firth in 1996 [133] to provide the framework for the experiments in alkali vapors of Refs. [12, 13] and the simulation results of Le Berre [134]. In the work of Ref. [129] a linearly polarized beam, i.e. possessing equal weights of the circular $\sigma^{\pm}$ components, was used as the input. A symmetry breaking instability occurs in the system when a fluctuation in the spin of the medium, which induces an opposite spatial modulation of the phases of the two circular light components exiting the medium, is strongly amplified by the feedback via phase to amplitude conversion of the Talbot effect.

In the first part of this Chapter the framework of linear stability analysis is employed to illustrate how the spin w drives the instability in the 1D case. It is also explained how the results of the experiment would change in case the instability were a result of maximizing the mirror feedback upon fluctuations of the other atomic variables. In the second part, the results of numerical simulations are presented for the 1D and 2D cases. The scans of the B-fields reproduce well the experimental results of Ch. 4. The symmetries of optical patterns and the atomic variables are also shown and discussed.

5.1 Linear stability analysis

5.1.1 Self-organization via mirror feedback

In the slowly warying amplitude and thin medium approximations, the light propagating through an atomic cloud experiences the medium polarization $\mathbf{P}(\mathbf{r}_\perp, z)$ via the paraxial wave equation [54]

$$\frac{\partial}{\partial z}\mathbf{E}(\mathbf{r}_\perp, z) = -ik\mathbf{P}(\mathbf{r}_\perp, z), \tag{5.1}$$

where $k = |\mathbf{k}|$ is the length of the longitudinal wavevector of the incoming pump beam. In circular polarization components $\sigma^{\pm}$, the above equation can, with the aid of Eqs. (2.23), be cast into the form

$$\begin{cases} \frac{\partial}{\partial z}E_+(\mathbf{r}_\perp, z) = -i\alpha_l^+ \left(\left(1 + \frac{3}{4}w + \frac{1}{20}x\right) E_+(\mathbf{r}_\perp, z) + \frac{3}{20}(u - iv)E_-(\mathbf{r}_\perp, z)\right), \\ \frac{\partial}{\partial z}E_-(\mathbf{r}_\perp, z) = -i\alpha_l^- \left(\left(1 - \frac{3}{4}w + \frac{1}{20}x\right) E_-(\mathbf{r}_\perp, z) + \frac{3}{20}(u + iv)E_+(\mathbf{r}_\perp, z)\right). \end{cases} \tag{5.2}$$

For the sake of simplicity, absorption and linear Faraday effect are neglected in the following discussion (but not in the simulations presented in Sections 5.2 and 5.3.1) due to $\Delta/\Gamma_2, \Delta/\Omega_z \gg 1$. The linear susceptibilities $\alpha_l^{\pm} = k\chi_l^{\pm}$ from (2.23) are now both equal to

$$\alpha = -\frac{b_0}{2L\Gamma_2}\frac{\Delta}{1 + \frac{\Delta^2}{\Gamma_2^2}}, \tag{5.3}$$

where b_0 is the on-resonance optical thickness as measured in experiment, Δ is the beam detuning and Γ_2 is the decoherence rate. The dynamical equations for the atomic variables (2.19) are solved at the end of the medium of length L. The electric fields $E_{\pm}(\mathbf{r}_\perp, z = L) \equiv E_{\pm}$ in the Rabi frequencies $\Omega_{\pm}$ are a superposition of the forward $(F_{\pm}(\mathbf{r}_\perp, z = L) \equiv F_{\pm})$ and backward $(B_{\pm}(\mathbf{r}_\perp, z = L) \equiv B_{\pm})$ propagating fields [133]

$$E_{\pm} = F_{\pm} + B_{\pm}. \tag{5.4}$$

The fields $E_{\pm}$ enter the atomic equations of motion only via terms proportional to $|E_{\pm}|^2$ and $E_+^* E_-$. The treatment described in this Chapter neglects the terms proportional to $\cos 2kL$, i.e. terms $F_+^* B_-$, $F_-^* B_+$, in the transverse pattern formation community reffered to as the longitudinal or reflection grating terms (see Sec. 6 and Ref. [125] for a treatment of a Kerr medium including the reflection gratings). The dynamical equation terms including the total fields are now

$$|E_\pm|^2 = |F_\pm|^2 + |B_\pm|^2, \text{ and } E_+^* E_- = F_+^* F_- + B_+^* B_-. \tag{5.5}$$

The first expression in Eq. (5.5) is the intensity and therefore phase-insensitive, while the second expression contains the interference terms of the two circular components of the forward and backward propagating beams, respectively. This interference is a consequence of the two beam coupling of the two $\Delta m = 2$ ground levels via a single excited state. Free space propagation of an electric field $\mathbf{E}_\pm(\mathbf{r}_\perp, z)$ in $+z$ direction after the cloud is governed by

$$\frac{\partial}{\partial z}\mathbf{E}_\pm(\mathbf{r}_\perp, z) = -\frac{i}{2k}\Delta_\perp \mathbf{E}_\pm(\mathbf{r}_\perp, z), \tag{5.6}$$

where $-$ sign on the RHS changes to $+$ if propagation is in the $-z$ direction, $\Delta_\perp$ is the Laplace operator in the plane transverse to the input beam propagation direction and $k = 2\pi/\lambda$ is the longitudinal wavenumber of the pump laser.

To express more formally the mechanism of single-mirror feedback, one can consider the effect of a modulation in the atomic variables on the backward propagating field. The total forward field exiting the medium is modulated with an amplitude $f_\pm(\mathbf{r}_\perp)$ by the atomic modulations, and can be separated into homogeneous and inhomogeneous parts as

$$F_\pm(\mathbf{r}_\perp, z = L) = F_\pm^0(1 + f_\pm(\mathbf{r}_\perp)). \tag{5.7}$$

This field is propagated to the mirror and back, solving the equation (5.6). Moving to the Fourier space of the transverse coordinate $\mathbf{r}_\perp \to \mathbf{q}$ one gets

$$\Delta_\perp \to -|\mathbf{q}|^2, \text{ and } f(\mathbf{r}_\perp) \to \int f(\mathbf{q})e^{i\mathbf{q}\cdot\mathbf{r}_\perp}\mathrm{d}\mathbf{q}. \tag{5.8}$$

Propagating the above equation (5.7) a distance z after the medium via the diffraction equation (5.6) results in

$$F_{\pm}(\mathbf{q}, z) = F_{\pm}^{0}(1 + f_{\pm}(\mathbf{q})e^{i\frac{|\mathbf{q}|^2 z}{2k}}). \tag{5.9}$$

The backward fields reentering the medium can now be easily calculated by propagating Eq. (5.9) to the mirror with reflectivity R and back. The field reentering the medium at $z = L$, which is a result of propagation to the mirror and back by a distance $l_{pr} = 2d$ (where d is in this Chapter the distance from the end of the medium to the mirror), is equal to

$$B_{\pm}(\mathbf{q}, z = L) = B_{\pm}^{0}(1 + f_{\pm}(\mathbf{q})e^{i\frac{|\mathbf{q}|^2 d}{k}}), \tag{5.10}$$

where $B_{\pm}^{0} = \sqrt{R}F_{\pm}^{0}$. In the linear stability analysis the sideband amplitudes $f_{\pm}(\mathbf{q})$ are for pump intensities near threshold related to the atomic variable modulations with wavevector $\mathbf{q}$. For the application of this framework to the $J = 1/2 \rightarrow J' = 1/2$ system see e.g. [133]. The phase factor of the sidebands is in the transverse pattern formation community known as diffractional phase shift and denoted by

$$\Theta(\mathbf{q}) = \frac{|\mathbf{q}|^2 d}{k}. \tag{5.11}$$

The above equation (5.10) makes apparent how the interference of the zero order and the sidebands influences the atomic variable modulations by mirror feedback. The atom variable fluctuations are random, i.e. they appear at every lengthscale $\Lambda = \frac{2\pi}{|\mathbf{q}|}$ or, more precisely, wavevector $\mathbf{q}$. The Talbot effect converts a phase grating with a period Λ into an amplitude grating with same period at a quarter of the Talbot distance $z_T = 2\Lambda^2/\lambda$ [52]. For the patterns to start growing out of random fluctuations, a positive feedback is needed. Positive feedback in the optically non-linear medium with refractive index $n(I)$ means the refractive index modulation Δn is reflected back to the medium as an intensity modulation with the same pattern and phase (self-focusing medium) or shifted by half a period (self-defocussing medium). Due to the fact that the diffraction length is fixed by the mirror distance d, positive feedback is received only by patterns with critical wavelength $\Lambda_c = \sqrt{4\lambda d}$ (self-focusing case) or $\Lambda_c = \sqrt{4\lambda d/3}$ (self-defocussing case), calculated by setting $\Theta = \pi/2$ for a self-focusing and $\Theta = 3\pi/2$ for a self-defocussing medium. A more formal way of stating this for a system with 2 transverse dimensions is to say the Fourier spectrum of patterns growing at the critical point will be localized on a ring with radius given by the critical wavenumber $q_c = 2\pi/\Lambda_c$. The symmetry of the patterns is based on wave mixing of waves with various wavevector $\mathbf{q}$ orientations inside the medium. A detailed treatment of this process can be found in the well known paper by D'Alessandro and Firth [65], and an outline is provided in the introductory chapter of this Thesis. An instability can also arise due to intensity modulated gratings [135, 136, 137, 138], which will be shown in the next Section when considering the modulations in the v variable.

5.1.2 Polarization instability

The existence and coupling between the atomic multipole moments via equations (2.19) is a novel element with respect to the work done on the $J = 1/2 \to J' = 1/2$ transition of hot sodium atoms [23]. However, as is indicated from the experimental results, the main driver of the instability is still the dipole term w. To see this, one needs to remember the two main ingredients for producing dispersive steady state patterns supported by spatially separated regions of σ^+ and σ^- light: a light polarization selective optical dispersion (i) and feedback (ii). Both of the requirements are satisfied for the w variable, as can seen from the form of the susceptibility (5.2) and was outlined for the $J = 1/2 \to J' = 1/2$ system in Ref. [133].

To show explicitly how the spin w drives the instability, one can first write a homogeneous (non-modulated) solution of the Eqs. (5.2) for fields $F_\pm$ exiting the atomic medium at point $z = L$

$$F_\pm = E^0_\pm e^{-i\xi\alpha L}\left[\cos(\eta\alpha L) \mp \frac{i}{\eta}\left(\frac{3}{4}w \pm \frac{3}{20}(u \mp iv)\right)\sin(\eta\alpha L)\right], \tag{5.12}$$

where

$$\xi = \left(1 + \frac{1}{20}x\right), \quad \eta = \sqrt{\left(\frac{3}{4}w\right)^2 + \left(\frac{3}{20}\right)^2 (u^2 + v^2)} \tag{5.13}$$

and $w,\ x,\ u,\ v$ are the solutions of Eqs. (2.15). The form of Eq. (5.12) is more involved than the simple solution for the $J = 1/2$ system, where only a phase shift is acquired for the field by transversing the medium (in the far-detuned limit). This is a consequence of the off diagonal terms in the equation (5.2), due to u and v variables.

A polarization instability cannot arise due to modulations in the u or x variables, as can be seen from the above equations (5.2, 5.12). This is trivially shown by observing that the response of the medium to modulations in these variables is equal for both $\sigma^{\pm}$ components, which in turn means that light polarization selective feedback, required for a polarization instability to form in the SFM configuration, is not possible.

Following the standard procedure of linear stability analysis [133] one can now set $w \to w_0 + \delta w,\ x \to x_0,\ u \to u_0$ and $v \to v_0 + \delta v$, where $w_0,\ x_0,\ u_0,\ v_0$ are the homogeneous solutions and $\delta w,\ \delta v$ are the perturbations. The resulting form of the variable η (Taylor expanded to the first order in the perturbations $\delta w,\ \delta v$) is

$$\eta \approx \eta_0 + \frac{1}{\eta_0}\left(\left(\frac{3}{4}\right)^2 w_0 \delta w + \left(\frac{3}{20}\right)^2 v_0 \delta v\right). \tag{5.14}$$

The Eq. (5.14) can be simplified by noting that for $B_z \approx 0$ (see Sec. 5.2.1) the terms $\left(\frac{3}{20}\right)^2 v_0 \delta v$ and $\left(\frac{3}{4}\right)^2 w_0 \delta w$ are $\ll \eta_0$ (due to the fact that the homogeneous solutions $w_0,\ v_0 \approx 0$), and thus the second term on the RHS can be neglected.

For a linear input polarization with $E_+^0 = E_-^0 = \sqrt{I_0}$ the fact that $w_0,\ v_0 \approx 0$ also implies $|F_+^0|^2 = |F_-^0|^2 = I_0$ and $|B_+^0|^2 = |B_-^0|^2 = RI_0$. The term multiplying the $\sin(\eta\alpha L)$ term in Eq. (5.12) now becomes

$$\frac{1}{\eta}\left(\frac{3}{4}w \pm \frac{3}{20}(u \mp iv)\right) \approx \frac{1}{\eta_0}\left(\frac{3}{4}\delta w - \frac{3}{20}(i\delta v \mp u_0)\right). \tag{5.15}$$

Due to $\eta_0 \alpha L,\ \xi_0 \alpha L \ll 1$, at the used parameters of $|\Delta| > 10\Gamma_2,\ b_0 \sim 30$, one can now set $\sin(\eta_0 \alpha L) \approx \eta_0 \alpha L,\ \cos(\eta_0 \alpha L) \approx 1,\ e^{-i\xi_0 \alpha L} \approx 1$.

Focusing first on a modulation in $\delta w(q)$ for a wavenumber q and using Eq. (5.10), one gets the form of the reflected field modulated by $\delta w(q)$ and entering the atomic equations of motion (2.15)

$$B_\pm = B_\pm^0 \left(1 \mp i \frac{3\alpha L}{4} e^{i\Theta(q)} \delta w(q)\right), \tag{5.16}$$

where the term $-i\frac{3}{20}u_0$ was neglected due to $\frac{3}{20}u_0 \ll 1$. The modulation δw can be chosen to be $\delta w = \varepsilon \sin(qx)$ where $\varepsilon \ll 1$. The positive feedback is achieved for the modulation with critical wavenumber $q = q_c$, for which the diffractive phase shift $\Theta(q_c)$ is such that it maximally reinforces the initial δw modulation. As was discussed in Ch. 2 the main driver of the spin w variable is the difference of pump rates $\mathcal{D} = P_+ - P_-$. This means that the diffractive phase shift $\Theta(q_c)$ is the one creating a modulation $\sim \sin(qx)$ of $\mathcal{D}$. The only field containing the feedback is $B_\pm$, so it is sufficient to limit the discussion to it. Now, for $\Omega_z \ll \Delta$, the prefactors of the pump rates $P_\pm$ are equal and the spin driving has the form

$$\mathcal{D} \sim |B_+|^2 - |B_-|^2 = 3RI_0\alpha\varepsilon \sin(qx)\sin(\Theta(q)). \tag{5.17}$$

The diffractive phase shift $\Theta(q)$ that reinforces the initial modulation $\delta w(q) = \epsilon \sin(qx)$ is thus seen to be equal to $\Theta(q_c) = \pi/2$, which is satisfied for the wavenumber $q_c = \sqrt{\pi k/2d}$ with period $\Lambda_c = \sqrt{4\lambda d}$. In case when the diffraction distance d is negative (made possible by the virtual feedback mirror [120]) so that $\Theta \to -\Theta$, the diffractive phase shift is equal to $\Theta(q_c') = 3\pi/2$, with $q_c' = \sqrt{3k\pi/2d}$ and $\Lambda_c' = \sqrt{4\lambda d/3}$. The field reentering the medium for $d > 0$ is then

$$B_\pm = B_\pm^0 \left(1 \pm \frac{3\alpha L}{4} \varepsilon \sin(q_c x)\right), \tag{5.18}$$

and for $d < 0$ the field is of the same form but with substition $q_c \to q_c'$. It is useful to see the feedback to the other variables from the fields of the form (5.18). The variables $x,\ u,\ v$ are driven by $\mathcal{S} \sim |B_+|^2 + |B_-|^2$, $P_{\Lambda+} \sim B_+^* B_- + B_+ B_-^*$ and

$P_{\Lambda -} \sim i(B_+^* B_- - B_+ B_-^*)$, respectively. For the $d > 0$ case the driving terms for the atomic variables are

$$\begin{aligned}
&\mathcal{D} \sim 3\alpha L R I_0 \epsilon \sin(q_c x) \\
&\mathcal{S} \sim 2RI_0 \left(1 + \left(\tfrac{3\alpha L}{4}\right)^2 \epsilon^2 \sin^2(q_c x)\right) \\
&P_{\Lambda +} \sim 2\mathrm{Re}(B_+^{0*} B_-^0) \left(1 - \left(\tfrac{3\alpha L}{4}\right)^2 \epsilon^2 \sin^2(q_c x)\right) \\
&P_{\Lambda -} \sim -2\mathrm{Im}(B_+^{0*} B_-^0) \left(1 - \left(\tfrac{3\alpha L}{4}\right)^2 \epsilon^2 \sin^2(q_c x)\right)
\end{aligned} \tag{5.19}$$

and again the same results are found for $d < 0$ with substitution $q_c \to q_c'$. The amplitudes of $P_{\Lambda +}$ and $P_{\Lambda -}$, $\mathrm{Re}(B_+^{0*} B_-^0)$ and $\mathrm{Im}(B_+^{0*} B_-^0)$, can be calculated from Eq. (5.18) to be equal to

$$\begin{aligned}
\mathrm{Re}(B_+^{0*} B_-^0) &= R I_0 \cos\left(\tfrac{3\alpha L}{10} u_0\right) \\
\mathrm{Im}(B_+^{0*} B_-^0) &= -R I_0 \sin\left(\tfrac{3\alpha L}{10} u_0\right),
\end{aligned} \tag{5.20}$$

where as in the previous results w_0, $v_0 \approx 0$. Solutions (5.20) show that the modulation of $P_{\Lambda -}$ will be small compared to the modulations of the other driving terms, as $\frac{3\alpha L}{10} u_0 \ll 1$, and consequently the modulation in v will be weaker. This is confirmed by the simulation results.

In the above calculations it was approximated, as is motivated by the experimental results, that spin w is the sole driver of the polarization instability. A polarization instability can however also arise due to the v variable, and repeating the above analysis for the v variable shows a differend kind of polarization patterns to arise. Setting now $\delta v = \varepsilon \sin(qx)$ and neglecting δw (also assuming all the approximations used in deriving 5.18) in Eq. (5.15), one gets for the modulated backwards propagating field

$$B_\pm = B_\pm^0 \left(1 \mp \frac{3\alpha L}{20} e^{i\Theta(q)} \delta v(q)\right). \tag{5.21}$$

As the v variable is now driven as $\delta \dot{v} \propto -P_{\Lambda -}$, the feedback is given by $-P_{\Lambda -}$. Inserting (5.21) into the relation for $P_{\Lambda -}$ now gives

$$-P_{\Lambda -} \propto 2\mathrm{Im}(B_+^* B_-) \approx \frac{6\alpha L}{5} \mathrm{Re}(B_+^{0*} B_-^0) \varepsilon \sin(qx) \sin(\Theta(q)), \tag{5.22}$$

where now the term $2\mathrm{Im}(B_+^{0*}B_-^0)$ is neglected as explained in the discussion of Eq. (5.20). As for the δw case, the maximum feedback is received for $\Theta(q_c) = \pi/2$ ($d > 0$), however the field reflecting back to the end of the medium is now equal to

$$B_\pm = B_\pm \left(1 \mp i\frac{3\alpha L}{20}\varepsilon \sin(q_c x)\right), \tag{5.23}$$

which is phase modulated, as opposed to the amplitude modulated field in Eq. (5.18). This results in a completely umodulated $\mathcal{D}$, which further gives a negligible modulation in w, arising solely due to coupling to the v via the dynamical equations (2.15).

The experimental results, where a high modulation in the $\mathcal{D}$ driving term is present, indicate that the driver of the instability is the w variable. This is anticipated by inspecting Eq. (5.2), where the prefactor of the w variable is 5 times greater than the prefactor of the v variable. The results of experiments reported in Ref. [139], where patterns with a modulation in the far field of the orthogonal linear polarization channel, but without a near field modulation in the circular polarization channels, was reported for high transverse B-fields, in a cloud with $b_0 = 80$. It is likely that these modulations were driven by v, and are not seen for small transverse B-fields as w variable dominates in this case. The threshold of these patterns is likely to be too high to be observed in the setup described in this Thesis, with the available optical thickness of $b_0 \approx 27$.

5.2 One dimensional model

The code for 1D simulations is based on solving the dynamical equations coupled to the equations of light-atom interaction and free space diffraction. The code solves numerically the dynamical equations of the atomic medium (2.19) and couples them with the solutions for forward and the backward fields calculated from the propagation equation (5.6). The equations are solved for each point in the real space, discretized to 128 (×128 for the 2D case) points. To simulate the noise in the atomic cloud a small background noise term was added to the optical equations, as a necessary condition for patterns to appear spontaneously above input intensity threshold. In addition to this, a low pass filter is applied to electric field modulations in the Fourier space with a radius of $1.5\times$ the critical value q_c. Experimentally, the Fourier filtering occurs as a consequence of “thick medium” effects, described in Ch. 6 and Ref. [125], i.e. mainly diffraction in the optical medium. The Fortran codes for both 1D and 2D cases were written by Gordon Robb. The 1D simulation results were produced by the author, while the 2D simulation results were done by Gordon Robb. Details on the numerical methods are presented in the Thesis of Enrico Tesio [38].

5.2.1 Steady state patterns

At zero B-fields, the interaction between the atomic variables is mediated solely by the driving terms $\mathcal{D}$, $\mathcal{S}$, $P_{\Lambda+}$, $P_{\Lambda-}$. Noting the form of Eqs. (2.19), this means the dipole moments y_1, y_2, z_1, z_2 can be neglected, as they are not coupling directly to the light, nor to the remaining atomic variables. The relevant dynamical equations for describing the system are then given by Eqs. (2.15). Fig. 5.1 shows typical steady state patterns for $B_z = 0$. The solutions for the atomic variable modulations are plotted alongside the solutions for their respective driving terms.

The modulation period of x and u has half the period of w modulation, which is in direct agreement with (5.19). The x and u modulations are also shifted by half a period relative to each other. The periodicity of v is mainly equal to the one of w, with a small peak at the second harmonic, and an amplitude that is nearly two orders of magnitude smaller than the w modulation amplitude, meaning the effect causing the shift from periodicity predicted in (5.19) is small. The depth of modulation in w is ~ 0.8, nearly an order of magnitude higher than modulations in x and u, which is in line with the interpretation that w is the main driver of instability.

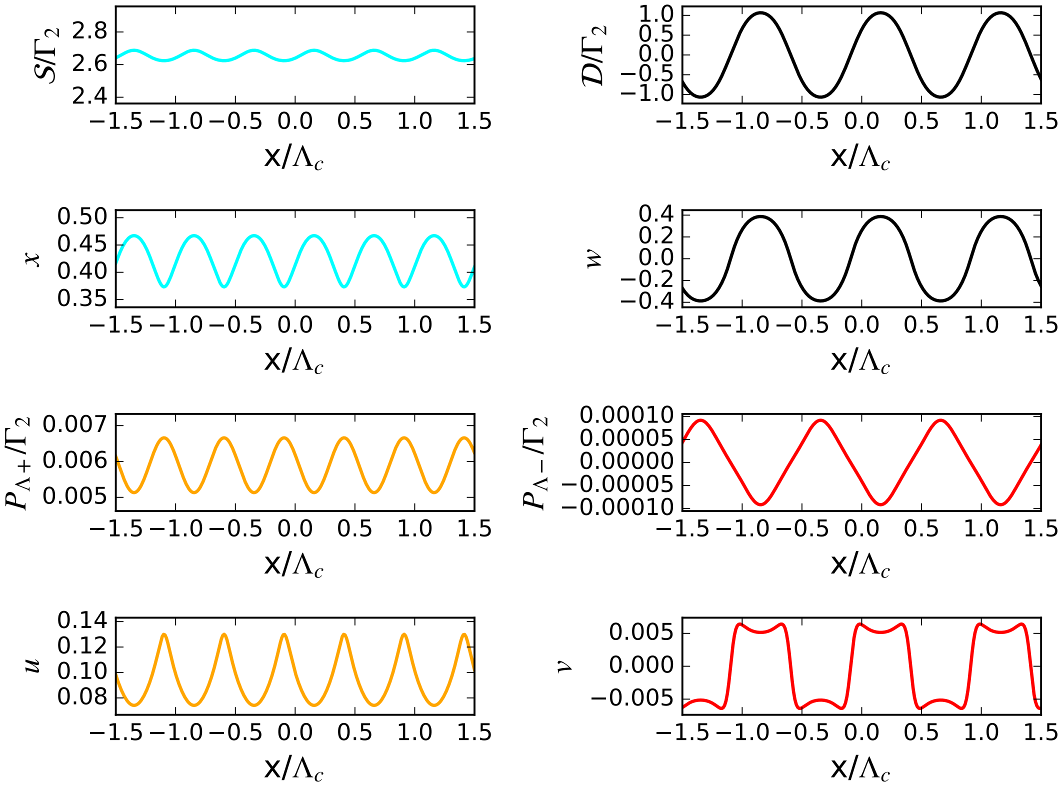

FIGURE 5.1: Steady state solutions for the atomic variables and their driving terms at zero B-fields. Simulation parameters: $b_0 = 25$, $I_\pm = 7.5 I_s$, $\Delta = -14\Gamma_2$, $r = 0.001\,\Gamma_2$, $B_x = B_y = B_z = 0$.

Fig. 5.2 shows the patterns for a B_z field of 40 mG. The most notable difference from the case with $B_z = 0$ are the asymmetries in the peak heights of x, u and v modulations for peaks separated by $\Lambda_c/2$. The asymmetry is a result of the coupling of the spin with the quadrupolar atomic moments by Ω_z and the driving terms, via the dynamical equations.

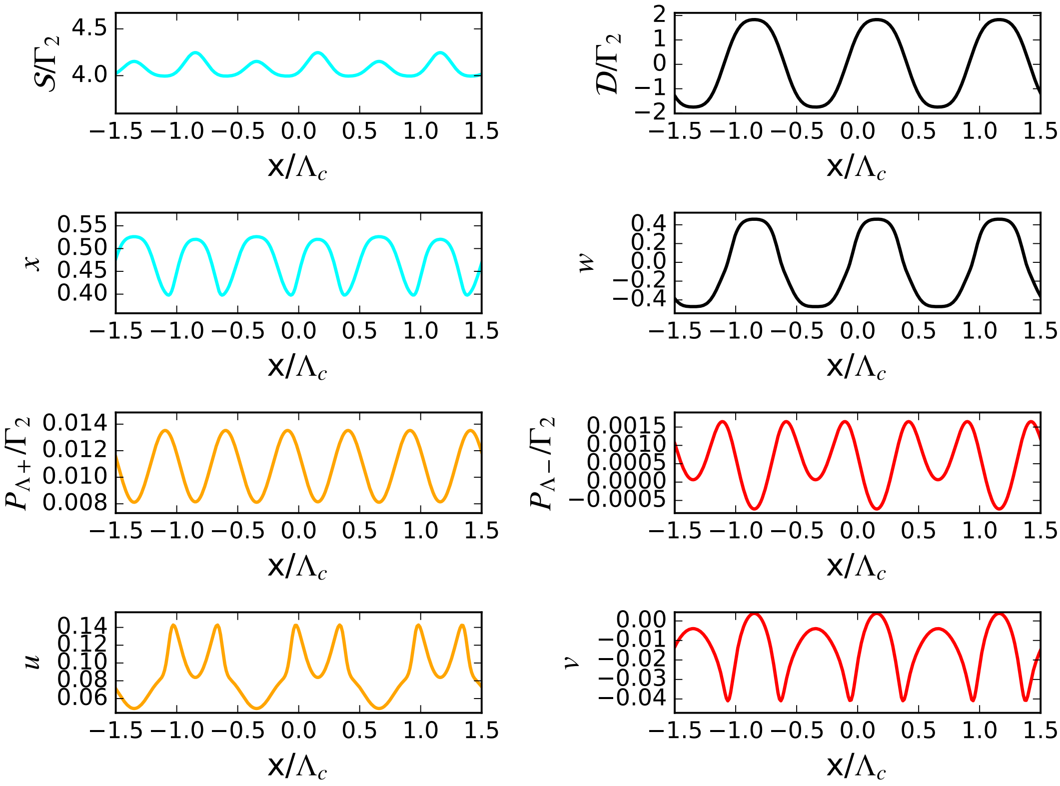

FIGURE 5.2: Steady state solutions for the atomic variables and their driving terms for moderate longitudinal B-field. Simulation parameters: $b_0 = 25$, $I_\pm = 12I_s$, $\Delta = -12\Gamma_2$, $r = 0.001\ \Gamma_2$, $B_x = B_y = 0$, $B_z = 40$ mG.

The asymmetry is the most likely cause of the asymmetry in the diffracted powers of the σ^+ and σ^- light shown in Fig. 5.3. This is so due to the fact that the Eq. (5.18) describes the backwards propagating field only in the linear growth regime [59], and the steady state backwards propagating field is dependent on all of the atomic variables, which are coupled dynamically by light traversing the cloud and reflecting from the feedback mirror. This dynamical coupling can then cause the other variables to couple to w and generate asymmetries of diffracted power.

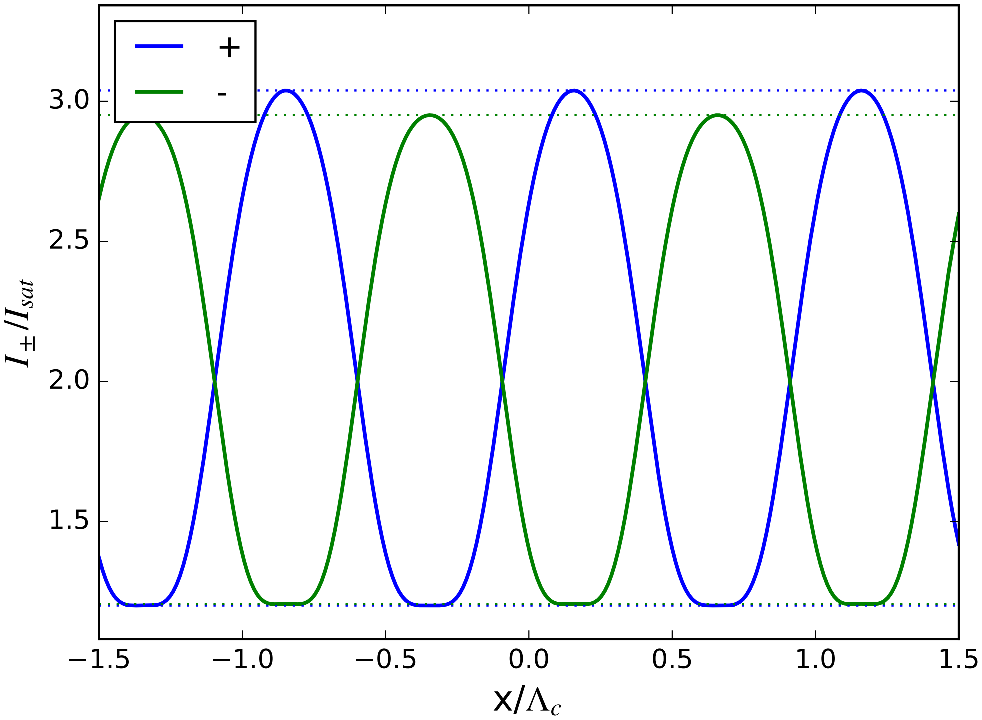

FIGURE 5.3: Total steady state beam intensities at $z = L$ for $\sigma^\pm$ light. Simulation parameters are same as in Fig. 5.2.

5.2.2 Longitudinal B-field scan

The longitudinal field scans for the field parallel to the input beam direction is shown in Fig. 5.4. The sum of diffracted powers in the two circular channels is plotted for the intensities $I_\pm = 12\ I_{sat}$ and $I_\pm = 20\ I_{sat}$. An asymmetry in modulation depth (proportional to the diffracted power) of the $\sigma^\pm$ components is seen to occur for $0 < |B_z| < 60$ mG for $I_\pm = 12\ I_{sat}$ and $0 < |B_z| < 120$ mG for $I_\pm = 20\ I_{sat}$. The width of the pattern existence region is seen to increase with the input pump intensity, as is seen in the experimental results of Chapter 4. An abrupt decay of diffracted power occurs for higher B_z fields, followed by a revival of the modulation, which is also seen in the experiments. The details of the mechanisms of the asymmetry of $\sigma^\pm$ modulations and the revival of pattern contrast are both under investigation.

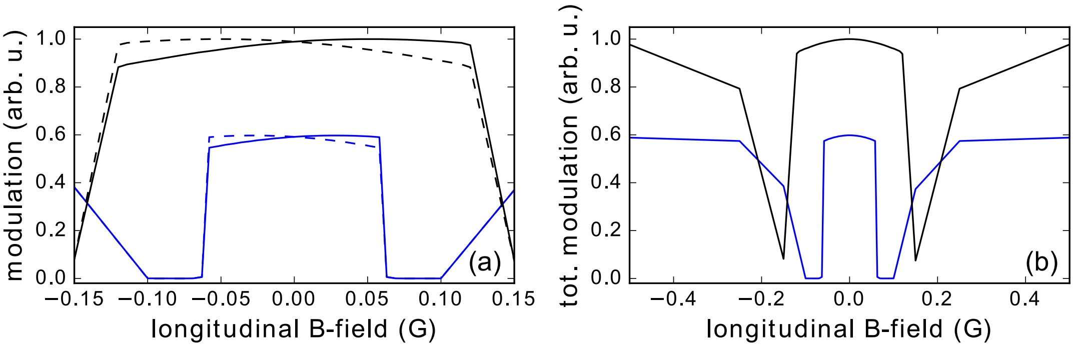

FIGURE 5.4: Scan of the longitudinal B-field. Modulation depth of (a) σ^+ light (solid lines) and σ^- light (dashed lines), (b) total light. Blue: $I_\pm = 12\ I_{sat}$. Black: $I = 20\ I_{sat}$. Simulation parameters: $t = 86\ \mu$s, $b_0 = 25$, $\Delta = -10\ \Gamma_2$, $r = 0.001\ \Gamma_2$, $B_{x,y} = 0$.

5.2.3 Transverse B-field scans

The transverse field scans for the fields parallel and orthogonal to the input beam polarization are shown in Fig. 5.5. The sum of diffracted powers in the two circular channels is plotted for the intensities $I_\pm = 12\ I_{sat}$ and $I_\pm = 20\ I_{sat}$. The instability is seen to decay completely for parallel fields > 100 mG at $I_\pm = 12\ I_{sat}$ and > 150 mG at $I_\pm = 20\ I_{sat}$. The orthogonal fields work to reduce the contrast of patterns and for strong enough values completely preclude the pattern formation. The reason for decay of contrast with transverse fields is the depumping of the orientation w which is the main cause of the instability. With beam intensities higher above threshold it is therefore possible to achieve pattern formation for stronger transverse fields. The shape of the parallel B-field scan curve agrees with the experimental result shown in Fig. 4.11. The shape of the orthogonal scan curve is however slightly different than the experimental one. The reason for this slight discrepancy is currently still unknown.

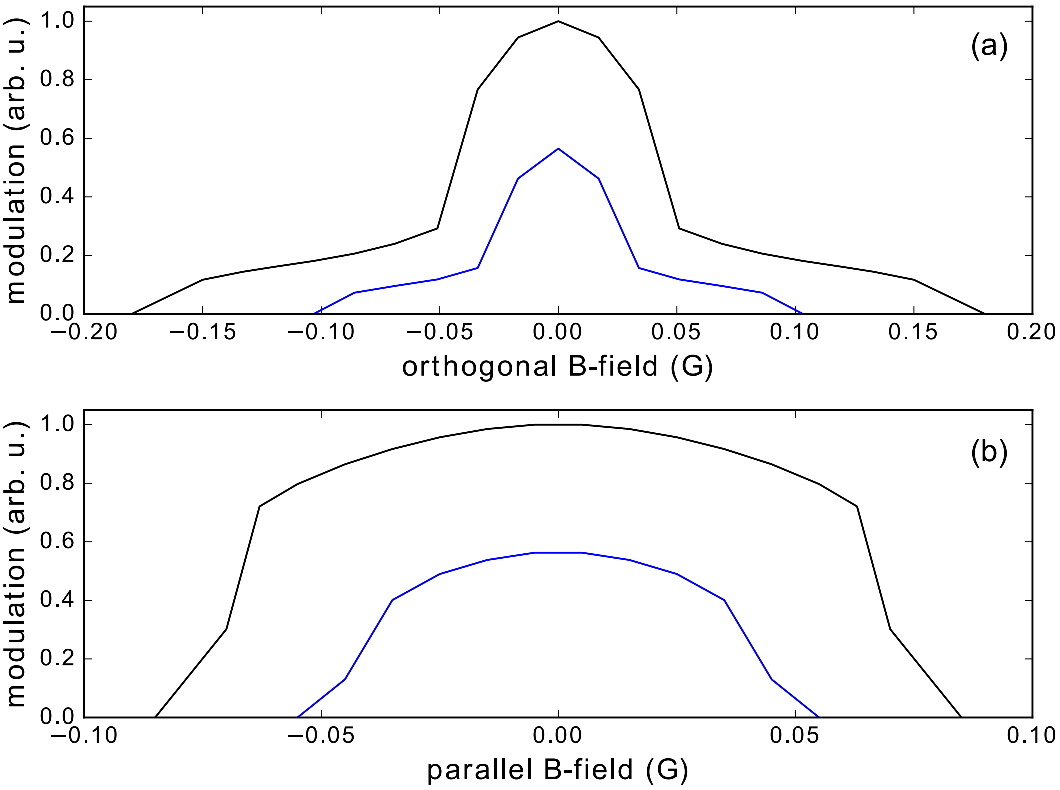

FIGURE 5.5: Scan of the B-fields parallel and orthogonal to the input beam polarization. Blue: $I_{\pm} = 12\ I_{sat}$. Black: $I_{\pm} = 20\ I_{sat}$. Simulation parameters: $t = 86\ \mu\text{s}$, $b_0 = 25$, $\Delta = -12\ \Gamma_2$, $r = 0.001\ \Gamma_2$, $B_z = 0$.

5.3 Two dimensional model

5.3.1 Pattern symmetries

The two dimensional simulations use a grid with 128×128 grid points. Figures 5.6 and 5.7 depict the typical pattern realizations for zero and finite B_z, respectively. The square patterns with complementary peaks of $\sigma^{\pm}$ light appear at zero B_z field. The periodicity in the atomic variables mirrors the 1D results shown in Sec. 5.2.1. The spin variable w, driven by the difference in the pump rates of $\sigma^{\pm}$ light, has positive peaks (red) at regions of excess σ^{+} and negative peaks (blue) at regions of excess σ^{-} light. The x and u variables have half the periodicity of the spin w, while the v variable has the same periodicity. The modulation depth is again highest for the w variable ($\Delta w \approx 1.2$), almost an order of magnitude greater than the modulation for x ($\Delta x \approx 0.2$) and u ($\Delta u \approx 0.1$), while the v variable has the smallest modulation depth ($\Delta v \approx 0.01$).

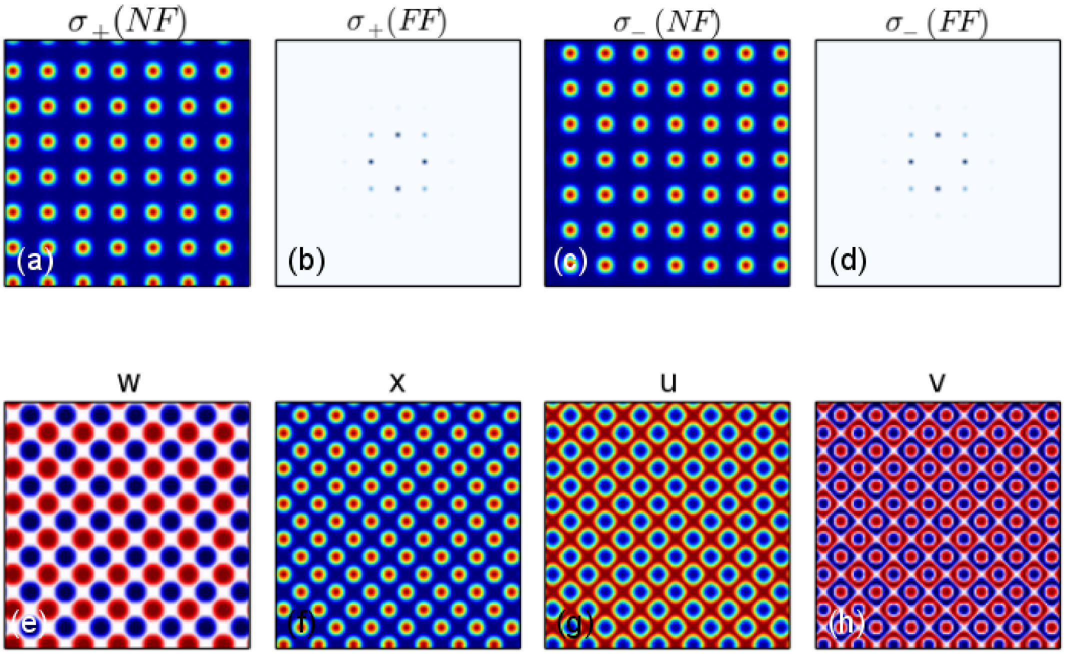

FIGURE 5.6: Square patterns for zero applied B_z field. (a) near field (NF) of σ^+ polarization, (b) far-field (FF) of σ^+ polarization, (c) NF of σ^- polarization, (d) FF of σ^- polarization, (e) atomic spin variable w, (f) alignment x, (g) real part of Δm=2 coherence u, (h) imaginary part of Δm=2 coherence v. Simulation parameters: $b_0 = 35$, $\Delta = -8\,\Gamma_2$, $B_z = 0$.

For hexagons, the positive (HX^+) phase appears in the σ^+ channel and the negative (HX^-) phase in the σ^- channel, at $B_z > 0$. The w, x and v variables have positive peaks at positive peaks of σ^+ light, while the u variable has negative peaks at these regions. The modulation depth for the w variable is $\Delta w \approx 1$, while the other variables have: $\Delta x \approx 0.24$, $\Delta u \approx 0.2$, $\Delta v \approx 0.1$. The modulation in w is thus still the strongest.

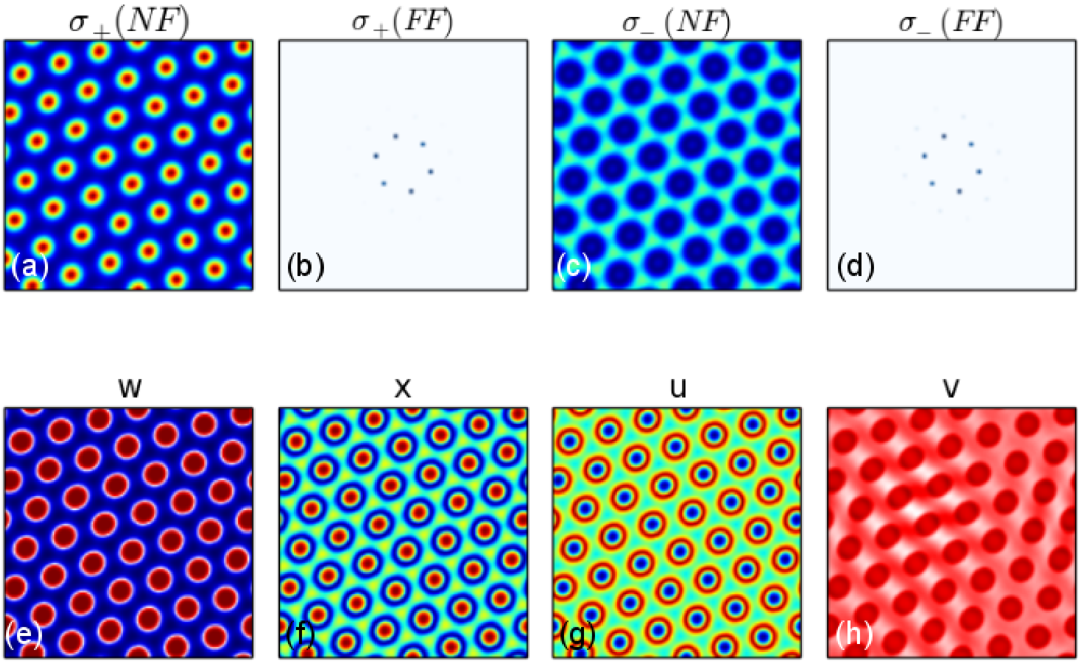

FIGURE 5.7: Hexagonal patterns for finite applied B_z field. Image ordering same as in Fig. 5.6. Simulation parameters: $b_0 = 35$, $\Delta = -15.6\ \Gamma_2$, $B_z = 25$ mG.

5.3.2 Spin magnetization

The interpretation of $B_z = 0$ patterns as spin antiferromagnetic and $B_z \neq 0$ patterns as ferrimagnetic can be illustrated by looking at 1D cuts along the lines of the peaks in 2D space.

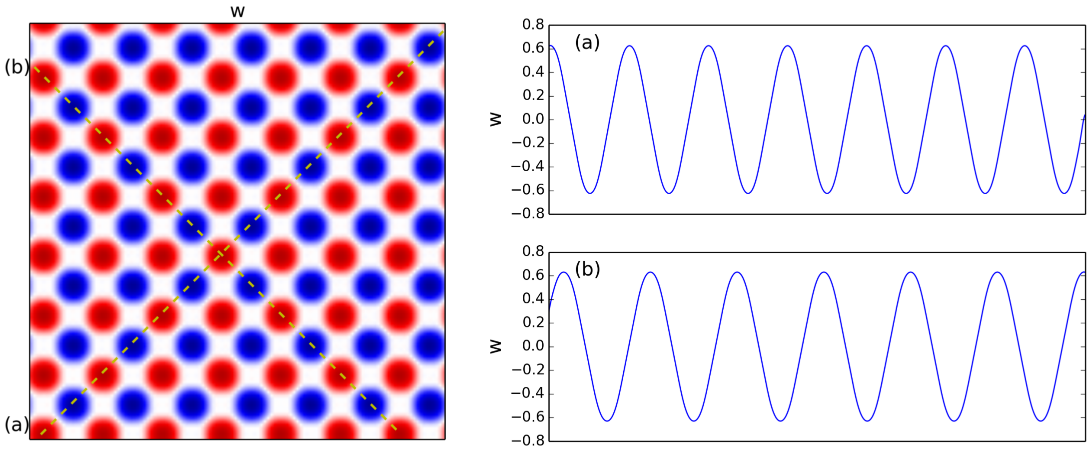

Figure 5.8: Dipole w magnetization peaks for square patterns (left) and 1D cuts along dashed lines (right). Simulation parameters are same as in Fig. 5.6.

Figure 5.8 shows the 1D cuts of the spin w variable along two orthogonal directions for a square pattern realization. The neighbouring spin w amplitudes are symmetric around $w = 0$, with the spins pointing in the opposite directions, indicating that the total magnetization in this phase is zero, as is expected from antiferromagnetic spin ordering.

Figure 5.9 shows the 1D cuts of the spin w variable for a hexagonal pattern realization. The neighbouring spin w amplitudes are now not symmetric around $w = 0$, with the upwards pointing sublattice having a higher amplitude than the downwards pointing lattice, for an external magnetic field of $B_z = 25$ mG. The magnetic ordering of the patterns is now ferrimagnetic, as the net magnetization is non-zero and the neighboring spins are pointing in the opposite directions.

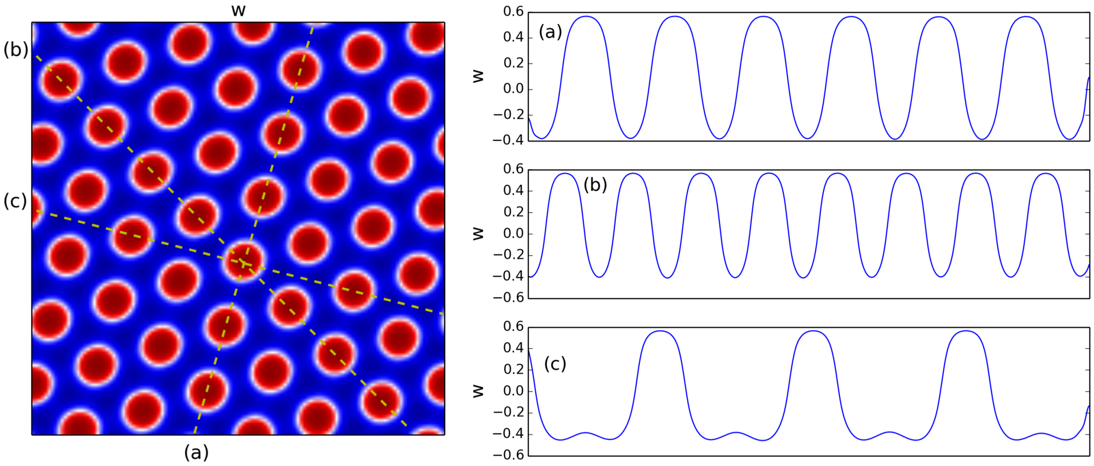

FIGURE 5.9: Dipole w magnetization peaks for hexagonal patterns (left) and 1D cuts along dashed lines (right). Simulation parameters are same as in Fig. 5.7.

5.4 Summary

In this Chapter, the simulation results of the SFM were presented. In the first part of the Chapter it is shown by arguments of linear stability analysis how the polarization instability observed in the experiments is driven by the spin w variable. It is also calculated how a polarization instability can in the $J = 1$ system be driven by the v variable, which is a plausible mechanism underlying the observations reported in Ref. [139] at high transverse B-fields. In the second part of the Chapter the results of 1D and 2D simulations are presented. The 1D longitudinal B-field scans reveal an imbalance between the diffracted power in the two circular polarization channels for small applied B-fields. The 2D simulations reveal a presence of antiferromagnetic ordering for zero longitudinal B-field, and a ferrimagnetic ordering for a finite longitudinal B-field. The simulation results agree with the experimental observations reported in Ch. 4.

Chapter 6

Thick medium effects

For pattern formation in the SFM configuration, the questions about the occurence of longitudinal gratings and the finite diffraction inside the optical medium, the so called *thick medium* effects, have up to now been discussed only partially. The cold atoms constitute a convenient platform for studying *thick medium* effects for various types of optical non-linearities. As was shown in the experiments with optomechanical and two-level non-linearities in clouds with high optical thickness of $b_0 \approx 200$ [18, 19], to correctly account for both the lengthscale and threshold dependence on the mirror distance, one needs to include the diffraction and longitudinal gratings into the description. For this reason a model was developed, taking into account the said phenomena, and explaining their consequences [125]. The model is outlined in this Chapter, and its predictions, in the Kerr limit, shown to agree well with the results of the experiments in a cold atomic medium using the Zeeman non-linearity. The model was developed by William J. Firth, and the details are published in Ref. [125].

6.1 Theoretical model

6.1.1 Beam propagation through the medium

Restricting to the scalar (single light polarization mode) case, the electric field is given by $E/\sqrt{I_s} = Ae^{ikz} + Be^{-ikz}$, where z is the propagation direction, I_s the saturation intensity and A, B are the forward and backward propagating fields. Maxwell's equations for propagation of electromagnetic waves in the medium are

$$\begin{cases} \frac{\partial A}{\partial z} - \frac{i}{2k}\nabla_\perp^2 A = i\frac{k}{2}\chi_{NL}A, \\ \\ \frac{\partial B}{\partial z} + \frac{i}{2k}\nabla_\perp^2 B = -i\frac{k}{2}\chi_{NL}B. \end{cases} \tag{6.1}$$

Nonlinear susceptibility χ_{NL} of the two-level medium is given by

$$\chi_{NL} = -\frac{6\pi}{k_0^3}n_a\frac{\bar{\Delta}}{1+\bar{\Delta}^2}\frac{1}{1+I/I_s} = \chi_l\frac{1}{1+I/I_s}, \tag{6.2}$$

where n_a is the atomic density, $I = |E|^2$, $\bar{\Delta} = 2\delta/\Gamma$ (δ is the beam detuning, $\Gamma \equiv \Gamma_1$ is the transition linewidth) and absorption is neglected due to $|\Delta| \gg 1$. Writing $A = ae^{i\theta_A}$, $B = be^{i\theta_B}$, it can easily be shown that

$$\frac{1}{1+\frac{I}{I_s}} = \frac{1}{1+a^2+b^2+hab(e^{2ik}e_+ + e^{-2ik}e_+^*)}, \tag{6.3}$$

where h is the grating parameter, and $e_+ = e^{i(\theta_A-\theta_B)}$. The grating parameter h has been introduced as in [140] to account for washing out of reflection grating due to atomic and mirror motion. In principle, any value between 0 and 1 can be used for h as wash-out of coherence of A and B can be partial, and it will later be shown $h = 1$ gives a better match with experimental data than $h = 0$. If we now introduce a coupling parameter $r = hab/(1+a^2+b^2)$, the part of expression (6.3) containing r can be Taylor expanded in re_+ as

$$\frac{1}{1+r(e^{2ik}e_+ + e^{-2ik}e_+^*)} = (1+2r^2+6r^4+...)-(e^{2ik}e^{i(\theta_A-\theta_B)}+e^{-2ik}e^{-i(\theta_A-\theta_B)})(r+3r^3+10r^5+...), \tag{6.4}$$

where higher order terms in e^{2ik} were dropped as they do not lead to phase matched couplings [125]. Inserting the above expression into (6.1) gives

$$\begin{cases} \frac{\partial A}{\partial z} - \frac{i}{2k}\nabla_\perp^2 A = i\frac{k}{2}\chi_l A(\frac{(1+2r^2+\ldots)-(br/a)(1+3r^2+\ldots)}{1+a^2+b^2}), \\ \\ \frac{\partial B}{\partial z} + \frac{i}{2k}\nabla_\perp^2 B = -i\frac{k}{2}\chi_l B(\frac{(1+2r^2+\ldots)-(ar/b)(1+3r^2+\ldots)}{1+a^2+b^2}). \end{cases} \tag{6.5}$$

The first term in both equations is responsible for saturation and the second for cross-coupling between the forward and backward propagating beams. To the lowest order in light intensity, the numerator in equation for A is $1+a^2+(1+h)b^2$, while for B it gives $1+(1+h)a^2+b^2$. This means the full grating case ($h=1$) increases the cross-couplings by a factor of 2 [125].

To prepare the investigation of transverse perturbations in the following Section, one can write the propagation equations (6.5) in the form

$$\begin{cases} \frac{\partial A}{\partial z} - \frac{i}{2k}\nabla_\perp^2 A = -\frac{\alpha_l}{2}(1+i\bar{\Delta})F(a^2,b^2)A, \\ \\ \frac{\partial B}{\partial z} + \frac{i}{2k}\nabla_\perp^2 B = \frac{\alpha_l}{2}(1+i\bar{\Delta})F(b^2,a^2)B, \end{cases} \tag{6.6}$$

where α_l is the linear absorption coefficient, and the function F describes the nonlinearity of the atomic susceptibility, as modelled by e.g. (6.5).

6.1.2 Transverse perturbations in the quasi-Kerr limit

The linear absorption coefficient can be written as $\alpha_l = \alpha_0/(1+\bar{\Delta}^2)$, where α_0 is the on-resonance absorption. Formally, in a quasi-Kerr model, one assumes that $|\bar{\Delta}|$ is large enough that $\alpha_l L$ can be neglected, but with $\alpha_l\bar{\Delta}L$ finite, so that the nonlinearity is purely refractive. This is justified in the experiments reported in this Thesis, where $\alpha_0 L$ ($= b_0$) is on the order of 30, and the detuning is on the order of $|\bar{\Delta}| \sim 14$.

In the linear stability analysis, one supposes that the solution of the diffractionless form of the equation (6.6) (the zero order mode), subject to the appropriate boundary conditions, is known, and considers transverse perturbations of the form $A = A_0(1+f)$, $B = B_0(1+g)$, where $\nabla_\perp^2(f,g) = -Q^2(f,g)$, i.e. the transverse perturbation has a wavenumber Q, corresponding to a diffraction angle Q/k in the far field. Assuming now $|f|, |g| << 1$, one can obtain the linearized propagation equations:

$$\begin{cases} \frac{df}{dz} = -i\theta f - i\alpha_l L\bar{\Delta}(F_{11}f' + F_{12}g'), \\ \frac{dg}{dz} = i\theta g + i\alpha_l L\bar{\Delta}(F_{21}f' + F_{22}g'). \end{cases} \tag{6.7}$$

Here L is the length of the medium, $\theta = Q^2L/2k$, $f = f' + if''$, $g = g' + ig''$, and the real quantities F_{ij} are defined as $F_{11} = p\frac{\partial F(p,q)}{\partial p}$, $F_{12} = q\frac{\partial F(p,q)}{\partial q}$, $F_{21} = p\frac{\partial F(q,p)}{\partial p}$, $F_{22} = q\frac{\partial F(q,p)}{\partial q}$ (where $p = |A|^2$, $q = |B|^2$). In the above it was assumed that the fields are time-independent, which is adequate to calculate the threshold of a zero-frequency pattern-forming (Turing) instability at wavevector Q. To find the Hopf instabilities, or to properly account for dynamical behavior of the field-atom system, one would have to start from the Maxwell-Bloch equations, rather than the susceptibility model.

The matrix elements $F_{i,j}$ can in the quasi-Kerr limit be calculated to be

$$\hat{F}_{kerr} = -\begin{pmatrix} p & (1+h)q \\ (1+h)p & q \end{pmatrix}. \tag{6.8}$$

where the parameters p and q are independent of the longitudinal coordinate z in the quasi-Kerr approximation [125].

The equations of propagation through the medium are related to the diffraction equations, describing the beam propagation from the medium and back, via boundary conditions on the perturbations $g(1)$, $f(1)$ at the end of the medium. Here, a normalized mirror distance D is used, defined as $D = (d - L/2)/L$, where d is the mirror distance from the center of the cloud and L is the medium length. The boundary conditions read $g(1) = e^{-2\psi_D}f(1)$, where $\psi_D = D\theta$, which leads to the SFM threshold condition for perfect mirror reflection ($R = 1$) [125]

$$c_1c_2 + \left(\frac{\psi_2}{\psi_1}c_D^2 + \frac{\psi_1}{\psi_2}s_D^2\right)s_1s_2 = c_Ds_D\left(\beta_1s_1c_2 - \beta_2s_2c_1\right), \tag{6.9}$$

where $\psi_{1,2}^2 = \theta(\theta + \kappa\phi_{1,2})$, $\kappa = \alpha_l L\bar{\Delta}$, (ϕ_1, ϕ_2) are the eigenvalues of $\hat{F}_{Kerr}$, $c_i = cos\psi_i$, $s_i = sin\psi_i$, $c_D = cos\psi_D$, $s_D = sin\psi_D$, and $\beta_n = \left(\frac{\psi_n}{\theta} - \frac{\theta}{\psi_n}\right)$. Solving the threshold condition equation (6.9) will lead to the threshold curves shown in the next Section. The equation can also be used to calculate the *envelope curve* [125], which is a crucial element determining the Talbot radius of the lowest threshold mode.

6.1.3 Calculating the thresholds

The threshold intensities for the pattern formation at a critical wavenumber Q can now be calculated from Eq. (6.9). Figure 6.1 shows the threshold curves for mirror distances $D = 1$ (orange) and $D = 2$ (green), where competition between lengthscales is seen to be mediated by the envelope curve (blue, dashed). At $D = 1$, the first Talbot ring (defined by the lowest Q where the threshold touches the envelope curve) is closer to the minimum threshold allowed by the envelope curve, at point ($I \approx 0.22$, $\theta \approx 1.2$), than the second Talbot ring. This means that the first Talbot ring has a lower threshold than the second, and will have a higher diffracted power at a fixed input beam intensity, as long as this intensity is not too high above threshold intensity. At $D = 2$, the situation is reversed, as both first and the second Talbot rings move towards left, and the second ring moves closer to the bottom of the envelope curve. This is a consequence of a more general principle, where increasing the mirror distance D increases the number of "wiggles" of the threshold curve. This in turn increases the possibility to get near the minimum of the envelope, and the system can get closer to the lowest possible threshold.

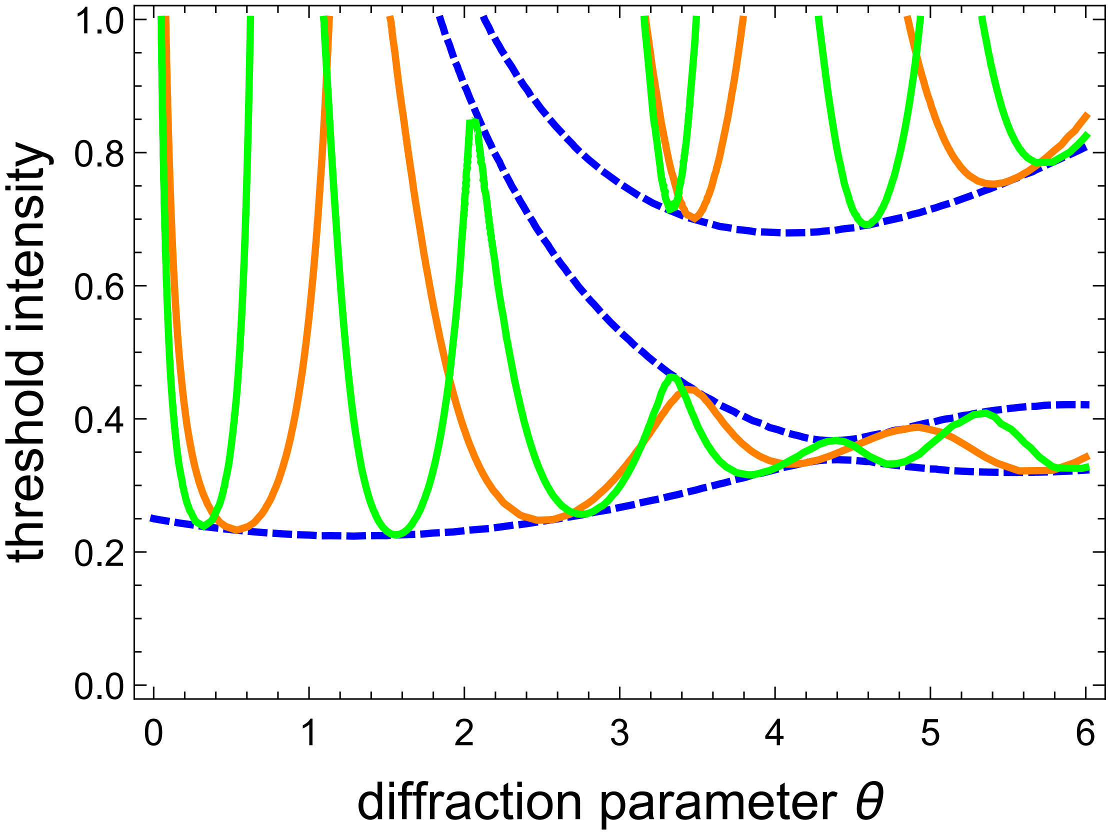

FIGURE 6.1: Threshold intensity (in units of $\alpha_l L\bar{\Delta}p/2$) vs diffraction parameter $\theta = Q^2L/2k$ for a Kerr medium with $h = 1$. Blue dashed curves: Envelope curves. Orange solid curves: $D = 1.0$. Green solid curves (with more wiggles): $D = 2.0$. In both cases the threshold curves touch the envelope curves, and are confined by them.

6.2 Experimental results

Figure 6.2 shows the variation of predicted threshold intensity (normalized as in Fig. 6.1), diffracted power (in general proportional to the inverse of the threshold intensity) and pattern lengthscale Λ with the scaled mirror distance $D = (d - L/2)/L$, where d is the distance from the cloud center and $L = 3.2$ mm is the effective medium thickness, taken to be equal to the FWHM of the cloud. For a mirror position near cloud center ($-1.2 < D < 0.6$) the threshold increases and no patterns are seen at the input beam intensity used. For higher mirror distances ($-2.5 < D < -1.2$ and $0.3 < D < 0.5$), a regime where the first Talbot ring is dominant is seen. This corresponds to the "thin medium" limit and is also the region where the pattern experiments in Chapter 4 are performed, as in this regime they can be compared to the theory of Chapters 2 and 5. For the mirror distances $-4.0 < D < -2.5$ and $0.5 < D < 2.4$, the second Talbot ring dominates at the fixed input intensity. The extinction of the power in the first Talbot ring with respect to the power in the second Talbot ring down to a factor of 3×10^{-3} is seen.

The solid lines represent the data calculated from Eq. (6.9) with $h = 1$ for the first (red) and second Talbot rings (blue). The mirror distance for which the second Talbot ring "overtakes" the first one can be read off from Fig. 6.2a as the point where the red threshold curve goes above the blue threshold curve. The experimental signature of this at the fixed input beam intensity is considered to be the point where the diffracted power in the second Talbot ring becomes higher than the diffracted power in the first Talbot ring (as shown in Fig. 6.2b). The two are in reasonably good agreement, with an error of around L for both the $D < 0$ and $D > 0$ cases.

The lengthscale dependence on mirror distance is depicted in 6.2c. The thick medium curve (red) coincides with the thin medium curve (black) for mirror distances $D < -1.4$ and $D > 0$, indicating that the thick medium framework is not necessary for predicting the lengthscale behavior. However, the necessity of the thick medium description becomes apparent when observing the occurrence of the second Talbot ring, which in cold atoms can not be explained from the thin medium considerations. The agreement of the lengthscale curves with the data is good, especially considering that there are no free parameters in this model.

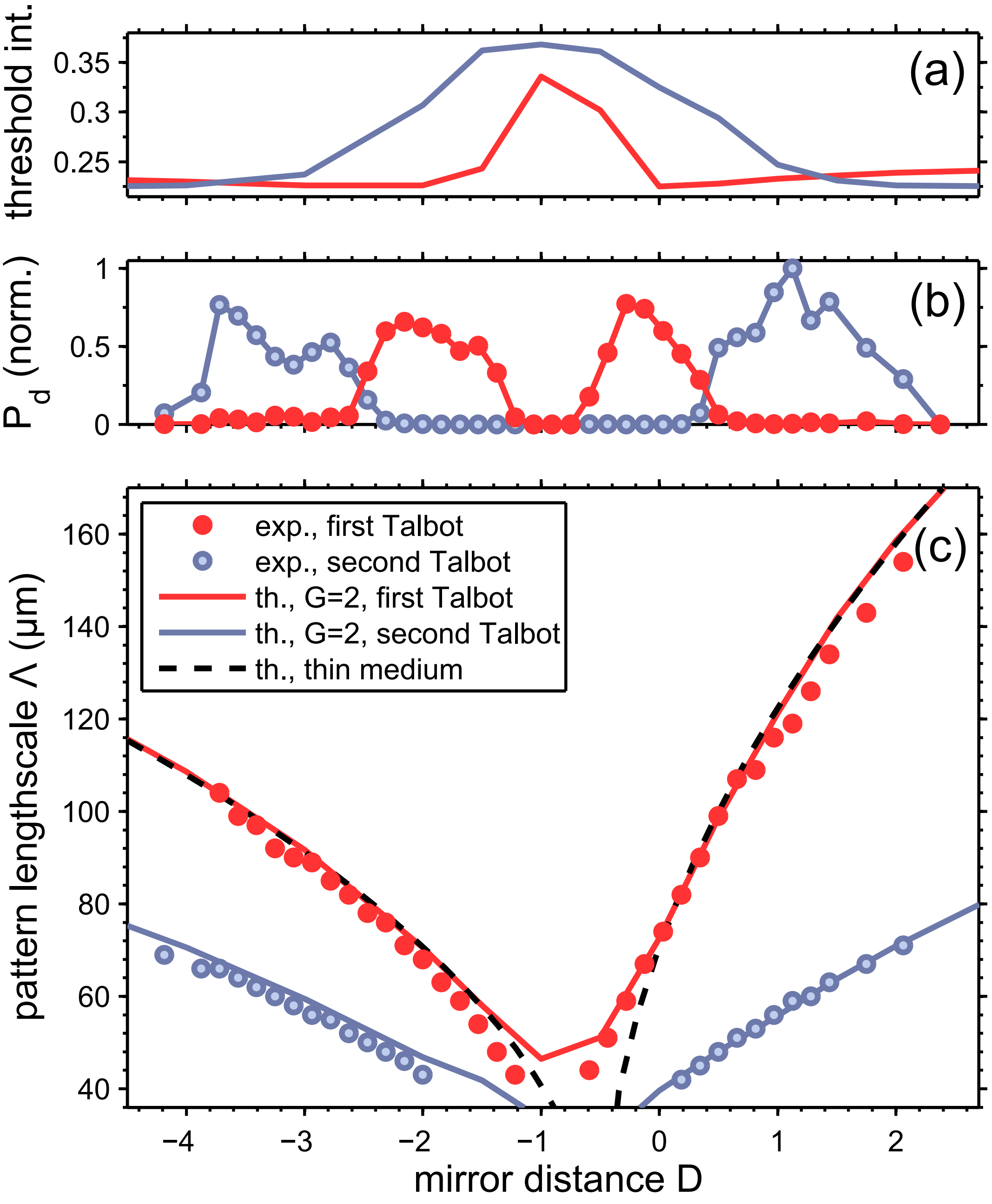

FIGURE 6.2: (a) Predicted threshold, (b) measured diffracted power, (c) pattern lengthscale Λ vs. mirror distance $D = (d - L/2)/L$, where d is the distance from the cloud center and L is effective medium length. Red solid dots: experimental data for first Talbot balloon (lowest wavenumber), blue circles: experimental data for second Talbot balloon (next highest wavenumber excited). The red and blue curves are the corresponding theoretical predictions and are calculated for a self-focusing Kerr medium with $h = 1$ described by $\hat{F}_{Kerr}$. Experimental parameters: effective medium length is $L = 3.2$ mm, beam intensity $I = 18$ mW/cm^2, B-fields $B_{x,y,z} = 0$, on-resonance optical thickness $b_0 = 27$ and detuning $\Delta = -14\,\Gamma_2$.

To further illustrate the change of diffracted power in the Talbot rings upon changing the mirror distance, far field pattern data taken in the orthogonal polarization channel are depicted in Fig. 6.3. For small $|D|$ (6.3a), only the first Talbot ring is excited. Increasing the mirror distance, the radius of the first ring reduces (Λ increases) and a second Talbot ring appears (6.3b), and completely takes over (6.3c). Increasing the distance further (6.3d), another ring with a higher radius is seen to be faintly excited. For even higher mirror distances (as limited by the setup) the power in the two rings decays to zero and the pattern formation does not occur at the used input intensities.

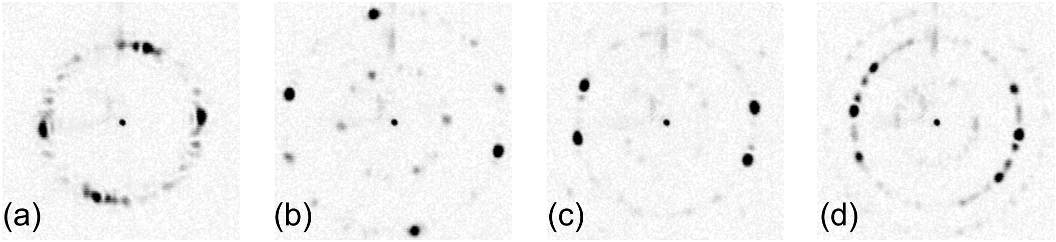

FIGURE 6.3: The patterns in far field for varying mirror distance $D = (d - L/2)/L$. (a) $D = -0.128$ ($d = 1.19$ mm). (b) $D = 0.497$ ($d = 3.19$ mm). (c) $D = 1.122$ ($d = 5.19$ mm). (d) $D = 1.434$ ($d = 6.19$ mm). Experimental parameters are the same as in Fig. 6.2.

6.3 Discussion

In the experiments in hot Na vapors [23], the thick medium effects can be neglected, as the diffraction within the medium is small with respect to a stronger effect governing the threshold behavior, the atomic diffusion. The atomic diffusion creates a threshold envelope function, causing the thresholds of the patterns at higher wavenumber harmonics to increase with q^2 (i.e. linearly with the diffraction parameter $\Theta = q^2 d/k$). This effect is the main mechanism for lifting the degeneracy of the higher harmonics in hot alkali vapor experiments.

The main result of this Chapter is the mirror distance scan of Fig. 6.2. This plot illustrates the competition between the two pattern lengthscales, mediated by the envelope curve. A nearly complete extinction of the first Talbot ring is seen, with the second ring taking over completely. A similar effect was predicted and observed in photorefractives, in spite of the different optical non-linearity mechanism [11, 141]. These results however only reported a coexistence of patterns at two lengthscales, without the extinction of power in the smaller and increase of power in the larger radius Talbot ring.

It is also shown that the time-independent linear stability analysis in the quasi-Kerr approximation (which is implicitly written in a scalar framework) works very well for calculating the pattern lengthscales Λ, and reasonably well for calculating the thresholds of the magnetization patterns. The reason for this is that the Zeeman non-linearity for the two circular components depends most strongly on the spin w variable, and linearly, which is for low powers linear in the pump rate and consequently also linear in the beam intensity.

Chapter 7

Conclusion and outlook

This Thesis reports on an experimental realization of self-organized magnetization patterns in a thermal ensemble of cold ^{87}Rb atoms driven by a detuned laser beam, in the single feedback mirror (SFM) configuration. The experimental results are shown to agree well with a theoretical model based on a simplification of the $F = 2 \rightarrow F' = 3$ transition to a more tractable $F = 1 \rightarrow F' = 2$ level structure. An external B-field is used to control the symmetry of the patterns. An antiferromagnetic phase is seen to occur for longitudinal B-fields close to zero, while a ferrimagnetic phase is seen to occur for a finite longitudinal B-field, changing the sign of magnetization when the sign of the longitudinal B-field is changed. The relatively localized peaks in the Fourier plane point to a long-range magnetic ordering.

The self-organized magnetization patterns in the SFM configuration are an example of a non-equilibrium phase transition, where the atomic degrees of freedom organize spontaneously via light mediated interaction. The light degrees of freedom can in principle be integrated out, leaving only the dynamical equations for the atomic degrees of freedom, and the explicit expressions for the atom-atom interactions could be obtained. The interaction between different magnetic multipoles could then also be more closely studied, which is a feature not presently explored in the experiments or theoretical models. The said rewriting of the theory would bring the patterns studied in this Thesis in closer relation with the theoretical framework used commonly in the quantum simulation community.

Cold atomic gases have in recent years been used to simulate the behavior of strongly correlated systems with many degrees of freedom, still posing a great challenge for even a conceptual understanding. The present cold atom self-organization experiments are however generally performed in single mode cavities, where the self-organized phase transitions break only discrete symmetries. In the SFM configuration, the initial system is translationally and rotationally symmetric around the pump axis. The self-organization thus breaks continuous symmetries, which is an interesting novel feature. In this Thesis the magnetization pattern formation is studied in a thermal atomic ensemble. The said medium is a middle ground between the more common magnetic systems studied in condensed matter (solid state) physics, with high densities and at high temperatures, and e.g. spinor BEC clouds, with high densities and at low temperatures.

Even though the pattern formation in atomic media has been studied for more than two decades, questions related to the atom-atom interaction, and the non-equilibrium thermodynamics of the system are still very little explored. One possible future direction would thus be to study the dispersion relation of spin density waves in the ordered system, which would provide direct information about the mirror mediated interaction between the atomic spins. A relatively simple way of performing this experiment would be by using a spatial light modulator to induce perturbations with longer wavelengths than the periodicity of the patterns, and monitor the way the system relaxes to the equilibrium patterned state. In addition to this, the interplay between the patterns relying on the Zeeman and the optomechanical non-linearities is another topic for future studies.

Appendix A

Derivation of the dynamical equations

A.1 Longitudinal B-field

In this Section of the Appendix the equations for the atomic dynamcs in the presence of only longitudinal B-field are derived (2.15). The derivation relies on the approximations described in Chapter 2 and the adiabatic elimination of the optical coherences [68]. The timescales of the evolution of the matrix elements are written in A.1. Inserting the Hamiltonian (2.7) and the decay and repopulation matrix elements calculated via the AtomicDensityMatrix Mathematica package [71] into the equation 2.1, one gets a set of the 20 relevant equations for the

r	transient repopulation	$2\pi\times10$ kHz
Γ_1	e.s. population decay	$2\pi\times6.066$ MHz
γ_1	$\lvert\Delta m\rvert = 2$ g.s. coherence decay	$2\pi\times10$ kHz
γ_1'	$\lvert\Delta m\rvert = 2$ e.s. coherence decay	$2\pi\times6.066$ MHz
Γ_2	$\lvert\Delta m\rvert = 1$ optical coherence decay	$2\pi\times3.033$ MHz
Γ_3	$\lvert\Delta m\rvert = 2$ optical coherence decay	$2\pi\times3.033$ MHz
γ_2	$\lvert\Delta m\rvert = 1$ e.s. coherence decay	$2\pi\times3.033$ MHz
Ω_z	Larmor frequency of longitudinal field	$2\pi\times0.1$ MHz
$\Omega_\pm$	Rabi frequency	$\lesssim 2\pi\times100$ MHz

Table A.1: Timescales of evolution of populations and coherences.

independent density matrix elements:

$$
\begin{aligned}
\dot{\rho}_{-1-1} &= \tfrac{r}{3} - r\rho_{-1-1} + \Gamma_1\left(\rho_{-2'-2'} + \tfrac{1}{2}\rho_{-1'-1'} + \tfrac{1}{6}\rho_{0'0'}\right) - i\left[\Omega'^{*}_{+}\rho_{-10'} - \Omega'_{+}\rho_{0'-1}\right. \\
&\quad \left. +\Omega^{*}_{-}\rho_{-1-2'} - \Omega_{-}\rho_{-2'-1}\right], \\
\dot{\rho}_{00} &= \tfrac{r}{3} - r\rho_{00} + \Gamma_1\left(\tfrac{1}{2}\rho_{-1'-1'} + \tfrac{2}{3}\rho_{0'0'} + \tfrac{1}{2}\rho_{1'1'}\right) - i\left[\Omega''^{*}_{+}\rho_{01'} - \Omega''_{+}\rho_{1'0}\right. \\
&\quad \left. +\Omega''^{*}_{-}\rho_{0-1'} - \Omega''_{-}\rho_{-1'0}\right], \\
\dot{\rho}_{11} &= \tfrac{r}{3} - r\rho_{11} + \Gamma_1\left(\tfrac{1}{6}\rho_{0'0'} + \tfrac{1}{2}\rho_{1'1'} + \rho_{2'2'}\right) - i\left[-\Omega_{+}\rho_{2'1} + \Omega^{*}_{+}\rho_{12'} + \Omega'^{*}_{-}\rho_{10'} - \Omega'_{-}\rho_{0'1}\right], \\
\dot{\rho}_{-11} &= \Gamma_1\left(\frac{\rho_{-2'0'}}{\sqrt{6}} + \frac{\rho_{-1'1'}}{2} + \frac{\rho_{0'2'}}{\sqrt{6}}\right) - \gamma_1\rho_{-11} - i\left[-\Omega_{-}\rho_{-2'1} - \Omega'_{+}\rho_{0'1} + \Omega'^{*}_{-}\rho_{-10'}\right. \\
&\quad \left. +\Omega^{*}_{+}\rho_{-12'} - 2g_g\Omega_z\rho_{-11}\right], \\
\dot{\rho}_{10'} &= -\Gamma_2\rho_{10'} - i\left[\Delta\rho_{10'} + g_g\Omega_z\rho_{10'} + \Omega'_{+}\rho_{1-1} + \Omega'_{-}\rho_{11}\right], \\
\dot{\rho}_{-10'} &= -\Gamma_2\rho_{-10'} - i\left[\Delta\rho_{-10'} - g_g\Omega_z\rho_{-10'} + \Omega'_{+}\rho_{-1-1} + \Omega'_{-}\rho_{-11}\right], \\
\dot{\rho}_{-1-2'} &= -\Gamma_2\rho_{-1-2'} - i\left[\Delta\rho_{-1-2'} + (2g_e - g_g)\Omega_z\rho_{-1-2'} + \Omega_{-}\rho_{-1-1}\right], \\
\dot{\rho}_{-2'1} &= -\Gamma_3\rho_{-2'1} - i\left[-\Delta\rho_{-2'1} - (g_g + 2g_e)\Omega_z\rho_{-2'1} - \Omega^{*}_{-}\rho_{-11}\right], \\
\dot{\rho}_{12'} &= -\Gamma_2\rho_{12'} - i\left[\Delta\rho_{12'} + (g_g - 2g_e)\Omega_z\rho_{12'} + \Omega_{+}\rho_{11}\right], \\
\dot{\rho}_{-12'} &= -\Gamma_3\rho_{-12'} - i\left[\Delta\rho_{-12'} - (g_g + 2g_e)\Omega_z\rho_{-12'} + \Omega_{+}\rho_{-11}\right], \\
\dot{\rho}_{0-1'} &= -\Gamma_2\rho_{0-1'} - i\left[\Delta\rho_{0-1'} + g_e\Omega_z\rho_{0-1'} + \Omega''_{-}\rho_{00}\right], \\
\dot{\rho}_{01'} &= -\Gamma_2\rho_{01'} - i\left[\Delta\rho_{01'} - g_e\Omega_z\rho_{01'} + \Omega''_{+}\rho_{00}\right], \\
\dot{\rho}_{-2'-2'} &= -\Gamma_1\rho_{-2'-2} - i\left[\Omega_{-}\rho_{-2'-1} - \Omega^{*}_{-}\rho_{-1-2'}\right], \\
\dot{\rho}_{-1'-1'} &= -\Gamma_1\rho_{-1'-1'} - i\left[\Omega''^{*}_{-}\rho_{-1'0} - \Omega''_{-}\rho_{0-1'}\right], \\
\dot{\rho}_{0'0'} &= -\Gamma_1\rho_{0'0'} - i\left[-\Omega'^{*}_{+}\rho_{-10'} + \Omega'_{+}\rho_{0'-1} + \Omega'_{-}\rho_{0'1} - \Omega'^{*}_{-}\rho_{10'}\right], \\
\dot{\rho}_{1'1'} &= -\Gamma_1\rho_{1'1'} - i\left[-\Omega''^{*}_{+}\rho_{01'} + \Omega''_{+}\rho_{1'0}\right], \\
\dot{\rho}_{2'2'} &= -\Gamma_1\rho_{2'2'} - i\left[-\Omega^{*}_{+}\rho_{12'} + \Omega_{+}\rho_{2'1}\right], \\
\dot{\rho}_{-2'0'} &= -\Gamma_1\rho_{-2'0'} - i\left[-2g_e\Omega_z\rho_{-2'0'} + \Omega'_{+}\rho_{-2'-1} + \Omega'_{-}\rho_{-2'1} - \Omega^{*}_{-}\rho_{-10'}\right], \\
\dot{\rho}_{-1'1'} &= -\Gamma_1\rho_{-1'1'} - i\left[-2g_e\Omega_z\rho_{-1'1'} + \Omega''_{+}\rho_{-1'0} - \Omega''^{*}_{-}\rho_{01'}\right], \\
\dot{\rho}_{0'2'} &= -\Gamma_1\rho_{0'2'} - i\left[-2g_e\Omega_z\rho_{0'2'} + \Omega_{+}\rho_{0'1} - \Omega'^{*}_{+}\rho_{-12'} - \Omega'^{*}_{-}\rho_{12'}\right].
\end{aligned}
\tag{A.1}
$$

where the primed indices of ρ_{ij} indicate the excited state and the non-primed indices of ρ_{ij} the ground state Zeeman sublevel. A shorthand notation was used for the Rabi frequencies, where $\Omega'_{\pm} = \Omega_{\pm}/\sqrt{6}$ and $\Omega''_{\pm} = \Omega_{\pm}/\sqrt{2}$. As the optical coherences, excited state populations and coherences evolve on timescales orders of magnitude faster than the ground state density matrix elements, they reach a steady state much sooner than the ground state density matrix elements and can be adiabatically eliminated. This procedure results in

$$
\begin{aligned}
\rho_{10'} &= \frac{\Omega'_-\rho_{11}+\Omega'_+\rho_{1-1}}{i\Gamma_2-(\Delta+g_g\Omega_z)},\\
\rho_{-10'} &= \frac{\Omega'_-\rho_{-11}+\Omega'_+\rho_{-1-1}}{i\Gamma_2-(\Delta-g_g\Omega_z)},\\
\rho_{-1-2'} &= \frac{\Omega_-\rho_{-1-1}}{i\Gamma_2-(\Delta+(2g_e-g_g)\Omega_z)},\\
\rho_{-2'1} &= \frac{-\Omega^*_-\rho_{-11}}{i\Gamma_3+(\Delta+(2g_e-g_g)\Omega_z)},\\
\rho_{12'} &= \frac{\Omega_+\rho_{11}}{i\Gamma_2-(\Delta+(g_g-2g_e)\Omega_z)},\\
\rho_{-12'} &= \frac{\Omega_+\rho_{-11}}{i\Gamma_3-(\Delta-(g_g+2g_e)\Omega_z)},\\
\rho_{0-1'} &= \frac{\Omega''_-\rho_{00}}{i\Gamma_2-(\Delta+g_e\Omega_z)},\\
\rho_{01'} &= \frac{\Omega''_+\rho_{00}}{i\Gamma_2-(\Delta-g_e\Omega_z)},\\
\rho_{-2'-2'} &= \frac{-i}{\Gamma_1}(\Omega_-\rho_{-2'-1} - \Omega^*_-\rho_{-1-2'}) = \frac{2P_-}{\Gamma_1}\rho_{-1-1},\\
\rho_{-1'-1'} &= \frac{-i}{\Gamma_1}(\Omega''^*_-\rho_{-1'0} - \Omega''_-\rho_{0-1'}) = \frac{2P''_-}{\Gamma_1}\rho_{00},\\
\rho_{0'0'} &= \frac{-i}{\Gamma_1}(-\Omega'^*_+\rho_{-10'} + \Omega'_+\rho_{0'-1} + \Omega'_-\rho_{0'1} - \Omega'^*_-\rho_{10'}),\\
&= \frac{2P'_+}{\Gamma_1}\rho_{-1-1} + \frac{2P'_-}{\Gamma_1}\rho_{11}\\
&\quad +\frac{i}{\Gamma_1}\left(\Omega'^*_+\Omega'_-\frac{\rho_{-11}}{i\Gamma_2-(\Delta-g_g\Omega_z)}\right.\\
&\quad \left.+\Omega'_+\Omega'^*_-\frac{\rho_{1-1}}{i\Gamma_2+(\Delta-g_g\Omega_z)} + \Omega'_+\Omega'^*_-\frac{\rho_{1-1}}{i\Gamma_2-(\Delta+g_g\Omega_z)} + \Omega'^*_+\Omega'_-\frac{\rho_{-11}}{i\Gamma_2+(\Delta+g_g\Omega_z)}\right),\\
\rho_{1'1'} &= \frac{-i}{\Gamma_1}(-\Omega''^*_+\rho_{01'} + \Omega''_+\rho_{1'0}) = \frac{2P''_+}{\Gamma_1}\rho_{00},\\
\rho_{2'2'} &= \frac{-i}{\Gamma_1}(-\Omega^*_+\rho_{12'} + \Omega_+\rho_{2'1}) = \frac{2P_+}{\Gamma_1}\rho_{11}\\
\rho_{-2'0'} &= \frac{-i}{\Gamma_1}\left(\Omega'_+\rho_{-2'-1} + \Omega'_-\rho_{-2'1} - \Omega^*_-\rho_{-10'}\right),\\
\rho_{-1'1'} &= \frac{-i}{\Gamma_1}\left(\Omega''_+\rho_{-1'0} - \Omega''^*_-\rho_{01'}\right),\\
\rho_{0'2'} &= \frac{-i}{\Gamma_1}\left(\Omega_+\rho_{0'1} - \Omega'^*_+\rho_{-12'} - \Omega'^*_-\rho_{12'}\right).
\end{aligned}
\tag{A.2}
$$

Using these relations with the Lande factors $g_g = g_e = 1$ and the reduced density matrix elements defined in (2.11) leads to the equations 2.15.

A.2 Transverse $B-$fields

The Hamlitonian calculated from the AtomicDensityMatrix Mathematica package is

$$\hat{H}/\hbar = \begin{pmatrix} g_g\Omega_z & \frac{g_g(\Omega_x - i\Omega_y)}{\sqrt{2}} & 0 & -\Omega_+ & 0 & -\frac{\Omega_-}{\sqrt{6}} & 0 & 0 \\ \frac{g_g(\Omega_x + i\Omega_y)}{\sqrt{2}} & 0 & \frac{g_g(\Omega_x - i\Omega_y)}{\sqrt{2}} & 0 & -\frac{\Omega_+}{\sqrt{2}} & 0 & -\frac{\Omega_-}{\sqrt{2}} & 0 \\ 0 & \frac{g_g(\Omega_x + i\Omega_y)}{\sqrt{2}} & -g_g\Omega_z & 0 & 0 & -\frac{\Omega_+}{\sqrt{6}} & 0 & -\Omega_- \\ -\Omega_+^* & 0 & 0 & 2g_e\Omega_z - \Delta & g_e\left(\Omega_x - i\Omega_y\right) & 0 & 0 & 0 \\ 0 & -\frac{\Omega_+^*}{\sqrt{2}} & 0 & g_e\left(\Omega_x + i\Omega_y\right) & g_e\Omega_z - \Delta & \sqrt{\frac{3}{2}}g_e\left(\Omega_x - i\Omega_y\right) & 0 & 0 \\ -\frac{\Omega_-^*}{\sqrt{6}} & 0 & -\frac{\Omega_+^*}{\sqrt{6}} & 0 & \sqrt{\frac{3}{2}}g_e\left(\Omega_x + i\Omega_y\right) & -\Delta & \sqrt{\frac{3}{2}}g_e\left(\Omega_x - i\Omega_y\right) & 0 \\ 0 & -\frac{\Omega_-^*}{\sqrt{2}} & 0 & 0 & 0 & \sqrt{\frac{3}{2}}g_e\left(\Omega_x + i\Omega_y\right) & -\Delta - g_e\Omega_z & g_e\left(\Omega_x - i\Omega_y\right) \\ 0 & 0 & -\Omega_-^* & 0 & 0 & 0 & g_e\left(\Omega_x + i\Omega_y\right) & -\Delta - 2g_e\Omega_z \end{pmatrix} \tag{A.3}$$

The equations (2.19) are now derived by the same procedure as in A.1, which results in a more involved calculation, details of which will not be presented here.

A.3 Optical response

In this Section the equations of the medium response are derived by the same procedure as described in Ref. [68] for the $J = 1/2 \to J' = 1/2$ system. The polarization writes as

$$\mathbf{P}(t) = \frac{1}{2}\left(P_+ e^{-i\omega t} + P_+^* e^{i\omega t}\right)\hat{\mathbf{e}}_+ + \frac{1}{2}\left(P_- e^{-i\omega t} + P_-^* e^{i\omega t}\right)\hat{\mathbf{e}}_-. \tag{A.4}$$

The relation connecting the density matrix elements and polarization is [68]

$$\mathbf{P}(t) = N\,\langle \boldsymbol{\mu}_E \rangle = N\,\mathrm{Tr}\,(\,\boldsymbol{\mu}_E\,\hat{\rho}(t))\,, \tag{A.5}$$

where N is peak density of atoms and $\boldsymbol{\mu}_E$ is the dipole operator. The dipole operator components of the $\sigma^\pm$ light can in the basis of eigenvectors of our system be written as

$$\mu_+ = \mu_E(C_{-10'}(|-1\rangle\langle 0'| + |0'\rangle\langle -1|) + C_{01'}(|0\rangle\langle 1'| + |1'\rangle\langle 0|) + C_{12'}(|1\rangle\langle 2'| + |2'\rangle\langle 1|)),$$

$$\mu_- = \mu_E(C_{10'}(|1\rangle\langle 0'| + |0'\rangle\langle 1|) + C_{0-1'}(|0\rangle\langle -1'| + |-1'\rangle\langle 0|) + C_{-1-2'}(|-1\rangle\langle -2'| + |-2'\rangle\langle -1|)), \tag{A.6}$$

where $\{|m\rangle,\ |m'\rangle\}$ are the ground and excited state vectors, respectively, C_{ij} are Clebsch-Gordan (C.G.) coefficients and

$$\tilde{\rho} = \rho_{i,j} e^{-i\omega t}, \quad i = \text{e.s.}, j = \text{g.s.}, \quad \rho_{i,j} = \langle i|\hat{\rho}|j\rangle \tag{A.7}$$

are the density matrix elements. The C.G. coefficients can be calculated from the Wigner-Eckart theorem

$$\langle F' m'_F | \mu_\pm | F m_F \rangle = (-1)^{F'-m'_F} \langle F' || \mu || F \rangle \begin{pmatrix} F' & 1 & F \\ -m'_F & \pm 1 & m_F \end{pmatrix} \tag{A.8}$$

and are written in Table A.2. The quantity μ_E is related to the reduced dipole matrix element via $\mu_E = \frac{\langle 2' || \mu || 1 \rangle}{\sqrt{5}}$. This gives

$$\begin{aligned} \langle \mu_+ \rangle = \mu_E \big[& C_{-10'} \left(\rho_{-10'} e^{i\omega t} + \rho_{0'-1} e^{-i\omega t} \right) + C_{01'} \left(\rho_{01'} e^{i\omega t} + \rho_{1'0} e^{-i\omega t} \right) \\ & + C_{12'} \left(\rho_{12'} e^{i\omega t} + \rho_{2'1} e^{-i\omega t} \right) \big] , \\ \langle \mu_- \rangle = \mu_E \big[& C_{10'} \left(\rho_{10'} e^{i\omega t} + \rho_{0'1} e^{-i\omega t} \right) + C_{0-1'} \left(\rho_{0-1'} e^{i\omega t} + \rho_{-1'0} e^{-i\omega t} \right) \\ & + C_{-1-2'} \left(\rho_{-1-2'} e^{i\omega t} + \rho_{-2'-1} e^{-i\omega t} \right) \big] . \end{aligned} \tag{A.9}$$

The polarization functions of the $\sigma^\pm$ components are now

$$P_\pm = \frac{b_0}{2} \frac{-(\Delta \mp \Omega_z) - i\Gamma_2}{\Gamma_2^2 + (\Delta \mp \Omega_z)^2} \left(\frac{3}{20} \left(u \mp iv \right) E_\mp + \left(\pm \frac{3}{4} w + \frac{1}{20} x + 1 \right) E_\pm \right) , \tag{A.10}$$

where the relation $b_0/2 = \sqrt{5} N \mu_E^2 / 9\hbar$ was used to relate the polarization function to the experimentally measured quantities.

$C_{12'} = C_{2'1}$	1	$C_{10'} = C_{0'1}$	$\frac{1}{\sqrt{6}}$
$C_{01'} = C_{1'0}$	$\frac{1}{\sqrt{2}}$	$C_{0-1'} = C_{-1'0}$	$\frac{1}{\sqrt{2}}$
$C_{-10'} = C_{0'-1}$	$\frac{1}{\sqrt{6}}$	$C_{-1-2'} = C_{-2'-1}$	1

Table A.2: Clebsch Gordan coefficients needed to calculate the electric dipole operator matrix elements via the Wigner-Eckart theorem.

List of original publications

1. Firth, W. J. and Krešić, I. and Labeyrie, G. and Camara, A. and Gomes, P. and Ackemann, T. Analysis of pattern forming instabilities in an ensemble of two-level atoms optically excited by counter-propagating fields. *ArXiv e-prints*, 1606.04885, June 2016.
2. Araújo, Michelle O and Krešić, Ivor and Kaiser, Robin and Guerin, William. Superradiance in a Large and Dilute Cloud of Cold Atoms in the Linear-Optics Regime. *Phys. Rev. Lett.*, 117(7):073002, August 2016.
3. I. Kresic, G. Labeyrie, G. Robb, R. Kaiser and T. Ackemann. Magnetization patterns in cold atoms. Manuscript in preparation.

Bibliography

[1] G. Grynberg et al. “Observation of instabilities due to mirrorless four-wave mixing oscillation in sodium”. In: *Opt. Comm.* 67.5 (1988), pp. 363 –366.

[2] D. J. Gauthier, M. S. Malcuit, and R. W. Boyd. “Polarization instabilities of counterpropagating laser beams in sodium vapor”. In: *Phys. Rev. Lett.* 61 (16 1988), pp. 1827–1830.

[3] W. J. Firth and C. Paré. “Transverse modulational instabilities for counterpropagating beams in Kerr media”. In: *Opt. Lett.* 13.12 (1988), pp. 1096–1098.

[4] W. J. Firth. “Spatial instabilities in a Kerr medium with single feedback mirror”. In: *J. Mod. Opt.* 37 (1990), pp. 151–153.

[5] R. Macdonald and H.J. Eichler. “Spontaneous optical pattern formation in a nematic liquid crystal with feedback mirror”. In: *Opt. Comm.* 89.2 (1992), pp. 289 –295.

[6] B. Thüring, R. Neubecker, and T. Tschudi. “Transverse pattern formation in liquid crystal light valve feedback system”. In: *Opt. Comm.* 102.1 (1993), pp. 111 –115.

[7] E. Pampaloni et al. “Experimental evidence of boundary-induced symmetries in an optical system with a Kerr-like non-linearity”. In: *Europhys. Lett.* 25 (1994), pp. 587–592.

[8] M. A. Vorontsov and A. Yu. Karpov. “Kerr slice-based nonlinear interferometer with two-dimensional feedback: control of roll and hexagon formation”. In: *Opt. Lett.* 20.24 (1995), pp. 2466–2468.

[9] J. Glückstad and M. Saffman. “Spontaneous pattern formation in a thin film of bacteriorhodopsin with mixed absorptive–dispersive nonlinearity”. In: *Opt. Lett.* 20.6 (1995), pp. 551–553.

[10] T. Honda. “Hexagonal pattern formation due to counterpropagation in KNbO3”. In: *Opt. Lett.* 18.8 (1993), pp. 598–600.

[11] M. Schwab et al. “Origin and control of dynamics of hexagonal patterns in a photorefractive feedback system”. In: *Chaos, Solitons & Fractals* 10 (1999), pp. 701–708.

[12] G. Grynberg, A. Maître, and A. Petrossian. “Flowerlike patterns generated by a laser beam transmitted through a rubidium cell with a single feedback mirror”. In: *Phys. Rev. Lett.* 72 (1994), pp. 2379–2382.

[13] T. Ackemann and W. Lange. “Non- and nearly hexagonal patterns in sodium vapor generated by single-mirror feedback”. In: *Phys. Rev. A* 50 (6 1994), R4468–R4471.

[14] T. Ackemann et al. “Transition between positive and negative hexagons in optical pattern formation”. In: *Phys. Rev. Lett.* 75 (1995), pp. 3450–3453.

[15] J. A. Greenberg, B. L. Schmittberger, and D. J. Gauthier. “Bunching-induced optical nonlinearity and instability in cold atoms”. In: *Opt. Express* 19.23 (2011), pp. 22535–22549.

[16] B. L. Schmittberger and D. J. Gauthier. “Transverse optical and atomic pattern formation”. In: *JOSA B* 33.7 (2016), pp. 1543–1551.

[17] B. L. Schmittberger and D. J. Gauthier. “Spontaneous emergence of free-space optical and atomic patterns”. In: *New J. of Phys.* 18.10 (2016), p. 103021.

[18] G. Labeyrie et al. “Optomechanical self-structuring in cold atomic gases”. In: *Nat. Photon.* 8 (2014), pp. 321 –325.

[19] A. Camara et al. “Optical pattern formation with a two-level nonlinearity”. In: *Phys. Rev. A* 92 (1 2015), p. 013820.

[20] A. Ashkin, J. M. Dziedzic, and P. W. Smith. "Continuous-wave self-focusing and self-trapping of light in artificial Kerr media". In: *Opt. Lett.* 7 (), pp. 276–279.

[21] G. A. Muradyan et al. "Absolute Instability and Pattern Formation in Cold Atomic Vapors". In: *Nonlinear Guided Waves and Their Applications.* Optical Society of America, 2005, ThB29.

[22] C. J. Foot. *Atomic Physics (Oxford Master Series in Atomic, Optical and Laser Physics).* 1st ed. 2005.

[23] T. Ackemann and W. Lange. "Optical pattern formation in alkali metal vapors: Mechanisms, phenomena and use". In: *Appl. Phys. B* 72.1 (2001), pp. 21–34.

[24] D. Jaksch et al. "Cold bosonic atoms in optical lattices". In: *Phys. Rev. Lett.* 81.15 (1998), p. 3108.

[25] M. Greiner et al. "Quantum phase transition from a superfluid to a Mott insulator in a gas of ultracold atoms". In: *Nature* 415.6867 (2002), pp. 39–44.

[26] I. Bloch, J. Dalibard, and W. Zwerger. "Many-body physics with ultracold gases". In: *Rev. Mod. Phys.* 80.3 (2008), p. 885.

[27] H. Ritsch et al. "Cold atoms in cavity-generated dynamical optical potentials". In: *Rev. Mod. Phys.* 85.2 (2013), p. 553.

[28] K. Baumann et al. "Dicke quantum phase transition with a superfluid gas in an optical cavity". In: *Nature* 464.7293 (2010), pp. 1301–1306.

[29] B. M. Garraway. "The Dicke model in quantum optics: Dicke model revisited". In: *Phil. Trans. R. Soc. A* 369.1939 (2011), pp. 1137–1155.

[30] J. Léonard et al. "Supersolid formation in a quantum gas breaking continuous translational symmetry". In: *arXiv preprint arXiv:1609.09053* (2016).

[31] M. Boninsegni and N. V. Prokof'ev. "Colloquium: Supersolids: What and where are they?" In: *Rev. Mod. Phys.* 84 (2 2012), pp. 759–776.

[32] A. J. Kollár et al. "Supermode-Density-Wave-Polariton Condensation". In: *arXiv preprint arXiv:1606.04127* (2016).

[33] S. Gopalakrishnan, B. L. Lev, and P. M. Goldbart. "Emergent crystallinity and frustration with Bose–Einstein condensates in multimode cavities". In: *Nat. Phys.* 5.11 (2009), pp. 845–850.

[34] S. Gopalakrishnan, B. L. Lev, and P. M. Goldbart. "Atom-light crystallization of Bose-Einstein condensates in multimode cavities: Nonequilibrium classical and quantum phase transitions, emergent lattices, supersolidity, and frustration". In: *Phys. Rev. A* 82.4 (2010), p. 043612.

[35] S. Gopalakrishnan, B. L. Lev, and P. M. Goldbart. "Frustration and glassiness in spin models with cavity-mediated interactions". In: *Phys. Rev. Lett.* 107.27 (2011), p. 277201.

[36] D. E. Chang, J. I. Cirac, and H. J. Kimble. "Self-organization of atoms along a nanophotonic waveguide". In: *Phys. Rev. Lett.* 110.11 (2013), p. 113606.

[37] A. Goban et al. "Atom–light interactions in photonic crystals". In: *Nat. Comm.* 5 (2014).

[38] E. Tesio. "Theory of self-organisation in cold atoms". PhD thesis. University of Strathclyde, 2014.

[39] G. R. M. Robb et al. "Quantum Threshold for Optomechanical Self-Structuring in a Bose-Einstein Condensate". In: *Phys. Rev. Lett.* 114 (17 2015), p. 173903.

[40] S. Ostermann, F. Piazza, and H. Ritsch. "Spontaneous Crystallization of Light and Ultracold Atoms". In: *Phys. Rev. X* 6 (2 2016), p. 021026.

[41] C. Von Cube et al. "Self-synchronization and dissipation-induced threshold in collective atomic recoil lasing". In: *Phys. Rev. Lett.* 93.8 (2004), p. 083601.

[42] A. T. Black, H. W. Chan, and V. Vuletic. "Observation of collective friction forces due to spatial self-organization of atoms: from Rayleigh to Bragg scattering". In: *Phys. Rev. Lett.* 91.20 (2003), p. 203001.

[43] H. W. Chan, A. T. Black, and V. Vuletić. “Observation of collective-emission-induced cooling of atoms in an optical cavity”. In: *Phys. Rev. Lett.* 90.6 (2003), p. 063003.

[44] E. Tesio et al. “Spontaneous optomechanical pattern formation in cold atoms”. In: *Phys. Rev. A* 86.3 (2012), p. 031801.

[45] S. Schütz, S. B. Jäger, and G. Morigi. “Thermodynamics and dynamics of atomic self-organization in an optical cavity”. In: *Phys. Rev. A* 92.6 (2015), p. 063808.

[46] S. Schütz, S. B. Jäger, and G. Morigi. “Dissipation-assisted prethermalization in long-range interacting atomic ensembles”. In: *Phys. Rev. Lett.* 117.8 (2016), p. 083001.

[47] G. Grynberg and L.A. Lugiato. “Quantum properties of hexagonal patterns”. In: *Opt. Comm.* 101.1 (1993), pp. 69 –73.

[48] E. S. Polzik, J. Carri, and H. J. Kimble. “Spectroscopy with squeezed light”. In: *Phys. Rev. Lett.* 68 (20 1992), pp. 3020–3023.

[49] I. D. Leroux, M. H. Schleier-Smith, and V. Vuletic. “Implementation of Cavity Squeezing of a Collective Atomic Spin”. In: *Phys. Rev. Lett.* 104 (7 2010), p. 073602.

[50] J. A. Greenberg and D. J. Gauthier. “High-order optical nonlinearity at low light levels”. In: *EPL* 98.2 (2012), p. 24001.

[51] E. Tesio et al. “Dissipative solitons in the coupled dynamics of light and cold atoms”. In: *Opt. Express* 21.22 (2013), pp. 26144–26149.

[52] H. F. Talbot. “LXXVI. Facts relating to optical science. No. IV”. In: *The Lond. and Edi. Phil. Mag. and J. of Sci.* 9.56 (1836), pp. 401–407.

[53] A. J. Kollár et al. “An adjustable-length cavity and Bose–Einstein condensate apparatus for multimode cavity QED”. In: *New J. of Phys.* 17.4 (2015), p. 043012.

[54] R. W. Boyd. *Nonlinear optics.* Burlington, MA: Elsevier Science, 2013.

[55] D. M. Stamper-Kurn and M. Ueda. “Spinor Bose gases: Symmetries, magnetism, and quantum dynamics”. In: *Rev. Mod. Phys.* 85.3 (2013), p. 1191.

[56] M. Weidemüller et al. “Bragg Diffraction in an Atomic Lattice Bound by Light”. In: *Phys. Rev. Lett.* 75 (25 1995), pp. 4583–4586.

[57] S. H. Strogatz. *Nonlinear dynamics and chaos: with applications to physics, biology, chemistry, and engineering.* Westview press, 2014.

[58] J. Guckenheimer and P. J. Holmes. *Nonlinear oscillations, dynamical systems, and bifurcations of vector fields.* Vol. 42. Springer Science & Business Media, 2013.

[59] M. C. Cross and P. C. Hohenberg. “Pattern formation outside of equilibrium”. In: *Rev. Mod. Phys.* 65 (3 1993), pp. 851–1112.

[60] F. T. Arecchi, S. Boccaletti, and P.-L. Ramazza. “Pattern formation and competition in nonlinear optics”. In: *Phys. Rep.* 318.1 (1999), pp. 1–83.

[61] A. M. Turing. “The chemical basis of morphogenesis”. In: *Philos. Trans. R. Soc. Lond., B, Biol. Sci.* 237.641 (1952), pp. 37–72.

[62] G. Nicolis and I. Prigogine. *Self-organization in nonequilibrium systems.* Vol. 191977. Wiley, New York, 1977.

[63] H. Haken. “Synergetics”. In: *Phys. Bulletin* 28.9 (1977), p. 412.

[64] V. I. Krinsky. *Self-organization: autowaves and structures far from equilibrium.* Springer, 1984.

[65] G. D’Alessandro and W. J. Firth. “Hexagonal spatial pattern for a Kerr slice with a feedback mirror”. In: *Phys. Rev. A* 46 (1992), pp. 537–548.

[66] A. Aumann. “Optical Patterns and Quasipatterns in an Alkali Metal Vapor with Feedback”. PhD thesis. Westfalische Wilhelms-Universität, 1999.

[67] R. P. Feynman, F. L. Vernon, and R. W. Hellwarth. “Geometrical Representation of the Schrödinger Equation for Solving Maser Problems”. In: *J. Appl. Phys.* 28.1 (1957).

[68] F. Mitschke et al. “Magnetically induced optical self-pulsing in a nonlinear resonator”. In: *Phys. Rev. A* 33 (5 1986), pp. 3219–3231.

[69] M. Möller and W. Lange. "Radiation trapping: An alternative mechanism for chaos in a nonlinear optical resonator". In: *Phys. Rev. A* 49 (5 1994), pp. 4161–4169.

[70] T. Ackemann et al. "Transition between Positive and Negative Hexagons in Optical Pattern Formation". In: *Phys. Rev. Lett.* 75 (19 1995), pp. 3450–3453.

[71] S. M. Rochester. "Modeling Nonlinear Magneto-optical Effects in Atomic Vapors". PhD thesis. University of California, Berkeley, 2010.

[72] D. A. Steck. *Rubidium 87 D line data.* 2001.

[73] G. B. Arfken and H. J. Weber. *Mathematical methods for physicists.* AAPT, 1999.

[74] J. Dalibard and C. Cohen-Tannoudji. "Laser cooling below the Doppler limit by polarization gradients: simple theoretical models". In: *JOSA B* 6.11 (1989), pp. 2023–2045.

[75] T. Ackemann. "Dynamische Instabilitäten in einem samariumdampfgefüllten Fabry-Perot-Resonator". MA thesis. Westfalische Wilhelms-Universität, 1992.

[76] M. Fleischhauer, A. Imamoglu, and J. P. Marangos. "Electromagnetically induced transparency: Optics in coherent media". In: *Rev. Mod. Phys.* 77.2 (2005), p. 633.

[77] G. Labeyrie, Ch. Miniatura, and R. Kaiser. "Large Faraday rotation of resonant light in a cold atomic cloud". In: *Phys. Rev. A* 64.3 (2001), p. 033402.

[78] A. Wojciechowski et al. "Nonlinear Faraday rotation and detection of superposition states in cold atoms". In: *Phys. Rev. A* 81 (5 2010), p. 053420.

[79] J. C. Maxwell. *A treatise on electricity and magnetism.* Vol. 1. Clarendon press, 1881.

[80] P Lebedev. "The experimental study of the pressure of the light". In: *Ann. Phys* 6 (1901), p. 433.

[81] E. F. Nichols and G. F. Hull. “The Pressure Due to Radiation. (Second Paper.)” In: *Phys. Rev. (Series I)* 17 (1 1903), pp. 26–50.

[82] R Frisch. “Experimenteller Nachweis des Einsteinschen Strahlungsrückstoßes”. In: *Z. Phys. A-Hadron Nucl.* 86.1 (1933), pp. 42–48.

[83] A. Ashkin. “Acceleration and Trapping of Particles by Radiation Pressure”. In: *Phys. Rev. Lett.* 24 (4 1970), pp. 156–159.

[84] T.W. Hänsch and A.L. Schawlow. “Cooling of gases by laser radiation”. In: *Opt. Comm.* 13.1 (1975), pp. 68 –69.

[85] E. L. Raab et al. “Trapping of neutral sodium atoms with radiation pressure”. In: *Phys. Rev. Lett.* 59.23 (1987), p. 2631.

[86] P. D. Lett et al. “Observation of atoms laser cooled below the Doppler limit”. In: *Phys. Rev. Lett.* 61.2 (1988), p. 169.

[87] D. S. Weiss et al. “Optical molasses and multilevel atoms: experiment”. In: *JOSA B* 6.11 (1989), pp. 2072–2083.

[88] J. Dalibard and C. Cohen-Tannoudji. “Dressed-atom approach to atomic motion in laser light: the dipole force revisited”. In: *JOSA B* 2.11 (1985), pp. 1707–1720.

[89] K. B. Davis et al. “Bose-Einstein condensation in a gas of sodium atoms”. In: *Phys. Rev. Lett.* 75.22 (1995), p. 3969.

[90] E. A. Cornell and C. E. Wieman. “Nobel Lecture: Bose-Einstein condensation in a dilute gas, the first 70 years and some recent experiments”. In: *Rev. Mod. Phys.* 74.3 (2002), p. 875.

[91] C. C. Bradley et al. “Evidence of Bose-Einstein condensation in an atomic gas with attractive interactions”. In: *Phys. Rev. Lett.* 75.9 (1995), p. 1687.

[92] F. Dalfovo et al. “Theory of Bose-Einstein condensation in trapped gases”. In: *Rev. Mod. Phys.* 71 (3 1999), pp. 463–512.

[93] K. M. O’hara et al. “Observation of a strongly interacting degenerate Fermi gas of atoms”. In: *Science* 298.5601 (2002), pp. 2179–2182.

[94] Z. Hadzibabic et al. “Two-Species Mixture of Quantum Degenerate Bose and Fermi Gases”. In: *Phys. Rev. Lett.* 88 (16 2002), p. 160401.

[95] C. A. Regal, M. Greiner, and D. S. Jin. “Observation of resonance condensation of fermionic atom pairs”. In: *Phys. Rev. Lett.* 92.4 (2004), p. 040403.

[96] J. D. Pritchard et al. “Cooperative Atom-Light Interaction in a Blockaded Rydberg Ensemble”. In: *Phys. Rev. Lett.* 105 (19 2010), p. 193603.

[97] S. L. Bromley et al. “Collective atomic scattering and motional effects in a dense coherent medium”. In: *Nat. Comm.* 7 (2016).

[98] W. Guerin, M. O. Araújo, and R. Kaiser. “Subradiance in a Large Cloud of Cold Atoms”. In: *Phys. Rev. Lett.* 116 (8 2016), p. 083601.

[99] M. O. Araújo et al. “Superradiance in a Large and Dilute Cloud of Cold Atoms in the Linear-Optics Regime”. In: *Phys. Rev. Lett.* 117.7 (2016), p. 073002.

[100] S. J. Roof et al. “Observation of Single-Photon Superradiance and the Cooperative Lamb Shift in an Extended Sample of Cold Atoms”. In: *Phys. Rev. Lett.* 117 (7 2016), p. 073003.

[101] A. Nicolas et al. “A quantum memory for orbital angular momentum photonic qubits”. In: *Nat. Photon.* 8.3 (2014), pp. 234–238.

[102] B. Albrecht et al. “Controlled Rephasing of Single Collective Spin Excitations in a Cold Atomic Quantum Memory”. In: *Phys. Rev. Lett.* 115 (16 2015), p. 160501.

[103] N. Sangouard et al. “Quantum repeaters based on atomic ensembles and linear optics”. In: *Rev. Mod. Phys.* 83 (1 2011), pp. 33–80.

[104] Z. Chen et al. “Conditional spin squeezing of a large ensemble via the vacuum Rabi splitting”. In: *Phys. Rev. Lett.* 106.13 (2011), p. 133601.

[105] N. Behbood et al. “Generation of Macroscopic Singlet States in a Cold Atomic Ensemble”. In: *Phys. Rev. Lett.* 113 (9 2014), p. 093601.

[106] R. McConnell et al. “Entanglement with negative Wigner function of almost 3,000 atoms heralded by one photon”. In: *Nature* 519.7544 (2015), pp. 439–442.

[107] W. Chen et al. “All-optical switch and transistor gated by one stored photon”. In: *Science* (2013), p. 1237242.

[108] M. Chalony et al. “Long-range one-dimensional gravitational-like interaction in a neutral atomic cold gas”. In: *Phys. Rev. A* 87 (1 2013), p. 013401.

[109] N. Šantić et al. “Experimental Demonstration of a Synthetic Lorentz Force by Using Radiation Pressure”. In: *Sci. Rep.* 5 (2015).

[110] C. C. Nshii et al. “A surface-patterned chip as a strong source of ultracold atoms for quantum technologies”. In: *Nat. Nanotech.* 8.5 (2013), pp. 321–324.

[111] J. P. McGilligan et al. “Phase-space properties of magneto-optical traps utilising micro-fabricated gratings.” In: *Opt. Express* 23.7 (2015), pp. 8948–8959.

[112] C. S. Adams and E. Riis. “Laser cooling and trapping of neutral atoms”. In: *Prog. in Quant. Electron.* 21.1 (1997), pp. 1 –79.

[113] W. D Phillips. “Nobel Lecture: Laser cooling and trapping of neutral atoms”. In: *Rev. Mod. Phys.* 70.3 (1998), p. 721.

[114] H. Metcalf and P. van der Straten. “Cooling and trapping of neutral atoms”. In: *Phys. Rep.* 244.4-5 (1994), pp. 203–286.

[115] H. J. Metcalf and P. Straten. *Laser cooling and trapping of neutral atoms.* Wiley Online Library, 2007.

[116] M. Vangeleyn. “Atom trapping in non-trivial geometries for micro-fabrication applications”. PhD thesis. University of Strathclyde, 2011.

[117] T. W. Hänsch, I. S. Shahin, and A. L. Schawlow. “High-Resolution Saturation Spectroscopy of the Sodium D Lines with a Pulsed Tunable Dye Laser”. In: *Phys. Rev. Lett.* 27 (11 1971), pp. 707–710.

[118] A. S. Arnold, J. S. Wilson, and M. G. Boshier. “A simple extended-cavity diode laser”. In: *Rev. Sci. Instrum.* 69.3 (1998).

[119] A. S. Arnold. “Preparation and manipulation of an 87Rb Bose-Einstein condensate”. PhD thesis. University of Sussex, 1999.

[120] E. Ciaramella, M. Tamburrini, and E. Santamato. “Talbot assisted hexagonal beam patterning in a thin liquid crystal film with a single feedback mirror at negative distance”. In: *Appl. Phys. Lett.* 63.12 (1993).

[121] I. H. Malitson. “Interspecimen Comparison of the Refractive Index of Fused Silica∗,†”. In: *J. Opt. Soc. Am.* 55.10 (1965), pp. 1205–1209.

[122] T. Walker, D. Sesko, and C. Wieman. “Collective behavior of optically trapped neutral atoms”. In: *Phys. Rev. Lett.* 64 (4 1990), pp. 408–411.

[123] M. T. DePue et al. “Transient compression of a MOT and high intensity fluorescent imaging of optically thick clouds of atoms”. In: *Opt. Comm.* 180.1–3 (2000), pp. 73 –79.

[124] G. L. Gattobigio et al. “Scaling laws for large magneto-optical traps”. In: *Phys. Scripta* 81.2 (2010), p. 025301.

[125] W. J. Firth et al. “Analysis of pattern forming instabilities in an ensemble of two-level atoms optically excited by counter-propagating fields”. In: *ArXiv e-prints* (June 2016). arXiv: `1606.04885 [physics.atom-ph]`.

[126] G. Bohm and G. Zech. *Introduction to statistics and data analysis for physicists.*

[127] D. Budker and D. F. J. Kimball. *Optical magnetometry.* Cambridge University Press, 2013.

[128] N. A. Spaldin. *Magnetic materials: fundamentals and applications.* Cambridge University Press, 2010.

[129] A. Aumann et al. “Polarized patterns in sodium vapor with single mirror feedback”. In: *Phys. Rev. A* 56 (1997), R1709–R1712.

[130] T. Ackemann et al. “Polarization degrees of freedom in optical pattern forming systems: alkali metal vapor in a single-mirror arrangement”. In: *J. Opt. B* 3 (2001), S124–S132.

[131] K. Huang. *Statistical Mechanics.* 2nd ed. 1987.

[132] T. Ackemann et al. “Investigations of pattern forming mechanisms by Fourier filtering: properties of hexagons and the transition to stripes in an anisotropic system”. In: *J. Opt. B* 1.1 (1999), p. 70.

[133] A. J. Scroggie and W. J. Firth. “Pattern formation in an alkali-metal vapor with a feedback mirror”. In: *Phys. Rev. A* 53 (1996), pp. 2752–2764.

[134] M. Le Berre et al. “Simulation and analysis of the flower-like instability in the single-feedback mirror experiment with rubidium vapor”. In: *Opt. Comm.* 118.3 (1995), pp. 447 –456.

[135] T. B. Benjamin and J. E. Feir. “The disintegration of wave trains on deep water Part 1. Theory”. In: *J. Fluid Mech.* 27.03 (1967), pp. 417–430.

[136] K. Tai, A. Hasegawa, and A. Tomita. “Observation of modulational instability in optical fibers”. In: *Phys. Rev. Lett.* 56.2 (1986), p. 135.

[137] G. P. Agrawal. *Nonlinear fiber optics.* Academic press, 2007.

[138] V. E. Zakharov and L. A. Ostrovsky. “Modulation instability: The beginning”. In: *Physica D* 238.5 (2009), pp. 540 –548.

[139] G. Labeyrie and R. Kaiser. “Kibble-Zurek Mechanism in the Self-Organization of a Cold Atomic Cloud”. In: *Phys. Rev. Lett.* 117 (27 2016), p. 275701.

[140] W. J. Firth, A. Fitzgerald, and C. Paré. “Transverse instabilities due to counterpropagation in Kerr media”. In: *J. Opt. Soc. Am. B* 7.6 (1990), pp. 1087–1097.

[141] C. Denz et al. “Pattern dynamics and competition in a photorefractive feedback system”. In: *JOSA B* 15.7 (1998), pp. 2057–2064.